Analysis of Electroneutrality Breakdown in Single-Digit Nanochannels

by

Pragati Shaw

A thesis submitted in partial fulfillment of the requirements for the degree of

Master of Science

Department of Mechanical Engineering
University of Alberta

Abstract

Nanotechnology has advanced in recent years to the extent that custom-tailored structures of high regularity can now be synthesized with high precision. Single-digit nanochannels (SDNs), referring to nanochannels with a diameter or conduit width of less than 10 nanometers, present unique challenges and opportunities for investigation and application. Due to the complex interplay between electrostatic, entropic, and surface-dominated phenomena in such confined regimes, new physical properties emerge. One example is the breakdown of electroneutrality, a situation in which channel surface charges are no longer exactly balanced by the ions in the channel-filling electrolyte. In past theoretical studies of charged, nanofluidic channels, electroneutrality is usually assumed to hold both globally (i.e. for the entire channel) and locally (i.e. for cross sections in the interior of the channel). However, recent work by Levy et al. [1], assuming zero-size ions, indicates that a single channel may not be electroneutral. In this work, we go beyond this initial investigation to examine the breakdown of electroneutrality in a single nanochannel using finite element-based software, COMSOL. Electroneutrality is quantified as the ratio of the ions inside the channel to the fixed charge on the channel surface. The effects of channel dimensions, surface charge density, dielectric constant of the surrounding medium, temperature, and bulk ion concentration on electroneutrality are investigated. The single nanochannel model is also investigated for finite-size ions to evaluate the significance of the steric effects within the nanochannel. Furthermore, the limiting trends depicting the convergence of the electroneutrality breakdown curves for various surface charge densities, dielectric constants, and dimensions of the surrounding medium are studied to understand

the behavior of the system. The investigation is extended to explore this phenomenon in a periodic array of nanochannels. Real-world nanostructures often present such configurations, where the interactions among multiple nanochannels, also referred to as coupling of nanochannels in our work, could influence the overall system behavior. Following this, an infinite periodic array of nanochannels is studied along with the single nanochannel model to identify and examine the differences in the electroneutrality breakdown trends for various parameters.

Additionally, the importance of explicitly incorporating the dielectric medium is highlighted. Levy et al. [1] reported the breakdown of electroneutrality in confined nanopores embedded in a dielectric medium. A Robin boundary condition was derived which eliminates the need to include the dielectric medium explicitly when solving for the electric field within the nanopore. The issues related to the approximations made during the derivation of the boundary condition are pointed out. The errors caused by the use of this boundary condition can be significant even for nanochannels of large aspect (length to radius) ratio, a condition on which the approximations in Levy et al. [1] are based. Our contributions are aimed at critically expanding the understanding of SDNs and the roles of various physical parameters in dictating the behavior of these confined systems.

Preface

The insights and results in Chapter 4 of this thesis, have been recognized, titled "Comment on "Breakdown of electroneutrality in nanopores"", and published in Journal of Colloid and Interface Science, vol. 650, part B, 1285-1289. It is a collaborative effort of my excellent supervisors, Dr. Tian Tang and Dr. Peter Berg, and Dr. Berg's summer student, Ethan Wood. I was responsible for the visualization and validation of the numerical results as well as the manuscript composition. Ethan Wood assisted with the validation of the numerical results as well. Dr. Tang and Dr. Berg were the supervisory authors and were involved with concept formation, and formal analysis and contributed to manuscript edits. Additionally, Peter Berg contributed immensely to the methodology of the project.

Acknowledgements

First of all, I would like to thank my supervisors, Dr. Tian Tang and Dr. Peter Berg, for giving me the opportunity to work under their supervision. Thank you for your unwavering support, sharing your experience, and for teaching me to be critical and confident in my work. These two years have been the most challenging part of my life so far, both personally and professionally. Despite encountering several setbacks, I always came back stronger and it would not have been possible without their continuous emotional support and understanding. I would also like to thank my colleague, Mpumelelo Matse, for the long discussions on COMSOL simulations, his guidance on the fundamentals of research in this field, and his patience towards even my trivial quests.

I would also like to thank my parents, Sheo and Nitu, my sister, Vaishnavi, my brother, Harsh, and all my cousins for believing in me. My family has given me the purpose of my life and is the reason I am here trying to make them proud. A huge thanks to my former high school tutor turned mentor, Spandan Chowdhury, for always being the light at the end of the tunnel. It is for him that I have made most of the good decisions in my life. Thanks to my friends Amit Anand, Lava Kumar Reddy Gunnam, Arshiya Balana, Varun Sai Mulagundla, Gurwinder Singh Sandhu, Mohammed Ayazuddin, and Vireshwar Das for standing next to me through thick and thin. I would like to thank my friend and colleague, Seyedhashem Moosavian for his helpful discussions about mathematics and work life. Last but not least, I would like to thank ChatGPT for its great help with the edits of the thesis. It was a great experience at the university in the last two years.

Table of Contents

List of Tables

List of Figures

List of Symbols

Constants

ϵ_0	Vacuum permittivity	$8.85 \times 10^{-12}\, F/m$
e	Elementary charge	$1.60 \times 10^{-19}\, C$
k_B	Boltzmann constant	$1.38 \times 10^{-23}\, J/K$

Latin

$\mathcal{F}$	Helmholtz free energy
$\tilde{z}$	Valency
a	Diameter of ions and solvent particles
c_0	Bulk ionic concentration
L	Nanochannel length
L_{out}	Reservoir length
R_{in}	Nanochannel radius
R_{out}	Surrounding medium radius in a single channel/Distance between adjacent channels in a periodic array
S	Entropy
T	Temperature
U	Internal energy

Greek

ϵ_{in}	Nanochannel permittivity
ϵ_{out}	Surrounding medium permittivity
κ_D	Inverse Debye length
λ_D	Debye length
ϕ	Electric potential
σ_s	Surface charge density

Abbreviations

BC Boundary condition.

BVP Boundary value problem.

DFT Density functional theory.

DH Debye-Hückel.

DPD Dissipative Particle Dynamics.

DSMC Direct Simulation Monte Carlo.

EDL Electric double layer.

GCS Gouy-Chapman-Stern.

LBM Lattice Boltzmann Method.

MD Molecular Dynamics.

NMR Nuclear magnetic resonance.

NS Navier-Stokes.

OMCTS octamethylcyclotetrasiloxane.

PB Poisson-Boltzmann.

SDN Single-Digit nanochannel.

Chapter 1

Introduction

Nanofluidics, which investigates fluid transport within structures characterized by nanometer dimensions, is a significant research area within the broader field of nanotechnology [2]. A substantial portion of nanofluidic studies are devoted to comprehending and manipulating the transport of ions through nanoscale structures, such as nanochannels or nanopores. The term "nanochannels" denotes channels having at least one dimension of 100 nm or less. The intensive study of ion transport within nanochannels is fueled by the drive to understand the role of biological ion channels in physiological processes [3], and the potential to harness this property for diverse biomedical and chemical applications. The applications of ion transport are indeed extensive and span fields as varied as chemical separation and analysis, molecular filtering, biosensing, and water desalination [4–15]. The advent of advanced nanofabrication techniques has spurred a renewed interest in nanopore-based ionic transport studies in recent years. These advancements allow us to investigate immaculate nanochannels at a single-channel level, including channels formed from materials like carbon nanotubes, boron nitrite nanotubes, or silicon [16–20]. Recent experiments, however, have exposed that our understanding of the fundamental physics of these processes is still incomplete, and significant theoretical gaps persist [21]. This underlines the continuing need for comprehensive studies in nanofluidics and ion transport.

Approaches at different scales have been developed to model ion transport in

nanofluidic systems, each with its own set of advantages and limitations. At the smallest scale, the discrete molecular nature of the system is vital, emphasizing the role of individual molecules and their interactions. Molecular Dynamics (MD) is a prevalent method used to understand these interactions at the atomic scale. For instance, MD has been frequently used to study ion transport in nanochannels due to its detailed portrayal of molecular interactions that drive the transport process [22–26]. Direct Simulation Monte Carlo (DSMC) methods, on the other hand, are preferred for studying ion transport when dealing with significant randomness or uncertainty [27–31]. To achieve high accuracy, hybrid methods combining these approaches are also considered [32–34]. Transitioning to the mesoscale, we encounter methods that bridge the gap between molecular and continuum scales. Here, the focus is less on individual atoms or molecules and more on collective behavior, patterns, and emergent phenomena. The Lattice Boltzmann Method (LBM) is a widely recognized technique adept at addressing problems where both mesoscopic dynamics and microscopic statistics play pivotal roles. By transforming the Navier-Stokes (NS) equations into a discrete set of lattice models, LBM provides a more efficient and scalable approach to simulations [35–41]. The Dissipative Particle Dynamics (DPD) method is another approach that integrates aspects from MD and LBM. It offers a distinctive perspective on simulating fluid dynamics at mesoscale levels, providing efficient and accurate simulations for complex fluid systems [42–47]. Finally, at the macroscopic level, continuum theories form the foundation of our understanding of fluid dynamics. These models ignore the molecular complexities of gases and liquids, treating the fluid as a continuous medium characterized by spatial and temporal changes in macroscopic properties such as density, pressure, temperature, velocity, and other flow parameters. The most well-known and widely utilized continuum model is governed by the NS equations, which describe the motion of fluid substances. These equations use principles of conservation of mass and momentum to define the behavior of fluids. However, at smaller scales, modifications to the NS equations are often required to account for effects like slip at the

boundaries [48]. Chan and Horn [49] confirmed, using a Surface Force Apparatus, that hydrodynamic predictions, explicitly using the Reynolds formula, remain valid for confinements exceeding roughly ten molecular diameters. This observation was later corroborated by Georges et al. [50]. In more recent studies, specifically focusing on water, Klein et al. [51] and E. Riedo et al. [52] demonstrated that water retains its bulk viscosity up to a scale of approximately $1 - 2\,\mathrm{nm}$. However, when the confinement becomes more pronounced, there is a marked shift in behavior, with the wettability of the confining surface becoming a significant factor [53]. Observations of analogous behavior have also been noted for other liquids, such as octamethylcyclotetrasiloxane (OMCTS) [53, 54]. Hence, the continuum theory of hydrodynamics remains applicable to simple fluids when confinement exceeds approximately $1\,\mathrm{nm}$, as stated by Bocquet and Barrat [55]. Up to this point, all the models discussed have been non-equilibrium models. The most well-known continuum model for electrolytes under equilibrium is governed by the Poisson-Boltzmann (PB) equation and is commonly used to describe the distribution of ions in a fluid under an electric field. The equation combines the Poisson equation, which relates the electric potential to the charge density, and the Boltzmann distribution, which describes the probability of a particle being in a particular state with a given energy at a certain temperature. Many works have been performed on the applicability of the PB equation for nanoscale electroosmotic flows [24, 56–63], highlighting the discrepancy in the results as compared to the atomistic simulations. However, Wang et al. [64] found that the PB model is reliable for predicting electroosmotic flows through nanochannels up to high ionic concentrations ($\sim 1\,\mathrm{M}$) and produces accurate electric potential profiles even with strong electric double layer (EDL) interaction. Another approach to improve the accuracy of the PB equation was to modify it to account for the effects not considered in its classical version. Depending on the nanochannel system, these modifications include accounting for finite ion size [65], non-electrostatic interactions [66], solution permittivity changes with field strength [67], wall-related effects [68], and

unique solvent effects [65]. With these changes, which are largely based on statistical mechanics, the equation can better predict ion distribution in nanochannels.

Single-digit nanochannels (SDNs), referring to nanochannels with a diameter or conduit width of less than 10 nanometers, represent an intriguing subfield within the wider landscape of nanofluidics. With their extremely small dimensions, SDNs present unique challenges and opportunities for investigation and application. Conventionally, continuum theories have been widely used to study ion transport in SDNs. These theories, by making assumptions about the properties of the fluid on a macroscopic level, allow for a simplified mathematical treatment of the transport phenomena. However, when the confinement reaches the nanoscale as in SDNs, the behavior of fluids and ions can significantly deviate from bulk behavior. The effects of the confining surface, quantum confinement, and finite-size ions become substantial. These changes can lead to discrepancies in the predictions of the continuum model, emphasizing the need for a new theoretical framework that encompasses both discrete and continuum behaviors. Several pioneering studies have ventured into this complex domain, such as the study focused on the assumption of electroneutrality within the SDNs. Electroneutrality is a foundational assumption considered in the boundary conditions in many continuum models, particularly the PB equation [69–81]. It assumes that the net electric charge within a given volume is zero. Because of this assumption, theoretical studies nearly always take the total charge neutrality (or electroneutrality) inside nanoconfined regions for granted, and experimental evaluation of electroneutrality inside nanoconfined regions was lacking [82–85].

The study by Luo et al. [86] explored the breakdown of electroneutrality in nanoconfined aqueous electrolytes in a slit-shaped pore. They utilized quantitative nuclear magnetic resonance (NMR) measurements and numerical calculations based on the classical PB equation. The findings revealed a significant breakdown of electroneutrality inside uncharged nanoconfined regions along with very asymmetric responses of cations and anions to the charging of nanoconfined surfaces. Following this, sev-

eral studies focusing on ion transport within SDNs in relation to the breakdown of electroneutrality were conducted. One notable study by Noh and Aluru [87] employed molecular dynamics simulations to develop an ion conductance theory that accurately predicts the experimental data for electrically "imperfect" nanopores with a constant surface charge. They termed nanopores as "imperfect" when the total charge of the solution within the pore was insufficient to uphold electroneutrality. Their ion conductance theory took into account this "imperfectness". Furthering this investigation, Ji et al. [88] delved into the dynamics of monovalent ions within SDNs from the perspective of ion conductance. Their experimental findings using silicon nitride SDNs substantiated that the breakdown of electroneutrality contributed to the enhancement of ion conductance within the pore. Another study by Colla et al. [84] examined a scenario involving two charged plates submerged in water. They addressed the presence of free ions on both sides of each plate and employed density functional theory (DFT) for the entire spatial domain. Due to asymmetric screening, particularly noticeable with a substantial screening length, the accumulation of charge between the plates can be minimal. This phenomenon is referred to by the authors as an instance of the local breakdown of electroneutrality.

Building on the concept of electroneutrality breakdown, Levy et al. [1] utilized the continuum model approach, specifically employing the PB equation, to analyze cylindrical nanochannels. They investigated confined ions in electrolytes within charged cylindrical channels, accounting for the presence of an electric field extending into the surrounding medium, thereby showing the breakdown of electroneutrality for zero-size ions. De Souza et al. [89] extended the analysis of electroneutrality breakdown to an infinite periodic nanochannel array using continuum simulations and discussed the effects of various physical factors. Using several assumptions and asymptotic relations, the authors presented analytical equations to quantify the breakdown within an array in the linear regime of PB equation.

Through this discussion, we highlight that while continuum theories inherently

possess some limitations in capturing every subtlety of SDN behavior, they serve well as a foundational theoretical framework. Using this framework to study phenomena, such as the breakdown of electroneutrality paves the way for more specialized models. As such, they act as a critical stepping stone, which can be refined and adapted more precisely to understand various aspects of SDNs. Thus, the model by Levy et al. [1] serves as a cornerstone for our work on SDNs. We undertake a detailed analysis of electroneutrality within single nanochannels, considering a broad spectrum of physical parameters. This includes observing the patterns of electroneutrality breakdown and investigating their underlying causes. Additionally, we consider the role of temperature, comparing trends in two distinct thermal settings. Moreover, we examine the impact of steric effects on the breakdown process, which justifies the use of the classical PB equation. Transitioning from single nanochannels, our investigation on electroneutrality breakdown broadens to encompass an infinite array of nanochannels. Emphasizing the applicability of the single nanochannel model, we illustrate its use to represent an infinite array, especially when the distance between channels significantly exceeds the channel radius. This approach streamlines numerical simulations, offering notable savings in computational resources and time. In addition to this, we examine the assumptions made in deriving a Robin boundary condition put forth by Levy et al. [1]. We emphasize the potential issues linked to using this boundary condition, particularly in understanding electroneutrality breakdown. Through this discussion, we highlight the importance of explicitly considering the dielectric medium in the model.

This thesis is structured as follows:

1. In **Chapter 2**, we offer a concise review of the continuum modelling of electrostatics within electrolytes, laying down the fundamental theories and concepts that govern our study.

2. In **Chapter 3**, we delve into an in-depth analysis of electroneutrality within

single nanochannels across a spectrum of physical parameters. This includes a comprehensive investigation into the trends of electroneutrality breakdown and a meticulous exploration of the underlying causes for these breakdowns. The influence of temperature is taken into account as we explore the trends in two different temperature settings. This chapter also engages with the contribution of steric effects to the breakdown process, which justifies the use of the classical Poisson-Boltzmann equation in our study.

3. In **Chapter 4**, we identify and discuss the problematic assumptions made in the derivation of a Robin boundary condition introduced by Levy et al. [1]. We highlight the significant implications that the use of this boundary condition can have on the understanding of electroneutrality breakdown, emphasizing the importance of explicitly including the dielectric medium in the model.

4. In **Chapter 5**, we expand our study from single nanochannels to an infinite periodic array of nanochannels. Drawing upon our insights from earlier chapters, we explore the electroneutrality breakdown in this new context, again in two different temperature conditions. We align our findings with the work of De Souza et al. [89], further strengthening and validating our conclusions. We highlight the applicability of the single nanochannel model as a representation of the infinite array when the inter-channel distance significantly exceeds the channel radius.

5. Finally, in **Chapter 6**, a summary of our findings and the contribution to the understanding of electroneutrality breakdown in nanochannels are discussed. Additionally, we propose potential avenues for future exploration, aiming to stimulate further research and advancements in this critical area of nanofluidics.

Chapter 2

Continuum modelling of electrostatics in electrolytes

The literature review in the preceding chapter underscores the significance of studying electrostatics within nanochannels, which ultimately aids in comprehending ion transport mechanisms. In the current chapter, we will undertake a concise review of fundamental concepts pivotal to modeling the electrostatics in electrolytes using continuum theory.

2.1 Charged solid-liquid interface

When a solid comes into contact with a liquid, it often carries a surface charge. The surface charge is typically a result of surface group dissociation or the adsorption of ions from the solution onto the surface, which does not necessarily involve electron transfer [90, 91]. The nature of the surface charge on a solid, whether it is positive or negative, depends on the quantity and type of acidic and basic groups present in the solution [92–94]. In reality, charged interfaces are a result of the presence of functional groups on the solid-liquid interface. For example, the surface of silica hydrolyzes when silica interfaces with an aqueous solution, giving rise to silanol surface groups. Depending on the pH value of the electrolyte solution, these groups can be positively charged ($Si{-}OH_2^+$), neutral ($Si{-}OH$), or negatively charged ($Si{-}O^-$). Another example is metal-liquid interfaces that can be charged upon application of a

bias potential to a metal electrode. Here, the nature of electron band structure of the metal gives rise to much smoother (less discrete) surface charge distribution. In the context of nanochannels, due to their high surface-to-volume ratio, the surface charge density on the solid-liquid interface can be discrete in nature although in mean-field approaches, the surface charge density is homogenized.

Surface charges give rise to electrostatic forces, playing a critical role in the long-range interactions between molecules and surfaces within liquid environments. Hence, they are instrumental in controlling the transport processes in nanofluidic systems [1, 95].

2.2 Electric double layer and Debye length

In the mean-field approach, owing to the presence of a surface charge on the solid surface, an oppositely charged region of counterions emerges in the liquid in the vicinity of the surface. A number of theoretical models have been formulated to elucidate the structure of this region. The Gouy-Chapman-Stern (GCS) model [96], in particular, is widely used in interfacial science. This model defines the so-called EDL, which consists of two distinct regions, namely, (i) the 'Stern layer' which corresponds to the compact layer of counterions that have a strong interaction with the surface [97], and (ii) the 'diffuse layer' which is made up of a mixture of co-ions and counter-ions. These ions are not as restrained and more mobile than the ions in the Stern layer. Electrokinetic phenomena arise due to the presence of the EDL. These phenomena, such as electroosmosis, electrophoresis, and streaming potential, refer to various behaviors and motion of liquids that arise due to the presence of an electric field [95].

In simple continuum theories, such as the Gouy-Chapman model, the EDL effectively screens the surface charge, causing the electric field to drop off exponentially with the distance from the surface. This is referred to as the shielding effect. However, when the size of the EDL becomes comparable to the size of the nanochannel, these simple models can overestimate this shielding effect. The size of the EDL can

be characterized by the Debye length (λ_D), defined as

$$\lambda_D = \sqrt{\frac{\epsilon k_B T}{2e^2 \sum_i \tilde{z}_i^2 c_{0i}}}, \tag{2.1}$$

where c_{0i} is the bulk concentration of the i^{th} type of ions (in m^{-3}) and ϵ is the permittivity of the fluid. It can be expressed as $\epsilon = \epsilon_0 \epsilon_r$ where $\epsilon_0 = 8.854 \times 10^{-12}$ F/m is the vacuum permittivity and ϵ_r is the relative permittivity of the fluid. $k_B = 1.38 \times 10^{-23}$ J/K is the Boltzmann constant and T is the temperature.

2.3 Continuum modelling of electrolyte

The continuum modeling approach used in this study is grounded in the Gouy-Chapman framework. Within this perspective, the interactions between charged species (counterions and co-ions) and solvents (such as water) hinge on the classical theory that addresses the interaction of mobile point charges within continuum media.

From the thermodynamics point of view, it is helpful to consider the Helmholtz free energy in order to understand how systems evolve and reach equilibrium under constant volume and temperature. It encapsulates both energetic and entropic effects, providing a key criterion for spontaneous processes. The idea is that closed (no mass exchange with the environment) thermodynamic systems at constant volume and temperature naturally evolve in a way that minimizes the Helmholtz free energy. The Helmholtz free energy ($\mathcal{F}$) of a system is given by $\mathcal{F} = U - TS$, where U is the internal energy and S is the entropy. In a state of electroneutrality, the system minimizes its internal energy. However, as the temperature increases, the system gains more thermal energy, and the entropy or the measure of randomness or disorder of the system also increases. The system will start to favor configurations that maximize entropy, even if they increase the internal energy. The temperature effectively determines the trade-off between minimizing internal energy and maximizing entropy. At zero or very low temperatures, the system tends toward electroneutrality,

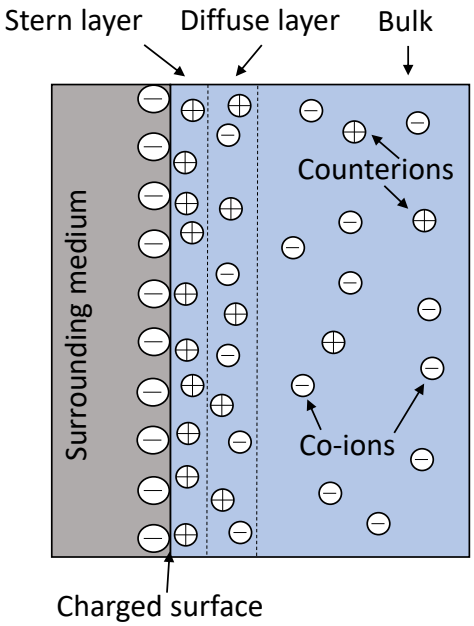

Figure 2.1: Schematic diagram of a negatively charged nanochannel containing an electrolyte as described by a Gouy-Chapman model.

while at higher temperatures the ions are allowed to arrange themselves in ways that are not strictly electroneutral, but increase the entropy of the system. This balance between minimizing energy (toward electroneutrality) and maximizing entropy (away from strict electroneutrality) leads to a state of dynamic equilibrium in the system as the temperature is varied.

2.3.1 Classical Poisson-Boltzmann equation

We begin with the assumption that the ionic species within the electrolyte domain are mobile point charges. This domain includes the volumetric interior of the channel, as shown in Fig. 2.1. In local density approximations, the free energy of each ionic species at each location in the volumetric domain depends solely on local variables such as the electric potential ϕ (expressed in units of Volts [V]) and the ionic charge density ρ^{ion}

$$\rho^{ion} = \sum_i e\tilde{z}_i c_i, \tag{2.2}$$

where c_i (expressed in m^{-3}) represents an averaged local concentration of ions for the i^{th} species, measured as the number of ions per unit volume. $\tilde{z}_i$ is the valency of the i^{th} ion and e is the elementary charge with the value of 1.602×10^{-19} C.

The Helmholtz free energy in a domain Ω is determined by [98],

$$\mathcal{F} = U - TS, \tag{2.3}$$

$$U = \int \left[-\frac{\epsilon}{2} |\nabla \phi|^2 + \rho^{ion} \phi - \sum_i \bar{\mu}_i c_i \right] d\Omega, \tag{2.4}$$

$$-TS = \int k_B T \left[\sum_i c_i \log \frac{c_i}{c_{ri}} - \sum_i c_i \right] d\Omega. \tag{2.5}$$

The first term in Eq. 2.4 is the electric field energy, which arises due to the spatial variation of the electric potential ϕ. The second term in Eq. 2.4 corresponds to the electrostatic energy of the ions while the third term represents the chemical potential energy. The electrochemical potential $\bar{\mu}_i$ is defined as a measure of the energy change of a system when an additional particle is added, keeping volume and entropy constant. Note that the electrochemical potential includes the reference chemical potential at the standard state. In Eq. 2.5, derived from Boltzmann's foundational entropy formula [99], c_{ri} denotes a reference ionic concentration. c_{ri} can be, for instance, the electrolyte's bulk ionic concentration, thereby coupling the system to a bulk reservoir. The expression $k_B T \sum_i c_i \log \frac{c_i}{c_{ri}}$ represents the entropy of mixing, capturing the change in the entropy of the system when ions deviate from their reference concentrations, whereas $-k_B T \sum_i c_i$ is the so-called osmotic term [100].

The system will naturally evolve to a state where $\mathcal{F}$ is minimized, determined by minimizing the functional (with variables ϕ and c) Eq. 2.3, using the variational principle [101]. By taking the variation of $\mathcal{F}$ with respect to ϕ and setting it to zero,

we can determine the free-energy minimum

$$\begin{aligned}
\delta\mathcal{F}|_{\phi} &= \int \left[-\frac{\epsilon}{2}\,\delta\left(|\nabla\phi|^2\right) + \rho^{ion}\delta\phi\right] d\Omega \\
&= \int \left[-\frac{\epsilon}{2}\,\delta\left(\nabla\phi\cdot\nabla\phi\right) + \rho^{ion}\delta\phi\right] d\Omega \\
&= \int \left[-\epsilon\,\delta\left(\nabla\phi\right)\cdot\nabla\phi + \rho^{ion}\delta\phi\right] d\Omega \\
&= \int \left[-\epsilon\,\nabla\left(\delta\phi\right)\cdot\nabla\phi + \rho^{ion}\delta\phi\right] d\Omega \\
&= \int \left[-\epsilon\left\{\nabla\cdot\left(\nabla\phi\delta\phi\right) - \nabla^2\phi\delta\phi\right\} + \rho^{ion}\delta\phi\right] d\Omega \\
&= -\int \epsilon\,\nabla\cdot\left(\nabla\phi\,\delta\phi\right) d\Omega + \int \left(\epsilon\nabla^2\phi + \rho^{ion}\right)\delta\phi\, d\Omega \\
&= -\int \epsilon\left(\nabla\phi\cdot\mathbf{n}\right)\delta\phi\, dA + \int \left(\epsilon\nabla^2\phi + \rho^{ion}\right)\delta\phi\, d\Omega = 0, \qquad (2.6)
\end{aligned}$$

where A represents the boundary surface enclosing the volume Ω. The integrand involving A is derived through the application of the Divergence theorem, which relates the flux of $\nabla\phi$ across A and the divergence of $\nabla\phi$ within the encompassed volume Ω. In sufficiently large domains, the surface integral is usually assumed to vanish. According to Gauss' law, this implies a balanced net charge within the enclosed surface [102]. Rearranging the integrand of the second integral of Eq. 2.6 results in the Poisson equation

$$\nabla^2\phi = -\frac{\rho^{ion}}{\epsilon}. \qquad (2.7)$$

This establishes a relationship between a static electric field and the electric charges that induce it.

Varying the free energy $\mathcal{F}$ with respect to the ionic concentration c_i gives the electrochemical potential, which is a measure of the change in free energy as the amount of that species (with ionic concentration c_i) changes. At equilibrium, the free energy of the system is at its minimum, which implies that any small addition or removal of any species does not change the free energy. Using Eq. 2.5, the variation of $\mathcal{F}$ with respect to c_i yields

$$\delta\mathcal{F}|_{c_i} = 0 \implies -\bar{\mu}_i + \tilde{z}_i e\phi + k_B T\log\frac{c_i}{c_{ri}} = 0. \qquad (2.8)$$

Rearranging Eq. 2.8, we get

$$\bar{\mu}_i = \tilde{z}_i e\phi + k_B T \log \frac{c_i}{c_{ri}}. \tag{2.9}$$

At equilibrium, the electrochemical potential anywhere in the electrolyte is equal to the bulk chemical potential,

$$\bar{\mu}_i = \mu_{0i}. \tag{2.10}$$

In the bulk, the electric potential ϕ is zero thereby reducing the electrochemical potential to the chemical potential, given as [99]

$$\mu_{0i} = k_B T \log \frac{c_{0i}}{c_{ri}}, \tag{2.11}$$

where the subscript 0 denotes the bulk. Equation 2.9, Eq. 2.10, and Eq. 2.11 are solved for c_i, leading to the Boltzmann equation. This provides us with the local concentration of each type of ion in the diffuse layer,

$$c_i = c_{0i} \exp\left[-\frac{\tilde{z}_i e\phi}{k_B T}\right]. \tag{2.12}$$

By substituting Eq. 2.2 and Eq. 2.12 into Eq. 2.7, we derive the complete PB equation for zero-size particles. This equation describes how the electrostatic potential varies with position at equilibrium due to the distribution of ions within the electrolyte domain,

$$\nabla^2 \phi = -\frac{e}{\epsilon} \sum_i \tilde{z}_i c_{0i} \exp\left[-\frac{\tilde{z}_i e\phi}{k_B T}\right]. \tag{2.13}$$

In the case of a binary symmetric $\tilde{z} : \tilde{z}$ electrolyte, where all positive ions have a valency of $\tilde{z}$ and all negative ions have a valency of $-\tilde{z}$ (with $\tilde{z} > 0$), and where $c_{0i} = c_0$ for $i = 1, 2$, the equation becomes

$$\nabla^2 \phi = \frac{2\tilde{z} e c_0}{\epsilon} \sinh\left[\frac{\tilde{z} e\phi}{k_B T}\right]. \tag{2.14}$$

2.3.2 Modified Poisson-Boltzmann equation

One of the major limitations of the classical PB equation is the assumption of point-like or zero-size ions. This model works well for dilute electrolytes, given that it

is based on mean-field theory, but it breaks down for high concentrations of ions. However, it is important to note that the assumption of a continuum of charges breaks down when the nanochannel becomes highly charged, exhibiting large ion concentrations, as more complex effects can come into play. These can include ion-ion correlations, where the ions in an electrolytic solution interact with each other, and steric effects, where the ions are no longer assumed to be point-like charges. The latter is critical because ions cannot pack as densely as classical continuum models would predict [103, 104], which can affect the distribution of ions and hence the properties of the system. Steric effects are included in some more advanced models, such as the modified PB equation [105, 106].

Borukhov and Andelman [107] tackled this problem by considering finite-size ions instead of zero-size ions as used in the classical PB equation. Keeping the contribution of internal energy the same as in Eq. 2.4, the entropic contribution is modified as

$$-TS = \int k_B T \left[\sum_i c_i \log\left(c_i a^3\right) - \sum_i c_i + w \log\left(w a^3\right) - w \right] d\Omega, \tag{2.15}$$

where w is the concentration of the solvent (such as water) expressed in m^{-3}. The electrolytic ions and the solvent molecules are assumed to be cubes of equal sizes. The volume of these ion and water particles is approximated as a^3 where a is an edge of the cube. Equation 2.15 takes into account the additional terms with w that are absent in Eq. 2.5, representing the entropic contribution of the water molecules.

Assuming that, aside from the ions, the remaining space is occupied by solvent molecules, we can then proceed as follows

$$w = \frac{N_w}{V} = \frac{N_w a^3}{V a^3} = \frac{V - \sum_i N_i a^3}{V a^3} = \frac{1}{a^3}(1 - \sum_i c_i a^3), \tag{2.16}$$

where V is the whole volume of the electrolyte. N_w and N_i are the numbers of solvent molecules and ions, respectively. Equation 2.16 can be written as

$$w a^3 + a^3 \sum_i c_i = 1, \tag{2.17}$$

which simply means the sum of volume fractions of solvent and ions is one. Substituting Eq. 2.17 into Eq. 2.15

$$-TS = \int k_B T \left[\sum_i c_i \log\left(c_i a^3\right) - \sum_i c_i + \frac{1}{a^3}\left(1 - \sum_i c_i a^3\right) \log\left(1 - c_i a^3\right) - \frac{1}{a^3}\left(1 - \sum_i c_i a^3\right)\right] d\Omega. \tag{2.18}$$

At equilibrium, the system minimizes its free energy. Hence, varying the modified $\mathcal{F}$ with respect to ϕ and setting it equal to zero results again in the Poisson equation as shown in Eq. 2.7. Similarly, in the equilibrium state, adding or removing species does not alter the free energy. By varying the modified $\mathcal{F}$ with respect to c_i and setting it equal to zero, we obtain

$$\delta\mathcal{F}|_{c_i} = -\bar{\mu}_i + \tilde{z}_i e\phi + k_B T \left[\log\left(\sum_i c_i a^3\right) - \log\left(1 - \sum_i c_i a^3\right)\right] = 0, \tag{2.19}$$

from which the electrochemical potential $\bar{\mu}_i$ is obtained,

$$\bar{\mu}_i = \tilde{z}_i e\phi + k_B T \left[\log\left(\sum_i c_i a^3\right) - \log\left(1 - \sum_i c_i a^3\right)\right]. \tag{2.20}$$

At equilibrium, the electrochemical potential $\bar{\mu}_i$ equals the bulk chemical potential μ_{0i} as the electric potential ϕ is zero in the bulk

$$\mu_{0i} = k_B T \left[\log\left(c_{0i} a^3\right) - \log\left(1 - c_{0i} a^3\right)\right], \tag{2.21}$$

where the subscript 0 denotes the bulk situation. This provides us with c_i as

$$c_i = \frac{c_{0i} \exp\left[\frac{\tilde{z}_i e\phi}{k_B T}\right]}{1 - c_{0i} a^3 + c_{0i} a^3 \exp\left[\frac{\tilde{z}_i e\phi}{k_B T}\right]}. \tag{2.22}$$

By substituting Eqs. 2.2 and 2.22 into Eq. 2.7, we arrive at the modified PB equation

$$\nabla^2\phi = -\frac{e}{\epsilon} \sum_i \frac{c_{0i} \exp\left[\frac{\tilde{z}_i e\phi}{k_B T}\right]}{1 - c_{0i} a^3 + c_{0i} a^3 \exp\left[\frac{\tilde{z}_i e\phi}{k_B T}\right]}. \tag{2.23}$$

For a binary symmetric $\tilde{z} : \tilde{z}$ electrolyte where $c_{0i} = c_0$ for $i = 1, 2$, we find

$$\nabla^2\phi = \frac{2\tilde{z} e c_0}{\epsilon} \frac{\sinh\left[\frac{\tilde{z}_i e\phi}{k_B T}\right]}{1 - c_{0i} a^3 + c_{0i} a^3 \cosh\left[\frac{\tilde{z}_i e\phi}{k_B T}\right]}. \tag{2.24}$$

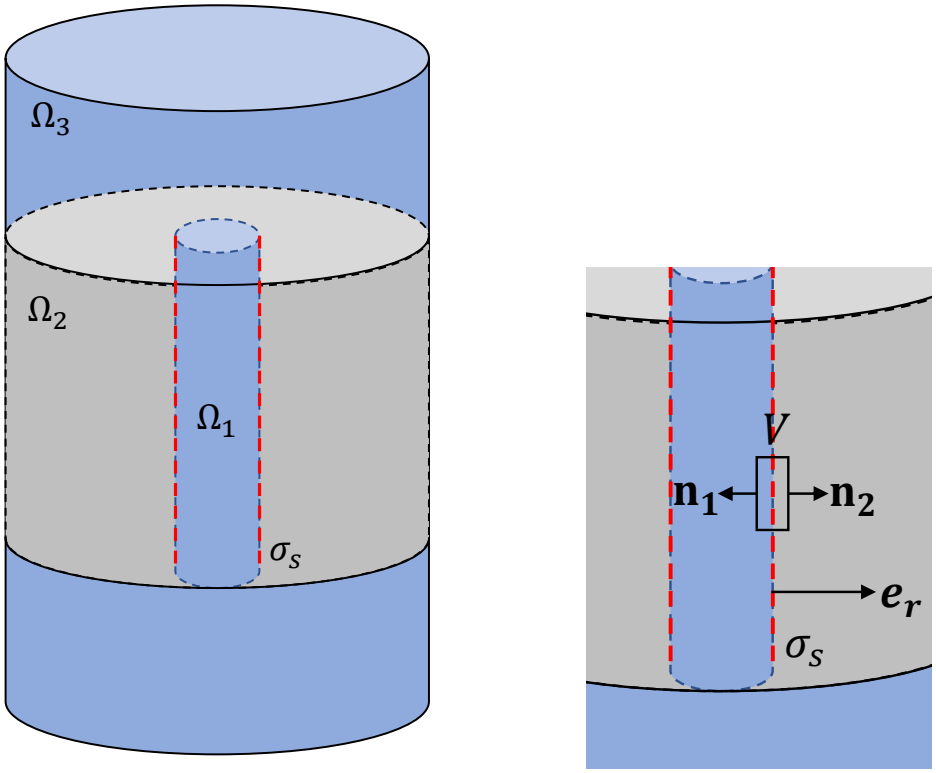

(a) (b)

Figure 2.2: (a) A schematic diagram of the model featuring a nanochannel (Ω_1) with surface charge density σ_s, embedded within a dielectric medium (Ω_2), and connected to a reservoir (Ω_3) at both entrances. (b) A small volume V with negligible thickness encompassing the channel wall with $\mathbf{n}$ as the outward surface vector. $\mathbf{e_r}$ is the unit vector normal to the channel wall pointing towards the dielectric medium.

2.4 System to model nanochannel

Figure 2.2a shows the system used to model a single nanochannel in this work, which is divided into three distinct domains, namely Ω_1, Ω_2, and Ω_3. Here, Ω_1 represents the nanochannel itself with surface charge density σ_s, embedded within a dielectric medium denoted by Ω_2. The entrances of the nanochannel are connected to the reservoir, Ω_3, which ensures the maintenance of chemical equilibrium within the nanochannel. We model the electric field distribution within the nanochannel and the reservoirs using the PB equation. For the distribution of the electric field within the dielectric medium, the Laplace equation is utilized, as presented in Eq. 2.25. This

is a direct result of the Poisson equation (Eq. 2.7) as the charge density is zero within the dielectric medium ($\rho^{ion} = 0$),

$$\nabla^2 \phi = 0. \tag{2.25}$$

The boundary condition at the nanochannel-dielectric interface ensures the continuity of electric potential and is derived from the Poisson equation (Eq. 2.7). Specifically, consider a small volume V with negligible thickness at the channel wall (depicted in Fig. 2.2b), with $\mathbf{n}$ being the unit outward surface vector. Integrating the Poisson equation within this volume yields the total charge,

$$\int_V \epsilon \nabla \cdot \nabla \phi \, dV = -\int_V \rho \, dV. \tag{2.26}$$

Using the Divergence theorem, we get

$$\int \epsilon \nabla \phi \cdot \mathbf{n} \, dA = -\sigma_s A. \tag{2.27}$$

where A represents the boundary surface enclosing the volume V. As the thickness of volume V tends to zero, the surfaces of the volume collapse on the channel wall resulting in area A,

$$\epsilon_{in} \nabla \phi_{in} \cdot \mathbf{n_1} \, A + \epsilon_{out} \nabla \phi_{out} \cdot \mathbf{n_2} \, A = -\sigma_s A, \tag{2.28}$$

where ϕ_{in} and ϕ_{out} are the electric potential within the nanochannel and the dielectric medium, respectively. ϵ_{in} is the permittivity of the fluid within the nanochannel while ϵ_{out} is the permittivity of the dielectric medium. Considering $\mathbf{e_r}$ as the unit vector in the radial direction pointing outward from the channel wall towards the dielectric medium as shown in Fig. 2.2b,

$$\epsilon_{in} \frac{\partial \phi_{in}}{\partial r} \mathbf{e_r} \cdot (-\mathbf{e_r}) + \epsilon_{out} \frac{\partial \phi_{out}}{\partial r} \mathbf{e_r} \cdot (\mathbf{e_r}) = -\sigma_s, \tag{2.29}$$

$$\implies \epsilon_{out} \frac{\partial \phi_{out}}{\partial r} - \epsilon_{in} \frac{\partial \phi_{in}}{\partial r} = -\sigma_s. \tag{2.30}$$

Equation 2.30 is the boundary condition on the channel wall accounting for the surface charge σ_s. This signifies the discontinuity of the electric displacement on the channel

wall. Conversely, the electric displacement on the dielectric-reservoir interface is continuous due to the assumption of an absence of surface charge.

In this chapter, we provided a brief review of the principles of electrostatics within electrolytes and the framework of continuum modeling. Moreover, we delved into the theoretical foundation of the system employed to model the nanochannel in this study. The system and its modified versions are simulated using COMSOL Multiphysics and the results are presented in the subsequent chapters.

Chapter 3

Electroneutrality breakdown in a single nanochannel

In this chapter, we shall employ the continuum modeling of electrolytes to study electroneutrality breakdown within a single nanochannel. Previous research by Levy et al. [1] explored the confinement of ions in electrolytes inside charged cylindrical channels. They acknowledged the breakdown of electroneutrality for zero-size ions. Building upon these findings, our study delves deeper into the impact of different physical parameters on electroneutrality breakdown within a single nanochannel. These results are graphically represented via phase diagrams, based on two defining variables (or parameters). The electric field in the medium surrounding the channel is thoroughly quantified, shedding light on the reasons behind the extent of breakdown observed. Additionally, the trends of this breakdown are evaluated at an elevated temperature. The choice of employing zero-size ions in our study is further validated by introducing finite-size ions into the investigation.

3.1 Infinitely long, single nanochannel

We begin by establishing the validity of numerical simulations through their comparison with the analytical solution of a one-dimensional model. The one-dimensional axisymmetric system is depicted in Fig. 3.1a. The system comprises an infinitely long nanochannel characterized by a radius R_{in}, a surface charge density σ_s, and a permit-

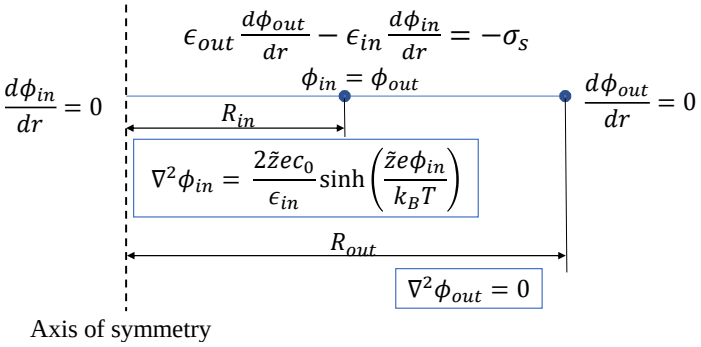

(a)

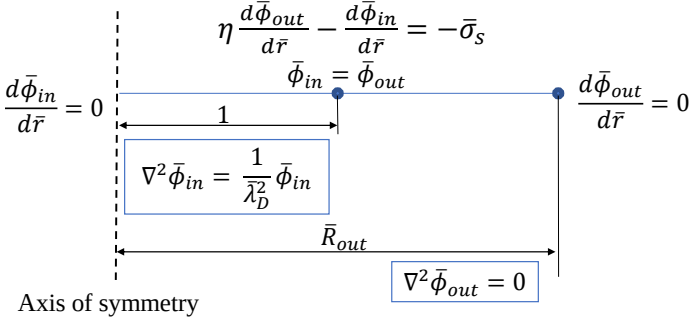

(b)

Figure 3.1: Sketch of a one-dimensional nanochannel with (a) the dimensional governing equations and boundary conditions, and (b) the normalized governing equations and boundary conditions in the Debye-Hückel regime.

tivity ϵ_{in}. ϵ_{in} is given by $\epsilon_{in} = \epsilon_0\epsilon_{in}^r$, where ϵ_{in}^r corresponds to the relative permittivity within the nanochannel. The nanochannel is embedded within a dielectric medium with a radius R_{out} and a permittivity ϵ_{out}. The fluid confined within the nanochannel consists of ions with negligible size.

The electric field distribution within the nanochannel, with a binary symmetric $\tilde{z} : \tilde{z}$ electrolyte, is governed by the classical PB equation (see Sec. 2.3.1),

$$\frac{1}{r}\frac{d}{dr}\left(r\frac{d\phi_{in}}{dr}\right) = \frac{2\tilde{z}ec_0}{\epsilon_{in}}\sinh\left(\frac{\tilde{z}e\phi_{in}}{k_BT}\right), \tag{3.1}$$

where ϕ_{in} is the electric potential within the nanochannel. In contrast, the Laplace

equation is utilized to describe the electric field in the surrounding dielectric medium,

$$\frac{1}{r}\frac{d}{dr}\left(r\frac{d\phi_{out}}{dr}\right) = 0, \tag{3.2}$$

where ϕ_{out} is the electric potential within the dielectric medium. The system of equations involving Eq. 3.1 and Eq. 3.2 is solved with the corresponding boundary conditions (BCs)

$$\left.\frac{d\phi_{in}}{dr}\right|_{r=0} = 0, \tag{3.3}$$

$$\epsilon_{out}\left.\frac{d\phi_{out}}{dr}\right|_{r=R_{in}} - \epsilon_{in}\left.\frac{d\phi_{in}}{dr}\right|_{r=R_{in}} = -\sigma_s, \tag{3.4}$$

$$\phi_{in}|_{r=R_{in}} = \phi_{out}|_{r=R_{in}}, \tag{3.5}$$

$$\left.\frac{d\phi_{out}}{dr}\right|_{r=R_{out}} = 0. \tag{3.6}$$

Equation 3.3 is a consequence of the Poisson equation (Eq. 2.7) in the vicinity of $r = 0$. The uniform charge density on the surface of the nanochannel is established by Eq. 3.4. Equation 3.5 ensures continuity of the electric potential across the boundary of the two domains. The electric field is assumed to vanish at the outer surface of the dielectric medium as expressed by the BC in Eq. 3.6. This is mainly because the dielectric medium is much wider than the radius of the channel. In essence, electroneutrality is imposed globally in the system.

Normalization helps us achieve a dimensionless representation that simplifies mathematical analysis and numerical computations. Furthermore, it allows for a clearer understanding and interpretation of results, as the normalized variables provide insights into the relative magnitudes and influences of different quantities involved. Moreover, normalization establishes a consistent framework for comparing different systems, facilitating meaningful comparisons and generalizations. In particular, we

introduce

$$\bar{\phi} = \frac{\tilde{z}e\phi}{k_B T}, \tag{3.7}$$

$$\bar{r} = \frac{r}{R_{in}}, \tag{3.8}$$

$$\bar{R}_{out} = \frac{R_{out}}{R_{in}}, \tag{3.9}$$

$$\eta = \frac{\epsilon_{out}}{\epsilon_{in}}, \tag{3.10}$$

$$\bar{\sigma}_s = \frac{\tilde{z}e\sigma_s R_{in}}{\epsilon_{in} k_B T}, \tag{3.11}$$

$$\bar{\lambda}_D = \frac{\lambda_D}{R_{in}}, \tag{3.12}$$

where $\lambda_D = \sqrt{\frac{\epsilon_{in} k_B T}{2\tilde{z}^2 e^2 c_0}}$ is the Debye length. With these definitions Eqs. 3.1 and 3.2 become

$$\frac{1}{\bar{r}} \frac{d}{d\bar{r}} \left(\bar{r} \frac{d\bar{\phi}_{in}}{d\bar{r}} \right) = \frac{1}{\bar{\lambda}_D^2} \sinh(\bar{\phi}_{in}), \tag{3.13}$$

$$\frac{1}{\bar{r}} \frac{d}{d\bar{r}} \left(\bar{r} \frac{d\bar{\phi}_{out}}{d\bar{r}} \right) = 0. \tag{3.14}$$

The BCs now read

$$\left. \frac{d\bar{\phi}_{in}}{d\bar{r}} \right|_{\bar{r}=0} = 0, \tag{3.15}$$

$$\eta \left. \frac{d\bar{\phi}_{out}}{d\bar{r}} \right|_{\bar{r}=1} - \left. \frac{d\bar{\phi}_{in}}{d\bar{r}} \right|_{\bar{r}=1} = -\bar{\sigma}_s, \tag{3.16}$$

$$\bar{\phi}_{in}\big|_{\bar{r}=1} = \bar{\phi}_{out}\big|_{\bar{r}=1}, \tag{3.17}$$

$$\left. \frac{d\bar{\phi}_{out}}{d\bar{r}} \right|_{\bar{r}=\bar{R}_{out}} = 0. \tag{3.18}$$

Figure 3.1b shows the sketch of the non-dimensionalized boundary value problem (BVP) where the PB equation in Eq. 3.13 is simplified (linearized) to the Debye-Hückel (DH) equation valid in the weakly-charged regime:

$$\frac{1}{\bar{r}} \frac{d}{d\bar{r}} \left(\bar{r} \frac{d\bar{\phi}_{in}}{d\bar{r}} \right) = \frac{1}{\bar{\lambda}_D^2} \bar{\phi}_{in}. \tag{3.19}$$

The general solution for $\bar{\phi}_{in}$ and $\bar{\phi}_{out}$ is given as

$$\bar{\phi}_{in} = A_1 I_0 \left(\frac{\bar{r}}{\bar{\lambda}_D} \right) + B_1 K_0 \left(\frac{\bar{r}}{\bar{\lambda}_D} \right), \tag{3.20}$$

$$\bar{\phi}_{out} = A_2 \ln(\bar{r}) + B_2, \tag{3.21}$$

where $I_0(x)$ and $K_0(x)$ are the zeroth-order modified Bessel functions of the first and second kind, respectively, and A_1, B_1, A_2, and B_2 are constants. Following BC 3.15 and considering the limits $I_0(x) \to 0$ and $K_0(x) \to \infty$ as $x \to 0$, Eq. 3.20 reduces to

$$\bar{\phi}_{in} = A_1 I_0 \left(\frac{\bar{r}}{\bar{\lambda}_D} \right). \tag{3.22}$$

Next, the derivative of $\bar{\phi}_{out}$ vanishes at $\bar{r} = \bar{R}_{out}$. From Eq. 3.18, we see that

$$A_2 = 0, \tag{3.23}$$

and so

$$\bar{\phi}_{out} = B_2. \tag{3.24}$$

Considering the BC 3.17, we find

$$A_1 I_0 \left(\frac{1}{\bar{\lambda}_D} \right) = B_2. \tag{3.25}$$

The final BC 3.16 results in

$$A_1 = \frac{\bar{\sigma}_s \bar{\lambda}_D}{I_1(\frac{1}{\bar{\lambda}_D})}, \tag{3.26}$$

where $I_1(x)$ is the first-order modified Bessel function of the first kind obtained by differentiating $I_0(x)$ once. Therefore, the expressions for $\bar{\phi}_{in}$ and $\bar{\phi}_{out}$ are

$$\bar{\phi}_{in} = \bar{\sigma}_s \bar{\lambda}_D \frac{I_0 \left(\frac{\bar{r}}{\bar{\lambda}_D} \right)}{I_1(\frac{1}{\bar{\lambda}_D})}, \tag{3.27}$$

$$\bar{\phi}_{out} = \bar{\sigma}_s \bar{\lambda}_D \frac{I_0(\frac{1}{\bar{\lambda}_D})}{I_1(\frac{1}{\bar{\lambda}_D})}. \tag{3.28}$$

In Fig. 3.2, $\bar{\phi}$ is plotted against $\bar{r}$ computed for this one-dimensional BVP both analytically and numerically using the electrostatics interface under the AC/DC branch in COMSOL Multiphysics. The BVP is numerically represented using a one-dimensional axisymmetric model with a mesh size of 3.35×10^{-10} m. Reference values of R_{in}, R_{out}, λ_D, ϵ_{in}, ϵ_{out}, σ_s, and $\tilde{z}$ are listed in Table 3.1 and employed for the computation. The excellent agreement between the two curves validates the numerical model of the BVP which serves as a benchmark for the analysis conducted in the following sections. Numerical details pertaining to the model simulations in this thesis are given in Appendix B.

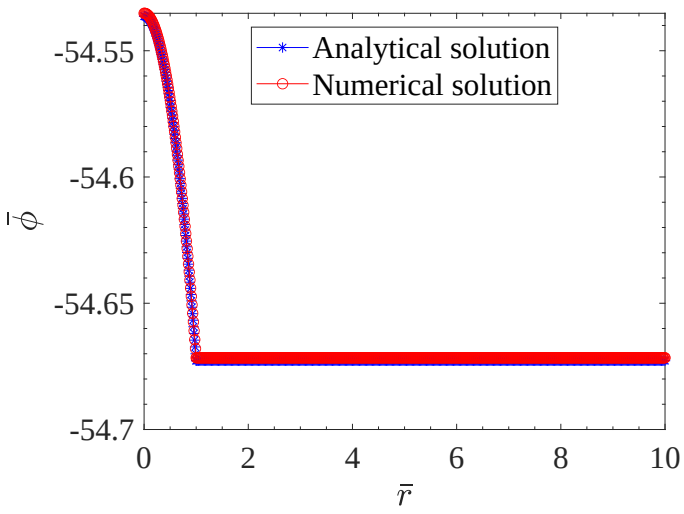

Figure 3.2: $\bar{\phi}$ is plotted against $\bar{r}$ to compare the analytical and numerical solutions for a one-dimensional nanochannel embedded in a dielectric medium.

Table 3.1: Reference parameters used for the study.

Parameter	**Description**	**Value**
R_{in}	Radius of the nanochannel	5 nm
R_{out}	Radius of the dielectric medium	50 nm
L	Length of the nanochannel	100 nm
λ_D	Debye length	50 nm
ϵ_{in}	Permittivity of nanochannel	$80\epsilon_0$ F/m
ϵ_{out}	Permittivity of dielectric medium	$100\epsilon_0$ F/m
σ_s	Surface charge density	-1.0×10^{-3} C/m^2
$\tilde{z}$	Valency of the electrolyte	1
T	Temperature	300 K

3.2 Finite, single nanochannel

Figure 3.3 shows a two-dimensional axisymmetric system defined on a $r-z$ plane. It consists of a long nanochannel (Ω_1) with a high aspect ratio, $L \gg R_{in}$ (or $\bar{L} \gg 1$), surrounded by a dielectric medium (Ω_2), and connected to two reservoirs (Ω_3) at the entrances, responsible for maintaining chemical equilibrium with the nanochannel. The electric potential $\phi_{in}(r,z)$ in the regions Ω_1 and Ω_3 are governed by the two-dimensional PB equation,

$$\frac{1}{r}\frac{\partial}{\partial r}\left(r\frac{\partial \phi_{in}}{\partial r}\right)+\frac{\partial^2 \phi_{in}}{\partial z^2}=\frac{2\tilde{z}ec_0}{\epsilon_{in}}\sinh\left(\frac{\tilde{z}e\phi_{in}}{k_BT}\right). \tag{3.29}$$

The z-coordinate and the length of the reservoir are normalized by R_{in} as

$$\bar{z} = \frac{z}{R_{in}}, \tag{3.30}$$

$$\bar{L}_{out} = \frac{L_{out}}{R_{in}}. \tag{3.31}$$

This results in the normalized PB equation,

$$\frac{1}{\bar{r}}\frac{\partial}{\partial \bar{r}}\left(\bar{r}\frac{\partial \bar{\phi}_{in}}{\partial \bar{r}}\right)+\frac{\partial^2 \bar{\phi}_{in}}{\partial \bar{z}^2}=\frac{1}{\bar{\lambda}_D^2}\sinh\left(\bar{\phi}_{in}\right). \tag{3.32}$$

The electric potential $\phi_{out}(r,z)$ in the region Ω_2 is governed by the Laplace equation, which in the normalized form reads

$$\frac{1}{\bar{r}}\frac{\partial}{\partial \bar{r}}\left(\bar{r}\frac{\partial \bar{\phi}_{out}}{\partial \bar{r}}\right)+\frac{\partial^2 \bar{\phi}_{out}}{\partial \bar{z}^2}=0. \tag{3.33}$$

The normalized BCs governing the problem are

$$\left.\frac{\partial \bar{\phi}_{in}}{\partial \bar{r}}\right|_{\bar{r}=0} = 0, \tag{3.34}$$

$$\eta(\mathbf{n}\cdot\nabla\bar{\phi}_{out})\big|_{\bar{r}=1,\ ,0\le\bar{z}\le\bar{L}} - (\mathbf{n}\cdot\nabla\bar{\phi}_{in})\big|_{\bar{r}=1,0\le\bar{z}\le\bar{L}} = -\bar{\sigma}_s, \tag{3.35}$$

$$\bar{\phi}_{in}\big|_{\bar{r}=1,0\le\bar{z}\le\bar{L}} = \bar{\phi}_{out}\big|_{\bar{r}=1,0\le\bar{z}\le\bar{L}}, \tag{3.36}$$

$$\left.\frac{\partial \bar{\phi}_{out}}{\partial \bar{r}}\right|_{\bar{r}=\bar{R}_{out}} = 0, \tag{3.37}$$

$$\eta\left(\mathbf{n}\cdot\nabla\bar{\phi}_{out}\right)\big|_{1\le\bar{r}\le\bar{R}_{out},\,\bar{z}=0} - (\mathbf{n}\cdot\nabla\bar{\phi}_{in})\big|_{1\le\bar{r}\le\bar{R}_{out},\,\bar{z}=0} \tag{3.38}$$

$$= \eta\left(\mathbf{n}\cdot\nabla\bar{\phi}_{out}\right)\big|_{1\le\bar{r}\le\bar{R}_{out},\bar{z}=\bar{L}} - (\mathbf{n}\cdot\nabla\bar{\phi}_{in})\big|_{1\le\bar{r}\le\bar{R}_{out},\bar{z}=\bar{L}} = 0,$$

$$\bar{\phi}_{in}\big|_{\bar{z}=\bar{L}+\bar{L}_{out}} = \bar{\phi}_{in}\big|_{\bar{z}=-\bar{L}_{out}} = 0, \tag{3.39}$$

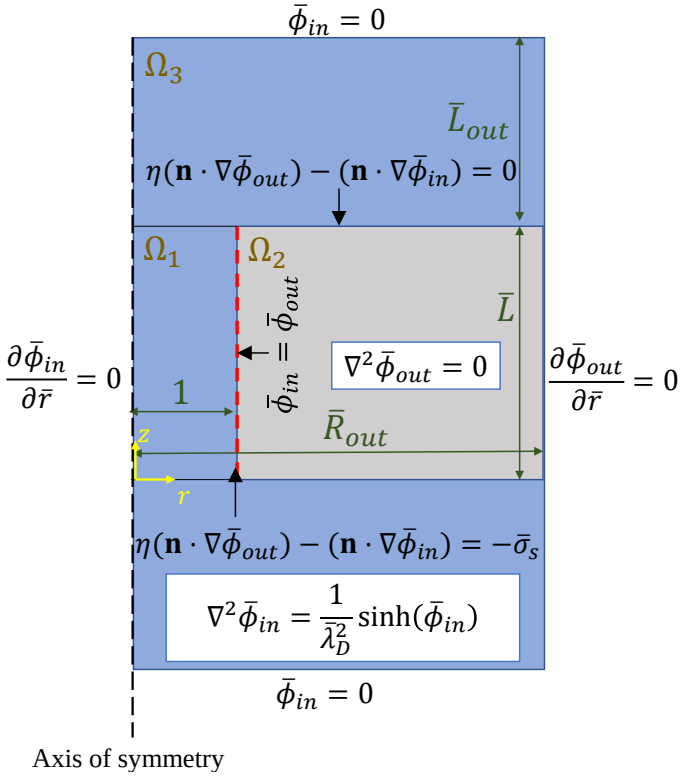

Figure 3.3: Sketch of an axisymmetric nanochannel (Ω_1) embedded in a dielectric medium (Ω_2) and maintained in chemical equilibrium with reservoirs (Ω_3) at the ends. All geometrical parameters are normalized with respect to the radius of the nanochannel.

where $\mathbf{n}$ is the unit normal vector pointing outward from the surface of the nanochannel.

A parametric study is performed to examine electroneutrality breakdown, discussed in the following sections, for a variety of nanochannel systems concerning a wide range of applications, such as water desalination, biosensors, and biomimetic materials. The ranges of parameters are listed in Table 3.2 and selected based on the actual materials. For most ion transport systems, R_{in} is considered to be 5 nm [6, 10, 108, 109]. It is not varied independently since the other geometric parameters in the system inherently scale with it. R_{out} ranges from 10 nm to 50 nm. This range is frequently encountered in applications such as water desalination, nanofiltration, and fuel cells [110–112]. We vary the nanochannel length L across an order of magnitude, allowing

Table 3.2: Range of parameters employed for the parametric study.

Parameter	**Description**	**Range**
R_{out}	Radius of the dielectric medium	10 to 50 nm
L	Length of the nanochannel	10 to 100 nm
λ_D	Debye length	0.5 to 50 nm
ϵ_{out}	Permittivity of dielectric medium	ϵ_0 to $100\epsilon_0$ F/m
σ_s	Surface charge density	-1.0×10^{-1} to -1.0×10^{-3} C/m^2

us to analyze both low and high aspect ratio (L/R_{in}) nanostructures. A channel length of $L = 100$ nm and a radius $R_{in} = 5$ nm is considered sufficient to represent an extremely long nanochannel in relation to its radius. Further extending the length for simulation would only have a marginal effect on the electrostatics within the channel. We explore systems with a broad spectrum of bulk ionic concentrations c_0, extending from 2.3×10^{22} m^{-3} (≈ 0.04 mM) to 2.3×10^{26} m^{-3} (≈ 400 mM), as reported in previous studies [69, 71, 113]. These concentrations, in turn, yield Debye lengths λ_D in the range of 0.5 nm to 50 nm for $\epsilon_{in} = 80\epsilon_0$ F/m, $T = 300$ K, and $\tilde{z} = 1$. The dielectric permittivity outside the nanochannel, ϵ_{out}, spans from ϵ_0 F/m to $100\epsilon_0$ F/m, encompassing a diverse array of dielectric materials such as polymers, nanocomposites, ceramics, and metal oxides [111, 112, 114]. The surface charge density σ_s considered for this study lies between -1.0×10^{-1} C/m^2 and -1.0×10^{-3} C/m^2, representing nanochannel systems with a wide spectrum of surface charge densities [69, 95, 108, 109]. Note that the limiting trends in Appendix A are also helpful in selection of the parameter ranges discussed above.

A set of parameter values from Table 3.2 were selected and listed in Table 3.1, as they led to the highest breakdown. These parameters are collectively referred to as the reference parameters for the COMSOL simulations.

3.3 Electroneutrality Breakdown

Electroneutrality breakdown within a nanochannel is quantified by the ratio $|Q_{in}/Q_{out}|$ i.e., the ratio of Q_{in}, which is the volume integral over the charge density within the nanochannel, and Q_{out}, which is the surface integral over the charge density along the surface of the nanochannel. As the charges within the nanochannel are related to the electric potential through the PB equation, Q_{in} can be calculated, mathematically, as

$$Q_{in} = -\int_V \epsilon_{in}\nabla^2\phi_{in}dV, \tag{3.40}$$

where V is the volume of the nanochannel. Using the Divergence Theorem, Q_{in} can be rewritten into the sum of three surface integrals

$$Q_{in} = -\int_I \epsilon_{in}\nabla\phi_{in}\cdot\mathbf{n}\,dA - \int_{II} \epsilon_{in}\nabla\phi_{in}\cdot\mathbf{n}\,dA - \int_{III} \epsilon_{in}\nabla\phi_{in}\cdot\mathbf{n}\,dA, \tag{3.41}$$

where boundaries I, II, and III are indicated in Fig. 3.4. Recall that the BC at III is

$$\epsilon_{out}(\mathbf{n}\cdot\nabla\phi_{out}) - \epsilon_{in}.(\mathbf{n}\cdot\nabla\phi_{in}) = -\sigma_s. \tag{3.42}$$

If $\int_I \epsilon_{in}\nabla\phi_{in}\cdot\mathbf{n}\,dA$, $\int_{II}\epsilon_{in}\nabla\phi_{in}\cdot\mathbf{n}dA$, and $\epsilon_{out}(\mathbf{n}\cdot\nabla\phi_{out})$ were negligible, it can be easily shown that Q_{in} equals Q_{out} in magnitude. Specifically, using Eqs. 3.41 and 3.42 with its first term neglected,

$$\begin{aligned} Q_{in} &= -\int_{III}\epsilon_{in}\nabla\phi_{in}\cdot\mathbf{n}\,dA \\ &= -\int_{III}\sigma_s\cdot\mathbf{n}\,dA \\ &= -\sigma_s 2\pi R_{in}L \\ &= -Q_{out}. \end{aligned} \tag{3.43}$$

In other words, electroneutrality is maintained when the entrance effects are negligible ($\int_I \epsilon_{in}\nabla\phi_{in}\cdot\mathbf{n}\,dA = \int_{II}\epsilon_{in}\nabla\phi_{in}\cdot\mathbf{n}\,dA \to 0$), in addition to the first term of Eq. 3.42 being negligible, i.e., $\epsilon_{out}(\mathbf{n}\cdot\nabla\phi_{out}) \to 0$.

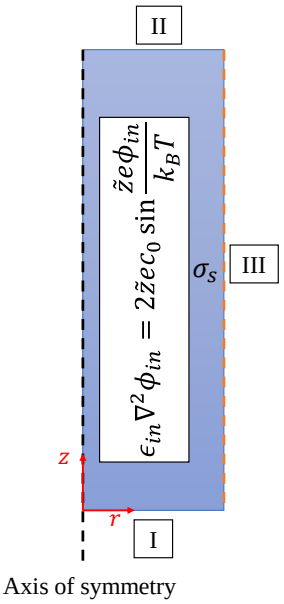

Figure 3.4: An axisymmetric model of a nanochannel with surface charge density σ_s defined on the $r-z$ plane. Boundaries I and II are the top and bottom entrances of the channel while boundary III is the channel wall with surface charge density σ_s.

More generally, with the help of Eq. 3.42, Eq. 3.41 can be written as

$$\begin{aligned} Q_{in} &= -\int_I \epsilon_{in}\nabla\phi_{in}\cdot\mathbf{n}\,dA - \int_{II} \epsilon_{in}\nabla\phi_{in}\cdot\mathbf{n}\,dA - \int_{III} \epsilon_{out}\nabla\phi_{out}\cdot\mathbf{n}\,dA - \int_{III} \sigma_s\cdot\mathbf{n}\,dA \\ &= -\int_I \epsilon_{in}\nabla\phi_{in}\cdot\mathbf{n}\,dA - \int_{II} \epsilon_{in}\nabla\phi_{in}\cdot\mathbf{n}\,dA - \int_{III} \epsilon_{out}\nabla\phi_{out}\cdot\mathbf{n}\,dA - Q_{out} \\ &= -2\int_I \epsilon_{in}\nabla\phi_{in}\cdot\mathbf{n}\,dA - \int_{III} \epsilon_{out}\nabla\phi_{out}\cdot\mathbf{n}\,dA - Q_{out}. \end{aligned} \tag{3.44}$$

The terms in Eq. 3.44 are computed in Table 3.3 for the reference parameters. $|Q_{in}/Q_{out}|$ is evaluated to be approximately 0.02, which results in a very high electroneutrality breakdown for the given BVP in Sec. 3.2. By examining these terms separately, a more comprehensive understanding of the underlying factors contributing to the breakdown can be gained. Electroneutrality breakdown occurs when the electric field leaks into the reservoir (first integral in the last line of Eq. 3.44) or into the surrounding medium (second integral). "Electric field leakage" refers to the phenomenon where electric fields extend into the dielectric medium surrounding a confined electrolyte or the reservoirs connected to the channel entrances, rather than being fully screened

Table 3.3: Values computed for the terms in Eq. 3.44 for the set of parameters listed in Table 3.1.

Term	**Value**
Q_{in}	$6.42 \times 10^{-20}\,\mathrm{C}$
Q_{out}	$-3.14 \times 10^{-18}\,\mathrm{C}$
$2\int_I \epsilon_{in}\nabla\phi_{in}\cdot\mathbf{n}\,dA$	$9.46 \times 10^{-20}\,\mathrm{C}$
$\int_{III} \epsilon_{out}\nabla\phi_{out}\cdot\mathbf{n}\,dA$	$2.98 \times 10^{-18}\,\mathrm{C}$

by the electrolyte itself. The integrals in Eq. 3.44 are computed using the gradients $\nabla\phi_{in}$ and $\nabla\phi_{out}$ obtained from the COMSOL simulation. Q_{out} is computed using the surface charge density σ_s employed in the simulation. The last three terms listed in Table 3.3 can, therefore, be utilized to calculate Q_{in} according to Eq. 3.44. On the other hand, Q_{in} can also be evaluated directly from the integral in Eq. 3.40 from the COMSOL simulation, which is the value given in Table 3.3. A numerical error of approximately 2% is found when compared to the computed Q_{in} according to Eq. 3.44, using the terms in Table 3.3.

Equation 3.44 can be rearranged into

$$1 = -q_{ex}^1 - q_{ex}^2 - \frac{Q_{out}}{Q_{in}}, \tag{3.45}$$

where

$$q_{ex}^1 = \frac{2\int_I \epsilon_{in}\nabla\phi_{in}\cdot\mathbf{n}\,dA}{Q_{in}}, \tag{3.46}$$

$$q_{ex}^2 = \frac{\int_{III} \epsilon_{out}\nabla\phi_{out}\cdot\mathbf{n}\,dA}{Q_{in}}. \tag{3.47}$$

q_{ex}^1 and q_{ex}^2 signify the excess leakage from the channel entrances and its surface, respectively[1]. Thus, electroneutrality is a result of the collective leakage through the nanochannel entrances and its surface. For an extremely long nanochannel, entrance effects are usually neglected on the presumption that leakage through the surface of

[1]Note that $\frac{Q_{out}}{Q_{in}}$ in Eq. 3.45 is greater than 1 during breakdown, hence q_{ex}^1 and q_{ex}^2 can have values greater than 1 as well.

the nanochannel dominates [89]. This assumption may not be valid for nanochannels of arbitrary dimensions as shown in the following sections.

Q_{in} is the total charge within the nanochannel which, as listed in Table 3.3, is only about 1/3 of the elementary charge. With such small charges within the nanochannel, electrostatic forces will be weakened, resulting in ion-ion correlation effects (see Sec. 2.3.2). Following the mean-field approach, our model assumes that the behavior of each ion is independent of the other ions present in the system and, thus, does not take ion-ion correlations into account. Therefore, the reference parameters from Table 3.1 do not seem to align completely with the continuum approach, and form an extreme scenario where the electroneutrality breakdown is significant, with $|Q_{in}/Q_{out}|$ approaching zero. Nevertheless, these parameters are utilized because of their potency in revealing significant trends of electroneutrality breakdown. The approach of analyzing the terms in Eq. 3.45 will continue to be used in the following section to shed light on the complex interplay of phenomena while inducing the electroneutrality breakdown.

3.4 Phase diagrams for a single nanochannel

A phase diagram is a graphical representation of a function of two variables that describes the state of a physical system. For example, in Fig. 3.5a, $|Q_{in}/Q_{out}|$ is plotted as a function of $\bar{L}$ and $\bar{R}_{out}$. As was discussed in the previous section, the electroneutrality breakdown increases as $|Q_{in}/Q_{out}|$ gets smaller. These diagrams help visualize the trend of this breakdown as important physical parameters of the system vary.

Figure 3.5a depicts the effect of channel dimensions on the electroneutrality breakdown. It shows that $|Q_{in}/Q_{out}|$ is negatively correlated with $\bar{R}_{out}$ but positively correlated with $\bar{L}$. Figure 3.5b illustrates the effect of properties of the dielectric media on the electroneutrality breakdown by plotting $|Q_{in}/Q_{out}|$ as a function of η and $\bar{R}_{out}$. The figure shows that $|Q_{in}/Q_{out}|$ decreases with increasing η and $\bar{R}_{out}$.

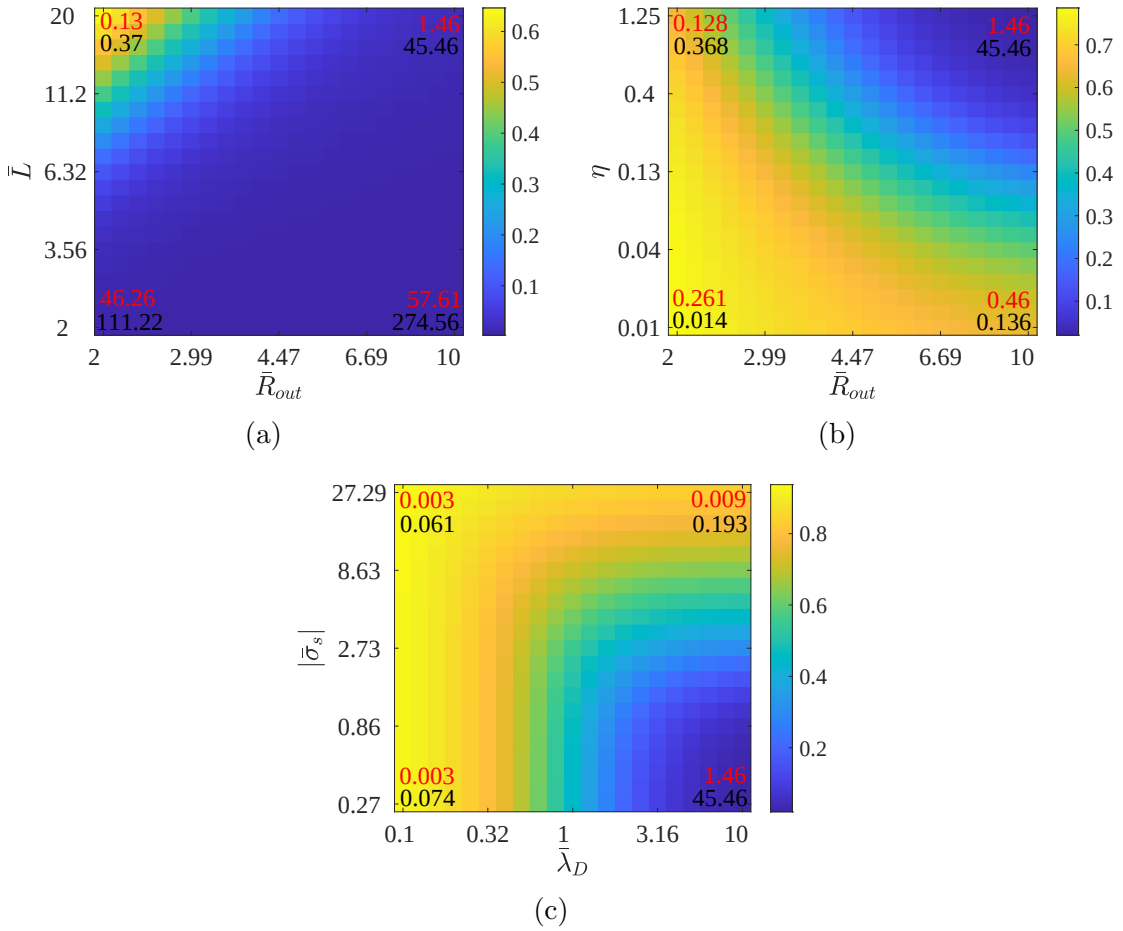

Figure 3.5: Log-log plots of $|Q_{in}/Q_{out}|$ as a function of (a) $\bar{R}_{out}$ and $\bar{L}$, (b) $\bar{R}_{out}$ and η, (c) $\bar{\lambda}_D$ and $\bar{\sigma}_s$. The numbers in the four corners of the plots correspond to q^1_{ex} in red and q^2_{ex} in black for the four limiting cases of each plot. The other fixed parameters for each phase diagram are listed in Table 3.1.

Figure 3.5c portrays the effect of the ionic concentration within the nanochannel and the magnitude of the charge density on the surface of the nanochannel. It shows that $|Q_{in}/Q_{out}|$ decreases with increasing $|\bar{\sigma}_s|$, while it increases with increasing $\bar{\lambda}_D$.

Each diagram in Fig. 3.5 has four extreme cases for which q_{ex}^1 (red) and q_{ex}^2 (black) are computed and shown in the four corners of the diagrams. In Fig. 3.5a, a shorter channel facilitates the escape of charges from the channel into the reservoir which results in lesser charges within the channel. This is indicated by the much higher q_{ex}^1 and q_{ex}^2 for $\bar{L} = 2$ compared to a channel with $\bar{L} = 20$. q_{ex}^2 increases with the radius of the surrounding dielectric medium $\bar{R}_{out}$. Because the electric field is set to vanish at the outer boundary of the dielectric medium, a thinner dielectric medium with $\bar{R}_{out} = 2$ restricts the extent to which the electric field can leak from the channel wall, leading to a higher concentration of charges within the channel as compared to thicker dielectric medium with $\bar{R}_{out} = 10$. Therefore, the system with a thinner dielectric medium ($\bar{R}_{out} = 2$) leans towards maintaining electroneutrality while a thicker dielectric medium ($\bar{R}_{out} = 10$) drives the system towards the breakdown of electroneutrality. Thus, a system with a short nanochannel surrounded by a thick dielectric medium is more prone to electroneutrality breakdown. This finding has a bearing on channel coupling in arrays of nanochannels (see Chapter 5).

In Fig. 3.5b, the higher q_{ex}^2 values for $\eta = 1.25$ as compared to $\eta = 0.01$ is due to the direct relationship of q_{ex}^2 with ϵ_{out} in Eq. 3.47. Higher leakage from the channel wall results in higher electroneutrality breakdown in this case. In Fig 3.5c, for high $|\bar{\sigma}_s|$, higher concentration of counterions screen the negative surface charge within the channel due to higher electrostatic attraction as compared to low $|\bar{\sigma}_s|$, thus, maintaining electroneutrality. A similar effect is observed for small $\bar{\lambda}_D$. The EDL is thin for small $\bar{\lambda}_D$, hence the concentration of counterions is high near the surface, effectively screening the charge of the wall. In a system with higher $\bar{\lambda}_D$ ($\bar{\lambda}_D = 10$), the ionic concentration c_0 is low and therefore, the ability of the electrolyte to screen the electric field created by the charged wall is significantly reduced. This, coupled

with low $|\bar{\sigma}_s|$, drives the system towards electroneutrality breakdown. Consequently, this is also established in the DH regime characterized by low $\bar{\sigma}_s$ and high $\bar{\lambda}_D$. Levy et. al [1] stated that very high electroneutrality breakdown is found in this regime which can also be concluded from the above discussion.

Overall, a system is more prone to electroneutrality breakdown when the nanochannel is short (low $\bar{L}$), containing a dilute electrolytic solution (high $\bar{\lambda}_D$), separated by a weakly charged interface (low $\bar{\sigma}_s$) from a thick dielectric medium (high $\bar{R}_{out}$) with high permittivity (high η).

The top left corner of Fig. 3.5a and the bottom right corner of Fig. 3.5b reveal an interesting insight into the breakdown of electroneutrality. In both cases, $|Q_{in}/Q_{out}|$ of approximately 0.6 is observed. However, it is important to note that these points correspond to different parameter combinations, and their impacts on the breakdown are distinct. The variations become evident when the leakages, denoted as q^1_{ex} and q^2_{ex}, are examined for these parameter combinations. In Fig. 3.5a, it is found that q^2_{ex} dominates over q^1_{ex}, whereas in Fig. 3.5b, q^1_{ex} dominates over q^2_{ex}. This shows that comprehensive information about the electric field distribution around a nanochannel cannot be provided by the magnitude of $|Q_{in}/Q_{out}|$ alone. In other words, a similar value of $|Q_{in}/Q_{out}|$ can be obtained from various combinations of q^1_{ex} and q^2_{ex}. This underscores the necessity for a deeper understanding of the underlying parameters and their effect on electroneutrality breakdown in nanochannels.

3.5 Steric Effects

In nanochannels with finite-size ions subject to high bulk concentrations (c_0) and significant surface charge densities (σ_s), an accumulation of counterions near the channel surface occurs, leading to saturation of counterions. This accumulation gives rise to steric effects as a consequence, where the ions can no longer be considered as point-like charges (see Sec. 2.3.2). The influence of steric effects on ion transport properties can be substantial, underscoring the significance of investigating the physical charac-

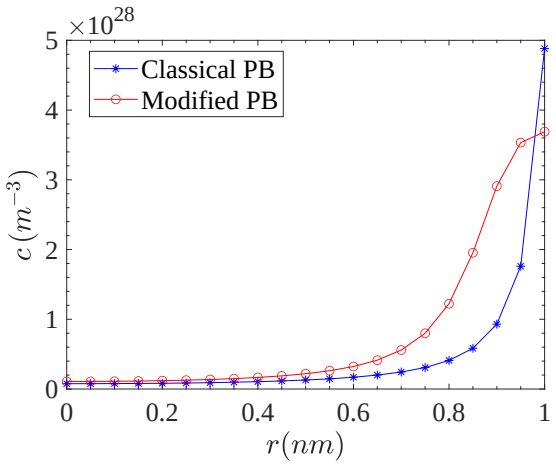

Figure 3.6: Radial profile of the concentration of counter-ions predicted from both the classical and modified Poisson-Boltzmann equations within the nanochannel in Fig. 3.3.

teristics of nanochannels that contribute to the emergence of these effects [115–118]. The classical PB equation (Eq. 2.14) considers zero-size ions while the modified PB equation (Eq. 2.24) accounts for the finite-size ions within the nanochannel. Note that the model utilizing the modified PB equation assumes $a_0 = 0.3\,\text{nm}$ [69, 119].

Steric effects become apparent in the model illustrated in Fig. 3.3 under the conditions of small channel size, high bulk concentration, and high surface charge density. For instance, Fig. 3.6 displays the radial distribution of counterion concentration (c) for nanochannels with the following parameters: $R_{in} = 1\,\text{nm}$, $R_{out} = 2\,\text{nm}$, $L = 100\,\text{nm}$, $\epsilon_{in} = 80\epsilon_0\,\text{F/m}$, $\epsilon_{out} = 100\epsilon_0\,\text{F/m}$, $\lambda_D = 0.5\,\text{nm}$, $\tilde{z} = 1$ and $\sigma_s = -1.0\,\text{C/m}^2$. The radial distribution curves are obtained from the solutions of the classical and modified PB equations, respectively. It is clear that the modified PB equation predicts saturation behavior depicted by plateauing of the concentration curve near $r = 1\,\text{nm}$, while the classical PB equation yields concentrations (c) higher than the saturation curve. This discrepancy highlights the limitations of the classical PB equation in accurately describing the ion distribution near the channel surface. Considering the electroneutrality trends discussed in the earlier sections, the system tends towards electroneutrality under the influence of large σ_s and c_0. Consequently,

for this particular case, the absolute value of Q_{in}/Q_{out} is approximately 0.93 for both the classical and the modified PB equations. From this, it can be concluded that steric effects are significant when the nanochannel is close to being electroneutral. In other words, steric effects do not play a substantial role when the system, depicted in Fig. 3.3, deviates from electroneutrality. However, steric effects may play a role in electroneutrality breakdown outside the applicability of continuum models such as sub-nanometer nanochannels.

3.6 Effect of temperature

Some devices involving nanochannels operate at elevated temperatures. For example, PEM and fuel cells typically function at 353 K [120–122]. This motivates an exploration of the electroneutrality breakdown trends for the range of physical parameters listed in Table 3.2 at $T = 353\,\mathrm{K}$ for a single nanochannel as discussed in Sec. 3.2. The left and the right panels of the phase diagrams in Fig. 3.7 show the electroneutrality breakdown trend for the BVP in Fig. 3.3 at $T = 353\,\mathrm{K}$ and $T = 300\,\mathrm{K}$, respectively. Figures 3.7a and 3.7b illustrate the $|Q_{in}/Q_{out}|$ trends for varying $\bar{L}$ and $\bar{R}_{out}$ for the two temperature settings, which remains the same except for a small shift towards breakdown for increasing $\bar{R}_{out}$ and decreasing $\bar{L}$ when the temperature is higher. This is seen by an increase of the dark blue region (or a decrease in the yellow region) towards the limiting case of $\bar{R}_{out} = 2$ and $\bar{L} = 20$. Figures 3.7c and 3.7d exhibit the influence of $|\bar{\sigma}_s|$ and $\bar{\lambda}_D$ on $|Q_{in}/Q_{out}|$ for the elevated and the room temperature, respectively. The pattern of the breakdown remains consistent across both temperatures, albeit the more likelihood of breakdown at higher temperatures. This shift is highlighted by the expansion of the blue, green, and orange regions towards $|\bar{\sigma}_s| = 27.29$ and $\bar{\lambda}_D = 0.1$. In Figs. 3.7e and 3.7f, $|Q_{in}/Q_{out}|$ is illustrated as a function of η and $\bar{R}_{out}$ for the two temperature settings. The breakdown of electroneutrality is more significantly influenced by η in Fig. 3.7e as compared to Fig. 3.7f shown by the expansion of the dark blue region towards $\eta = 0.01$ and $\bar{R}_{out} = 2$.

The observed shifts towards electroneutrality breakdown can be linked to the rise in the kinetic energy of ions as temperature increases. With enhanced kinetic energy, ions can more readily migrate toward the reservoir, leaving behind fewer counterions within the nanochannel to screen the surface charge on the channel wall. This is further confirmed by the normalization of ϕ, where a temperature increase results in a decrease in $\bar{\phi}$. In this manner, the system gets closer to the DH regime, as expressed in Eq. 3.19. As discussed in Sec. 3.4, the system tends towards electroneutrality breakdown as it approaches the DH regime.

Further understanding of the effect of temperature can be gained by considering the Helmholtz free energy of the system. As elucidated in Sec. 2.3, within the context of the free energy formulation $\mathcal{F} = U - TS$, an increase in temperature (T) imparts greater thermal energy to the system and consequently increases the entropic contribution (TS) to the free energy. With this surge in entropic contribution due to thermal fluctuations, ions are unable to maintain strict electroneutrality configurations. This behavior propels the system towards a state of electroneutrality breakdown.

The model for a single nanochannel in this chapter explicitly incorporates a surrounding dielectric medium, which holds a crucial role in influencing the electroneutrality breakdown. In 2020, Levy et al. [1] proposed a Robin boundary condition to simplify the simulations of single nanochannels by eliminating the dielectric medium from the model. Despite its simplicity, the assumptions used in the derivation of the boundary condition are problematic and can have huge implications on the electroneutrality breakdown. In the next chapter, we discuss this issue and emphasize the need to explicitly include the dielectric medium in the model.

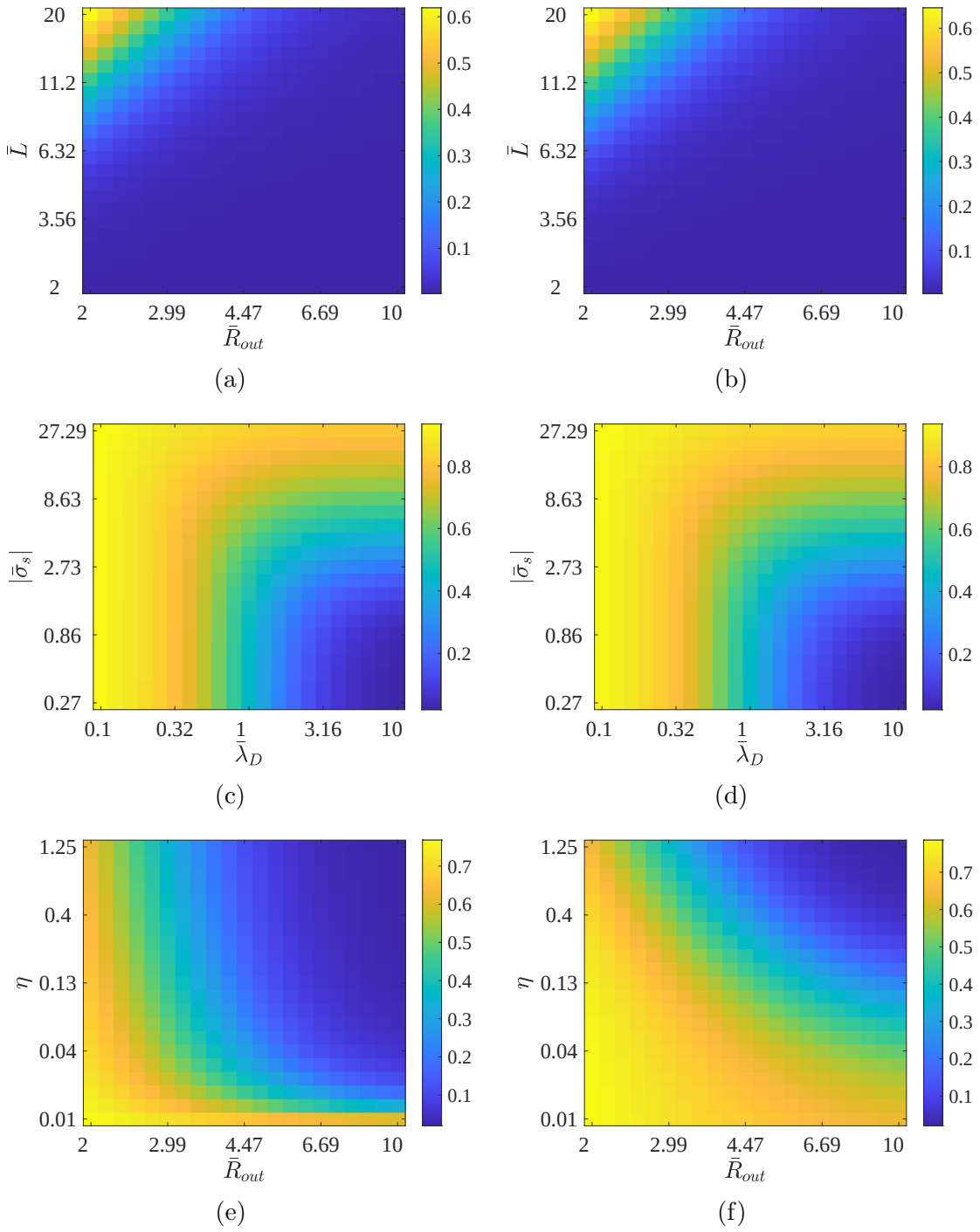

Figure 3.7: Log-log plots of $|Q_{in}/Q_{out}|$ as a function of (a) & (b) $\bar{L}$ and $\bar{R}_{out}$, (c) & (d) $|\bar{\sigma}_s|$ and $\bar{\lambda}_D$, and (e) & (f) η and $\bar{R}_{out}$ for $T = 353\,\mathrm{K}$ (left panel) and $T = 300\,\mathrm{K}$ (right panel). The other parameters are listed in Table 3.1.

Chapter 4

Need for explicitly modelling the dielectric medium surrounding the nanochannel

In recent work, Levy et al. [1] examined an important assumption usually made in the modeling of electrolytes in a charged nanochannel, namely the electroneutrality of the nanochannel-electrolyte system. This assumption usually neglects the presence of the medium surrounding the nanochannel, as the boundary condition imposed on the surface of the nanochannel implicitly assumes that the electric field in the surrounding medium is zero. In essence, the surface charge of the nanochannel is completely neutralized by the counterions in the pore. Via an in-depth investigation, Levy et al. [1] proved that electroneutrality can be violated either within a cross-section or even globally on the scale of the entire nanochannel. This work is valuable and has raised awareness about the important issue of electroneutrality breakdown. While the work is also comprehensive and valid overall, we discuss a particular issue of the contribution in this chapter. Specifically, recognizing that the inclusion of the surrounding medium complicates the BVP, Levy et al. propose a Robin boundary condition (Eq. 4.1) at the surface of the nanochannel, which offers an opportunity to eliminate the need to compute the electric field in the surrounding medium:

$$\frac{\partial \phi_{in}}{\partial r}(R_{in}, z) = \frac{\sigma_s}{\epsilon_{in}} - \frac{\epsilon_{out}}{\epsilon_{in}} \frac{\phi_{in}(R_{in})}{R_{in} M_{L/R_{in}}} \tag{4.1}$$

Despite its simplicity, in this chapter, we point out that the approximations that lead to the proposed boundary condition can be flawed and care should be taken when using it.

Figure 4.1a shows the axisymmetric system under consideration, consisting of a nanochannel of radius R_{in} and length L with surface charge density σ_s and permittivity ϵ_{in}, embedded in a dielectric medium with permittivity ϵ_{out}. The nanochannel is connected to and in equilibrium with an external reservoir which has the same permittivity ϵ_{in} and a bulk ion concentration of c_0. The electric potential ϕ is governed by the PB equation in Ω (domain for the nanochannel and reservoir) and the Laplace equation in the dielectric medium. For the symmetric monovalent electrolyte considered in [1], the equations are

$$\epsilon_{in}\nabla^2\phi_{in}(\mathbf{r}) = 2c_0 e \sinh\left(\frac{e\phi_{in}(\mathbf{r})}{k_B T}\right) \qquad \forall \mathbf{r} \in \Omega, \tag{4.2}$$

$$\epsilon_{out}\nabla^2\phi_{out}(\mathbf{r}) = 0 \qquad \forall \mathbf{r} \notin \Omega. \tag{4.3}$$

In deriving the boundary condition Eq. 4.1, Levy et al. [1] focused on the DH regime of the PB equation (i.e., weakly charged nanochannel) and considered a simplified BVP as shown in Fig. 4.1b. Here the external reservoir is removed and replaced by a Dirichlet condition ($\phi = 0$) at the channel opening. $\kappa_D = \sqrt{\frac{2c_0e^2}{\epsilon_{in}k_BT}}$ is the inverse of the Debye length, λ_D. Using azimuthal symmetry, exact solutions for ϕ_{in} and ϕ_{out} exist in the case $\phi \to 0$ as $r \to \infty$ in the form of series expansions:

$$\phi_{in}(r,z) = \sum_{n=1}^{\infty} A_n \sin(\omega_n z) I_0\left(\sqrt{\omega_n^2 + \kappa_D^2}\, r\right), \tag{4.4}$$

$$\phi_{out}(r,z) = \sum_{n=1}^{\infty} B_n \sin(\omega_n z) K_0(\omega_n R_{in}), \tag{4.5}$$

where $\omega_n = n\pi/L$, and $I_0(x)$ and $K_0(x)$ are the zeroth-order modified Bessel functions of the first and second kind, respectively. The constants A_n and B_n are obtained using

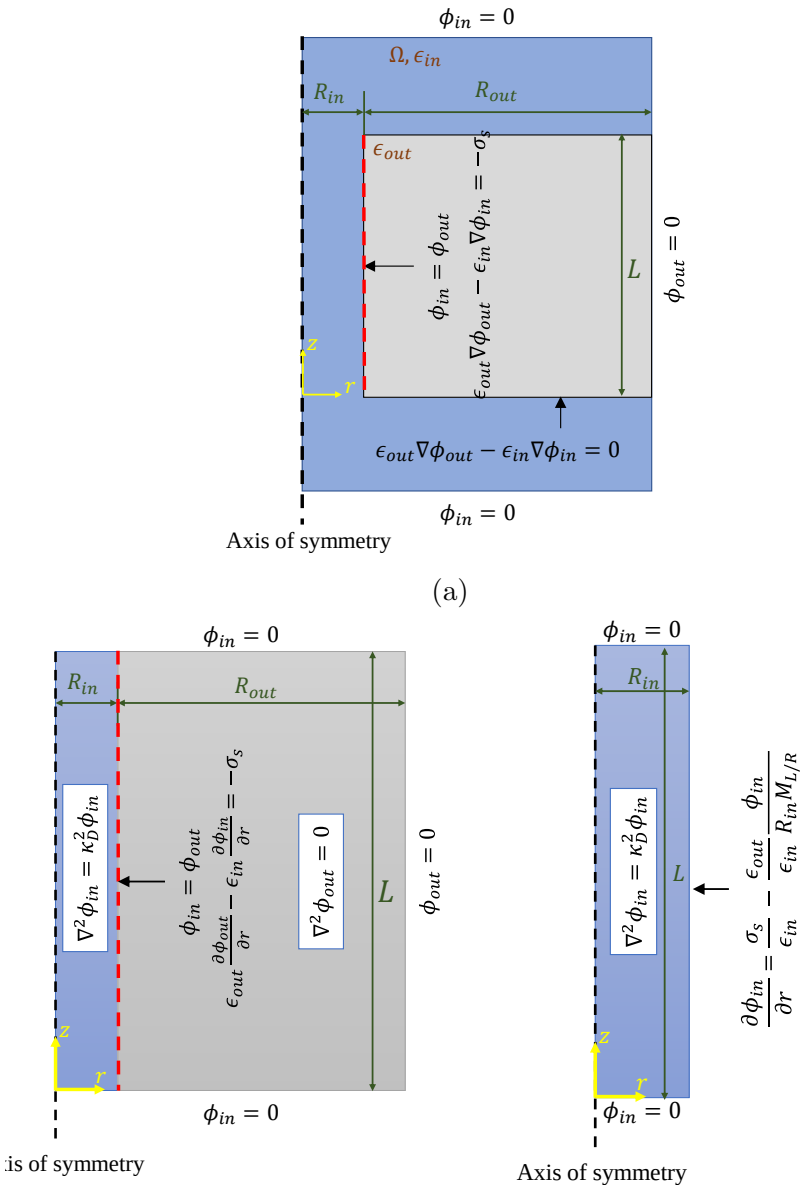

Figure 4.1: (a) Schematic of the system consisting of a nanochannel, surrounding dielectric medium and an external reservoir. (b) Boundary value problem discussed in Appendix A of [1] for a weakly charged cylinder embedded in a dielectric medium. (c) Boundary value problem discussed in Appendix B of [1] which differs from (b) by the replacement of the dielectric medium with a Robin boundary condition.

the boundary conditions in Fig. 4.1b, and are given by

$$A_n = \frac{4\sigma_s}{\omega_n L} \frac{K_0(\omega_n R_{in})}{\epsilon_{in}\sqrt{\omega_n^2+\kappa_D^2}K_0(\omega_n R_{in})I_1\left(\sqrt{\omega_n^2+\kappa_D^2}R_{in}\right)+\epsilon_{out}\omega_n I_0\left(\sqrt{\omega_n^2+\kappa_D^2}R_{in}\right)K_1(\omega_n R_{in})}, \quad (4.6)$$

$$B_n = \frac{4\sigma_s}{\omega_n L} \frac{I_0\left(\sqrt{\omega_n^2+\kappa_D^2}R_{in}\right)}{\epsilon_{in}\sqrt{\omega_n^2+\kappa_D^2}K_0(\omega_n R_{in})I_1\left(\sqrt{\omega_n^2+\kappa_D^2}R_{in}\right)+\epsilon_{out}\omega_n I_0\left(\sqrt{\omega_n^2+\kappa_D^2}R_{in}\right)K_1(\omega_n R_{in})}, \quad (4.7)$$

where $I_1(x)$ and $K_1(x)$ are the first-order modified Bessel functions of the first and second kind, respectively. The above solutions are also presented in Appendix A of [1], but there are typos in the expressions of A_n and B_n which are corrected in Eq. 4.6 and 4.7.

In Appendix B of [1], an attempt is made to further simplify the BVP in Fig. 4.1b to the one in Fig. 4.1c. For this purpose, the following series of approximations are made for $L/R_{in} \gg 1$:

$$K_0(\omega_n R_{in}) = K_0\left(\frac{n\pi R_{in}}{L}\right) \approx -\ln\left(\frac{n\pi R_{in}}{2L}\right) - \gamma, \quad (4.8)$$

$$-\ln\left(\frac{n\pi R_{in}}{2L}\right) - \gamma \approx -\ln\left(\frac{\pi R_{in}}{2L}\right) - \gamma \equiv M_{L/R_{in}}, \quad (4.9)$$

$$K_1(\omega_n R_{in}) = K_1\left(\frac{n\pi R_{in}}{L}\right) \approx \frac{L}{n\pi R_{in}}, \quad (4.10)$$

where γ is Euler's constant, approximately equal to 0.577. As an alternative to the derivation in Appendix B of [1], we offer a simple way to see how the approximations 4.8-4.10 lead to the BC in Eq. 4.1. Starting from Eq. 4.5 and using the continuity of ϕ at the channel wall for all values of z, which implies $A_n I_0\left(\sqrt{\omega_n^2+\kappa_D^2}R_{in}\right) = B_n K_0(\omega_n R_{in})$ from Eqs. 4.4 and 4.5, it can be easily shown that

$$\frac{\partial \phi_{out}}{\partial r}(R_{in}, z) = -\sum_{n=1}^{\infty} A_n \sin(\omega_n z) I_0\left(\sqrt{\omega_n^2+\kappa_D^2}R_{in}\right) \frac{\omega_n K_1(\omega_n R_{in})}{K_0(\omega_n R_{in})}. \quad (4.11)$$

Now, replacing $K_1(\omega_n R_{in})$ and $K_0(\omega_n R_{in})$ using Eqs. 4.8-4.10 reduces the term $\frac{\omega_n K_1(\omega_n R_{in})}{K_0(\omega_n R_{in})}$ to $\frac{1}{R_{in} M_{L/R_{in}}}$, i.e., a constant, allowing $\frac{\partial \phi_{out}}{\partial r}(R_{in}, z)$ to be directly proportional to ϕ_{in}. The jump condition in the electric displacement shown in Fig. 4.1b finally becomes Eq. 4.1.

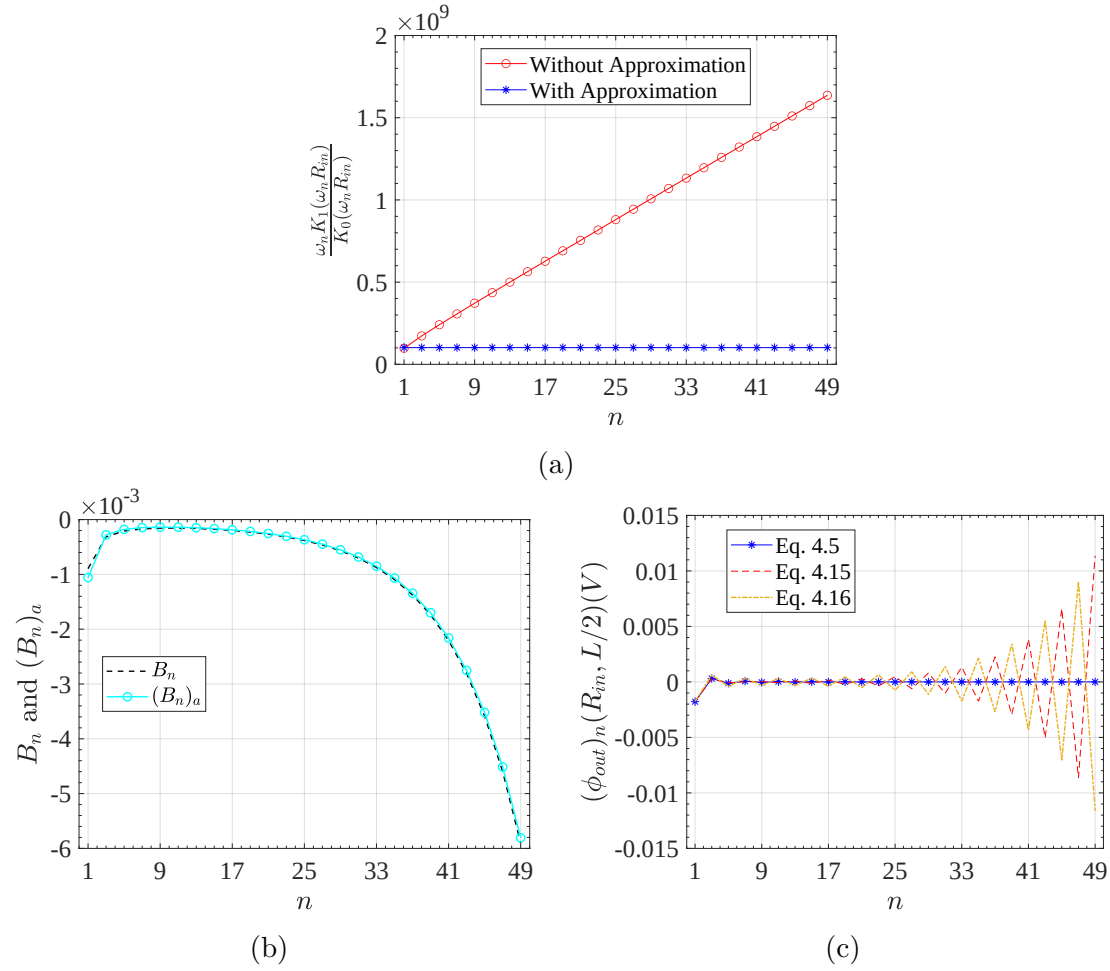

Figure 4.2: (a) $\frac{\omega_n K_1(\omega_n R_{in})}{K_0(\omega_n R_{in})}$ vs. n, compared with its approximation by $\frac{1}{R_{in} M_{L/R_{in}}}$. (b) B_n (Eq. 4.7) and its asymptote $(B_n)_a$ in Eq. 4.12 against n. (c) $(\phi_{out})_n$ at $(R_{in}, L/2)$ for odd values of n calculated using Eq. 4.5, Eq. 4.15 and Eq. 4.16. The plots are generated using $R_{in} = 5\,\text{nm}$, $L = 100\,\text{nm}$, $\epsilon_0 = 8.854 \times 10^{-12}\,\text{F/m}$, $\epsilon_{in} = \epsilon_{out} = 80\epsilon_0\,\text{F/m}$, $\sigma_s = -1.0 \times 10^{-4}\,\text{C/m}^2$, and $\kappa_D = 2.0 \times 10^7\ \text{m}^{-1}$.

We first examine the approximation of $\frac{\omega_n K_1(\omega_n R_{in})}{K_0(\omega_n R_{in})}$ by a constant $\frac{1}{R_{in} M_{L/R_{in}}}$. Figure 4.2a shows that $\frac{\omega_n K_1(\omega_n R_{in})}{K_0(\omega_n R_{in})}$ is almost linearly dependent on n, which deviates significantly from the constant $\frac{1}{R_{in} M_{L/R_{in}}}$ (also shown in Fig. 4.2a). In fact, $\frac{\omega_n K_1(\omega_n R_{in})}{K_0(\omega_n R_{in})}$ tends to infinity as n goes to infinity, which motivates us to investigate the behavior of the coefficient B_n in Eq. 4.7 as n increases. Figure 4.2b plots B_n vs. n for the same nanochannel dimension considered in [1], along with $\sigma_s = -1.0 \times 10^{-4}\,\mathrm{C/m^2}$ and $\kappa_D = 2.0 \times 10^7\ \mathrm{m^{-1}}$. Also plotted is the asymptotic expression of B_n for large n:

$$(B_n)_a = \frac{4\sigma_s \exp\left(\frac{n\pi R_{in}}{L}\right)}{\pi^2(\epsilon_{in} + \epsilon_{out})\sqrt{\frac{n^3}{2R_{in}L}}} \tag{4.12}$$

where the asymptotes of the modified Bessel functions

$$I_0(x), I_1(x) \propto \frac{\exp(x)}{\sqrt{2\pi x}}, \tag{4.13}$$

$$K_0(x), K_1(x) \propto \exp(-x)\sqrt{\frac{\pi}{2x}}, \tag{4.14}$$

for large x have been used. Both Fig. 4.2b and the analytical expression in Eq. 4.12 show that B_n diverges as n goes to infinity (note that the asymptotic approximation in Eq. 4.12 works well even for small n). Therefore, the convergence of $\phi_{out}(r, z)$ in Eq. 4.5 relies critically on the decaying feature of $K_0(\omega_n R_{in})$ and approximating it by a constant on the boundary using Eq. 4.8-4.10 removes this critical feature.

To see this impact, Fig. 4.2c plots $(\phi_{out})_n(R_{in}, L/2)$ against n where $(\phi_{out})_n$ is the n^{th} term of the sum in Eq. 4.5. Only odd values of n are considered since $(\phi_{out})_n(R_{in}, L/2) = 0$ for even values of n due to the symmetry of the system. Compared in the same figure are $(\phi_{out})_n(R_{in}, L/2)$, obtained by using the approximations taken from the following expressions:

$$\phi_{out}(R_{in}, z) = -\sum_{n=1}^{\infty} B_n \sin\left(n\pi\frac{z}{L}\right)\left(\log\frac{n\pi R_{in}}{2L} + \gamma\right), \tag{4.15}$$

$$\phi_{out}(R_{in}, z) \approx M_{L/R_{in}} \sum_{n=1}^{\infty} B_n \sin(\omega_n z). \tag{4.16}$$

Equation 4.15 is found by using the approximation in Eq. 4.8 whereas Eq. 4.16 is found by using Eq. 4.9. Clearly from Fig. 4.2c, the bounded values of $(\phi_{out})_n$ in Eq. 4.5

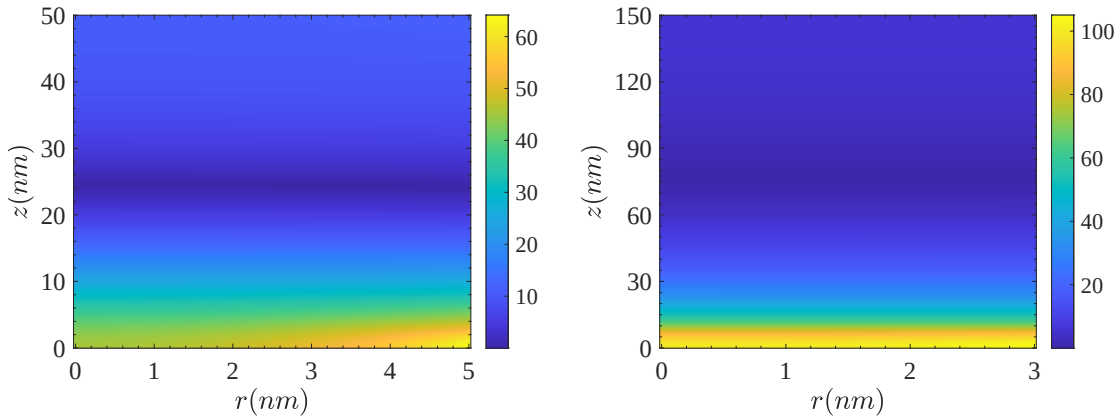

Figure 4.3: Relative error (in %, see Eq. 4.20) as a function of r and z coordinates within a nanotube with length and radius of (a) 100 nm and 5 nm, and (b) 300 nm and 3 nm, respectively.

verify that the divergent values of B_n for large n are compensated by the decay of $K_0(\omega_n R_{in})$ with n, while approximations in Eqs. 4.8-4.9 result in divergent $(\phi_{out})_n$, which is unphysical.

Intuitively, the divergent behavior of $(\phi_{out})_n$ in Fig. 4.2c should not result in a convergent ϕ_{out} and the problematic approximations in Eq. 4.10 should impact the jump boundary condition for the electric displacement. In fact, in Appendix B of [1] an intermediate step is presented before using the continuity condition for the electric potential at $r = R_{in}$ to arrive at Eq. 4.1, namely,

$$\frac{\partial \phi_{out}(R_{in}, z)}{\partial r} = -\frac{\phi_{out}(R_{in}, z)}{R_{in} M_{L/R_{in}}}. \tag{4.17}$$

Under the approximations in Eq. 4.10, $\phi_{out}(R_{in}, z)$ becomes divergent, making this intermediate step unphysical. However, replacing $\phi_{out}(R_{in}, z)$ with $\phi_{in}(R_{in}, z)$ by virtue of continuity accidentally "resolves" this issue, because ϕ_{in} is convergent despite the use of the erroneous approximations in Eq. 4.10. To be more explicit, taking the general solution in Eq. 4.4 and applying the Robin boundary condition Eq. 4.1, the coefficient A_n under this approximation can be obtained, leading to the following

expression for ϕ_{in}:

$$\phi_{in}(r,z) = \sum_{\text{n odd}} \frac{4\sigma_s}{\omega_n L} \frac{R_{in} M_{L/R_{in}} \sin(\omega_n z) I_0\left(\sqrt{\omega_n^2 + \kappa_D^2} r\right)}{\epsilon_{in} R_{in} M_{L/R_{in}} \sqrt{\omega_n^2 + \kappa_D^2} I_1\left(\sqrt{\omega_n^2 + \kappa_D^2} R_{in}\right) + \epsilon_{out} I_0\left(\sqrt{\omega_n^2 + \kappa_D^2} R_{in}\right)} \quad (4.18)$$

The same expression can also be obtained by directly applying the approximations in Eq. 4.10 to Eq. 4.6 in the calculation of A_n. The n^{th} term of this sum, for large n and at $r = R_{in}$, has the following asymptotic behavior:

$$(\phi_{in})_a(R_{in}, z) = \frac{4\sigma_s L}{n^2\pi^2} \sin\left(\frac{n\pi z}{L}\right) \quad (4.19)$$

and, hence, the sum is convergent. This is one reason why Levy et al. used Eq. 4.1 to examine electroneutrality and did not encounter any issues of divergence (see Fig. 5 of [1]).

Another reason why Eq. 4.1 appears to work well in Fig. 5 of [1] is that the calculation of electroneutrality involves the integration of charges in the pore, which smoothens the inaccuracies. Nevertheless, this does not change the fact that there is an intrinsic error associated with using the approximations in Eq. 4.10. To examine the magnitude of the error in the evaluation of ϕ_{in}, the following relative error is computed for ϕ_{in} obtained from the exact solution of Eq. 4.4 and 4.6 ($(\phi_{in})_{exact}$), and ϕ_{in} obtained from Eq. 4.18 ($(\phi_{in})_{approx}$):

$$\text{Relative error (in \%)} = \frac{(\phi_{in})_{exact} - (\phi_{in})_{approx}}{(\phi_{in})_{exact}} \times 100 \quad (4.20)$$

Figure 4.3a shows the relative error when the radius and length of the nanochannel are 5 nm and 100 nm, respectively. The first 99 terms in the sum are used for the calculation of both $(\phi_{in})_{exact}$ and $(\phi_{in})_{approx}$. The error is only plotted for half the length of the pore ($z = 0$ to $L/2$) due to the symmetric nature of the problem. The largest errors are found near the entrance of the nanochannel ($z = 0$). In addition, more than two-thirds of the length of the pore records a relative error above 10%. Considering that the approximations in Eq. 4.10 are based on the condition of $L \gg R_{in}$, Fig. 4.3b shows the relative error for a nanochannel with an even larger aspect

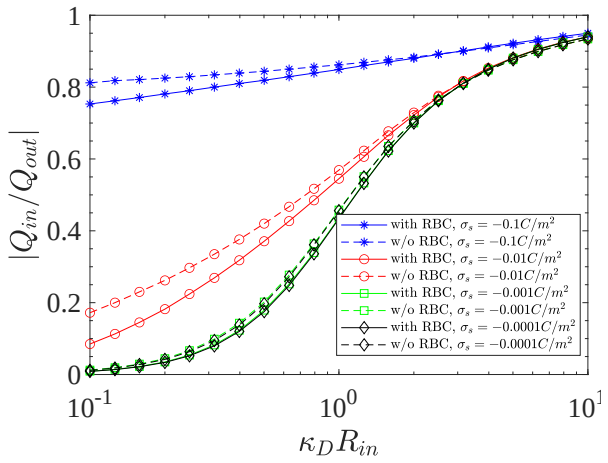

Figure 4.4: Electroneutrality breakdown within the nanochannel system with the Robin boundary condition in Fig. 4.1c and without the Robin boundary condition in Fig. 4.1a. The pore dimensions are: $R_{in} = 5\,\text{nm}$ and $L = 100\,\text{nm}$.

(L to R_{in}) ratio: $R_{in} = 3\,\text{nm}$ and $L = 300\,\text{nm}$. Again, more than two-thirds of the nanochannel exhibits more than 10% error, and over 100% error is observed at the pore entrance for all r. Having a large aspect ratio does not reduce the error, and the poor prediction of ϕ_{in} near the entrance can have a significant effect on the description of transport properties.

In their Appendix B, Levy et al. [1] point out that the Robin boundary condition (Eq. 4.1) is not limited to the linearized DH regime, as long as the channel has a large aspect ratio, $L \gg R_{in}$. This motivates an exploration of the BVP in Fig. 4.1c by employing the PB equation for large to small surface charge densities σ_s, viz., $-1.0 \times 10^{-1}\,\text{C/m}^2$, $-1.0 \times 10^{-2}\,\text{C/m}^2$, $-1.0 \times 10^{-3}\,\text{C/m}^2$, and $-1.0 \times 10^{-4}\,\text{C/m}^2$. Following the analysis in [1], the electroneutrality breakdown $|Q_{in}/Q_{out}|$ is computed for $\kappa_D R_{in}$ in the range of 10^{-1} to 10, and for $R_{in} = 5\,\text{nm}$ and $L = 100\,\text{nm}$, exhibited in Fig. 4.4. Maximum relative error as large as 100% is observed for the case of high surface charge density, $\sigma_s = -0.01\,\text{C/m}^2$, but low bulk concentration, $\kappa_D R_{in} = 0.1$. Here, the DH approximation is no longer valid near the channel wall. This clearly demonstrates that the application of the Robin boundary condition (Eq. 4.1) can, in fact, result in large errors as one moves out of the DH regime.

Last but not least, the Robin boundary condition in Eq. 4.1 causes issues at $r = R_{in}$ and $z = 0$ from a numerical perspective, if one imposes $\phi = 0$ at $z = 0$ for all r, as it is done in its derivation. Clearly, these two conditions can only be met in Eq. 4.1 if $\sigma_s = 0$, which is not the physical case one is usually interested in and which was not assumed in deriving this Robin boundary condition. In other words, for $\sigma_s \neq 0$, a self-consistency issue arises that can cause numerical instabilities or errors. However, the assumption $\phi = 0$ at $z = 0$ is questionable in the first place as it neglects the double-layer overlap at the channel entrance.

To conclude, this chapter points out fundamental issues associated with the approximations employed in Appendix B in [1]. While our discussion remains focused on one specific issue and does not address the other important contributions made in [1], care should be taken when considering using Eq. 4.1 to replace the medium surrounding the nanochannel. From a practical perspective, using this boundary condition may not show a significant impact on the results for the breakdown of electroneutrality (as shown in Fig. 5 of [1]) in the DH regime. However, calculations for the electric potential can result in errors larger than 100% error at the pore entrance, even for nanochannels with very large aspect ratios.

The previous chapter, Chapter 3, offered an in-depth exploration of the trends linked to electroneutrality breakdown within single nanochannels. This chapter sheds light on the challenges associated with the use of the Robin boundary condition, aimed at simplifying these models. In this context, the theoretical framework of single nanochannels was thoroughly investigated. As real-world nanochannel applications often involve the use of multi-channel nanostructures, it becomes vital to extend our analysis to these more complex systems. In this context, the next chapter seeks to delve into the electroneutrality breakdown trends within a periodic array of nanochannels, a representation closer to practical applications.

Chapter 5

Electroneutrality breakdown in periodic arrays of nanochannels

In the preceding chapters, we have examined the occurrence of electroneutrality breakdown within single nanochannels and underscored the necessity of incorporating the dielectric medium into these nanochannel models. Building upon this knowledge, this chapter will explore this phenomenon in a periodic array of nanochannels. Real-world nanostructures often present such configurations [103, 123–126], where the interactions among multiple nanochannels could influence the overall system behavior. Therefore, our objective is to study a model that encompasses a unit cell representation of an infinite periodic array of nanochannels. By doing so, we aim to bridge the gap between fundamental theoretical frameworks and practical nanostructured systems, offering insights that could direct the design and implementation of advanced nanoscale devices.

5.1 Periodic array of nanochannels

Figure 5.1a shows an infinite array of nanochannels arranged in a square packing. These channels are embedded in a dielectric medium and their entrances are connected to reservoirs. A unit cell, highlighted in red, is outlined in the array, serving as a representation of the entire structure. Figure 5.1b shows a unit cell of the periodic array used for COMSOL simulations. Unlike the axisymmetric model of a single

nanochannel explored in Chapter 3, this model cannot be described using cylindrical coordinates due to its non-axisymmetric nature. Within each unit cell, there are four nanochannels, with one positioned at each corner. These channels are characterized by a radius R_{in}, length L, surface charge density σ_s, and permittivity ϵ_{in}. These channels are embedded in the dielectric medium of a length, width, and height of $2R_{out}$, $2R_{out}$, and L, respectively, with a permittivity denoted as ϵ_{out}. Each reservoir is defined by dimensions $2R_{out}$ in length and width, and L_{out} in height. The nanochannels and reservoirs confine a fluid consisting of zero-size ions. To make meaningful comparisons and generalizations, the following normalization scheme is employed for the model.

$$\bar{\phi} = \frac{\tilde{z}e\phi}{k_BT}, \tag{5.1}$$

$$\bar{x} = \frac{x}{R_{in}}, \tag{5.2}$$

$$\bar{y} = \frac{y}{R_{in}}, \tag{5.3}$$

$$\bar{z} = \frac{z}{R_{in}}, \tag{5.4}$$

$$\bar{R}_{out} = \frac{R_{out}}{R_{in}}, \tag{5.5}$$

$$\bar{L} = \frac{L}{R_{in}}, \tag{5.6}$$

$$\bar{L}_{out} = \frac{L_{out}}{R_{in}}, \tag{5.7}$$

$$\eta = \frac{\epsilon_{out}}{\epsilon_{in}}, \tag{5.8}$$

$$\bar{\sigma}_s = \frac{\tilde{z}e\sigma_s R_{in}}{\epsilon_{in}k_BT}, \tag{5.9}$$

$$\bar{\lambda}_D = \frac{\lambda_D}{R_{in}}. \tag{5.10}$$

For a binary symmetric $\tilde{z} : \tilde{z}$ electrolyte, the electric field distribution within the nanochannel and the reservoirs is governed by the normalized classical PB equation,

$$\frac{\partial^2\bar{\phi}_{in}}{\partial\bar{x}^2} + \frac{\partial^2\bar{\phi}_{in}}{\partial\bar{y}^2} + \frac{\partial^2\bar{\phi}_{in}}{\partial\bar{z}^2} = \frac{1}{\bar{\lambda}_D^2}\sinh(\bar{\phi}_{in}), \tag{5.11}$$

where $\bar{\phi}_{in}$ is the normalized electric potential within the nanochannel and the reservoir. The normalized Laplace equation is used to describe the electric potential in

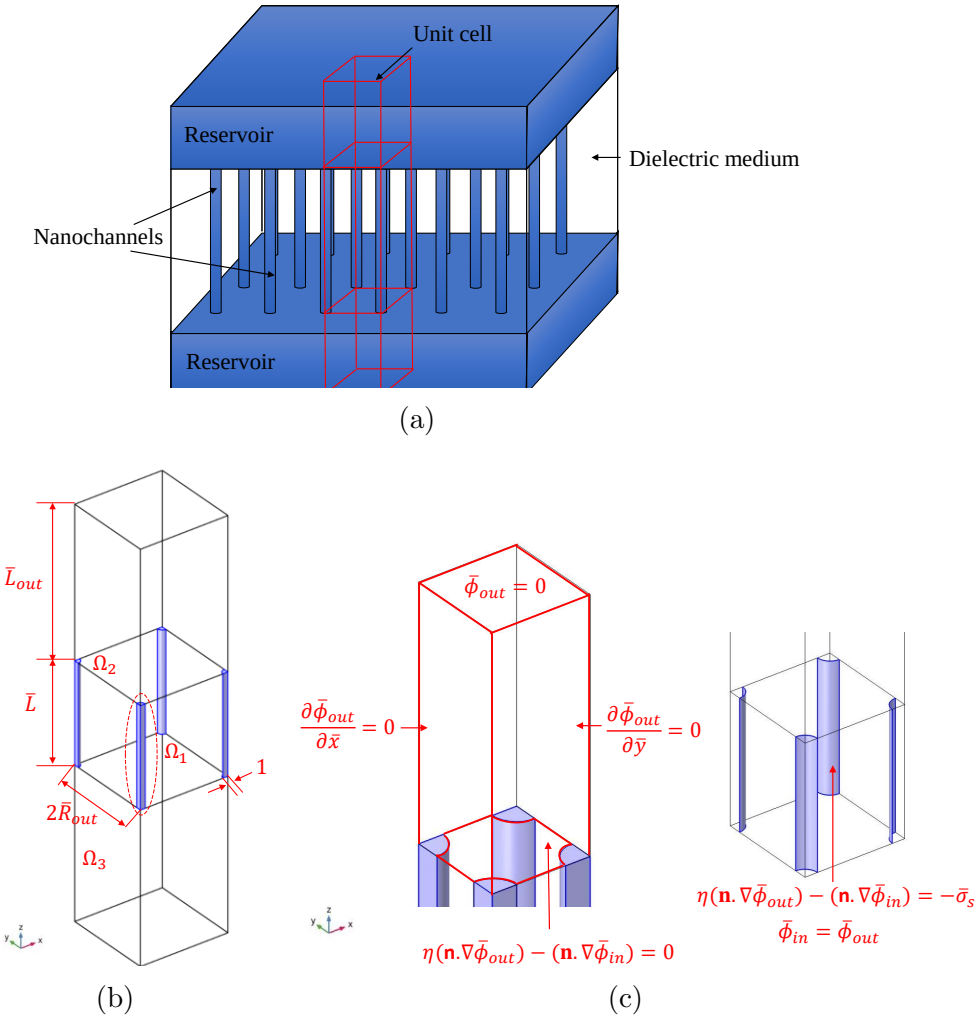

Figure 5.1: (a) Infinite periodic array of square-packed nanochannels embedded in a dielectric medium, with entrances connected to reservoirs. A unit cell of the array, outlined in red, is used to represent the entire array. (b) Orthogonal view of the unit cell with the geometrical parameters. (c) The boundary conditions employed in the COMSOL simulations of the unit cell. Geometry and equations are in the normalized form.

the surrounding dielectric medium,

$$\frac{\partial^2 \bar{\phi}_{out}}{\partial \bar{x}^2} + \frac{\partial^2 \bar{\phi}_{out}}{\partial \bar{y}^2} + \frac{\partial^2 \bar{\phi}_{out}}{\partial \bar{z}^2} = 0, \tag{5.12}$$

where $\bar{\phi}_{out}$ is the normalized electric potential within the dielectric medium.

Figure 5.1c illustrates the BCs enforced upon the model. The symmetry condition is employed on the four lateral boundaries of the unit cell ensuring that it represents the entire periodic array. A uniform surface charge density $\bar{\sigma}_s$ is enforced on the nanochannel-dielectric interfaces,

$$\eta(\mathbf{n} \cdot \nabla \bar{\phi}_{out}) - \mathbf{n} \cdot \nabla \bar{\phi}_{in} = -\bar{\sigma}_s, \tag{5.13}$$

where $\mathbf{n}$ is the surface normal vector pointing outward from the nanochannel towards the dielectric medium. The continuity of the electric potential across the nanochannel-dieletric interfaces is ensured by

$$\bar{\phi}_{in} = \bar{\phi}_{out}. \tag{5.14}$$

The uncharged surfaces separating the dielectric medium and the reservoirs are represented by

$$\eta(\mathbf{n} \cdot \nabla \bar{\phi}_{out}) - \mathbf{n} \cdot \nabla \bar{\phi}_{in} = 0. \tag{5.15}$$

The reservoirs are much longer than the Debye length and, hence, the electric potential is set to zero at its ends.

5.2 Model validation

During our simulations of the system in Fig. 5.1, a similarity was observed with the work of De Souza et al. [89]. These authors conducted simulations for a unit cell that represented a periodic array similar to ours. Given this, their results serve as validation for our model. De Souza et al. [89] used COMSOL Multiphysics for simulations of the unit cell shown in Fig. 5.2a. Their chosen unit cell, detailed in Fig. 5.2b, represents the entire array, with its governing equations and boundary conditions. Despite the

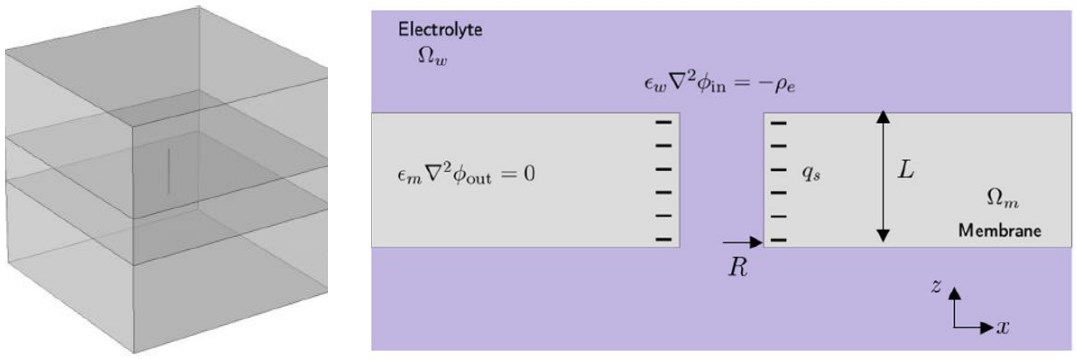

(a) (b)

Figure 5.2: (a) Simulation configuration in COMSOL showing a nanochannel, a dielectric medium, and reservoirs. (b) A cross-section of the unit cell representing the entire periodic array of nanochannels. This cross-section includes the axis of the cylindrical pore, describing the domains and equations utilized in the simulations. Here, R, σ_s, ϵ_{in}, ϵ_{out} correspond to R_{in}, σ_s, ϵ_{in}, ϵ_{out} in this thesis, respectively. Reprinted figure with permission from ref [89]. Copyright 2021 by the American Physical Society.

difference in the choice of the unit cell, the governing equations and boundary conditions employed in both models are the same, ensuring consistency in the approach to simulate electroneutrality breakdown. In De Souza et al. [89], the electroneutrality breakdown curves are presented in dimensionless forms against the center-to-center spacing between channels ($2R_{out}$) normalized by length L as $2R_{out}/L$.

In Fig. 5.3, the COMSOL simulation results are compared for the models depicted in Figs. 5.1 and 5.2 under the conditions of $L = 100\,\text{nm}, R_{in} = 1\,\text{nm}, \sigma_s \to 0, \epsilon_{in} = 80\epsilon_0\,F/m, \epsilon_{out} = 10\epsilon_0\,F/m$. Note that the exact value of σ_s was not mentioned in De Souza et al. [89] when the limit of $\sigma_s \to 0$ was considered. Through multiple tests with various σ_s values, it was deduced that the model in Fig. 5.1 aligns with the observed electroneutrality breakdown when $\sigma_s = 1.0 \times 10^{-5}\,\text{C/m}^2$. Figure 5.3a illustrates the function $|Q_{in}/Q_{out}|$ in terms of $2R_{out}/L$ considering three different bulk ionic concentrations. The curves with star markers are results from our simulation of the unit cell in Fig. 5.1, which overlap the circle markers from De Souza et al. [89] except for an error of approximately 4.5% at $2R_{out}/L = 0.02$ and $c_0 = 0.01\,\text{mM}$.

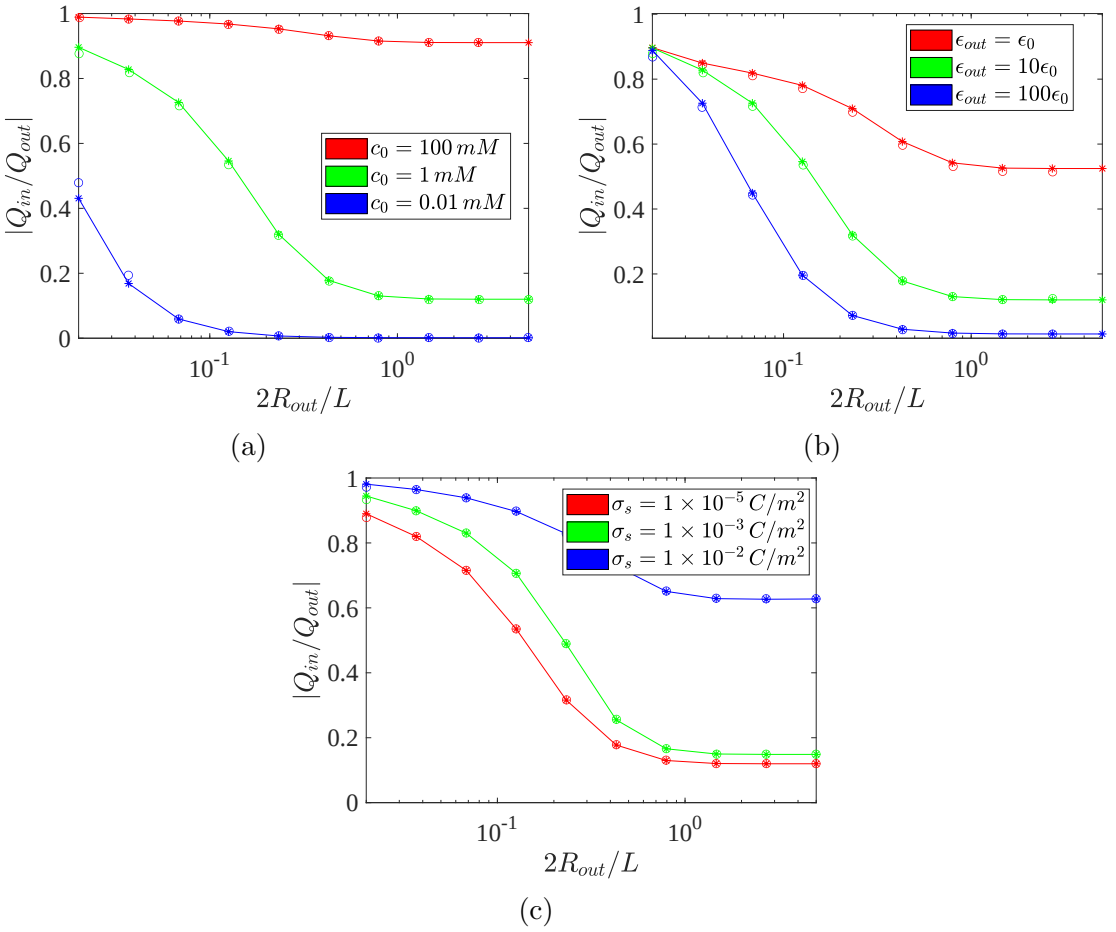

Figure 5.3: $|Q_{in}/Q_{out}|$ vs. $2R_{out}/L$ for (a) $\epsilon_{out} = 10\epsilon_0$, $\sigma_s = 1.0 \times 10^{-5}\,\mathrm{C/m^2}$ and three different c_0 (b) $c_0 = 1\,\mathrm{mM}$, $\sigma_s = 1.0 \times 10^{-5}\,\mathrm{C/m^2}$ and varying ϵ_{out}, and (c) $\epsilon_{out} = 10\epsilon_0\,\mathrm{F/m}$, $c_0 = 1\,\mathrm{mM}$, and three different σ_s. The circle markers are the COMSOL simulation results by De Souza et al. [89] for their model in Fig. 5.2 while the star markers are our COMSOL simulation results for our model in Fig. 5.1. The channel dimensions are $L = 100\,\mathrm{nm}$ and $R_{in} = 1\,\mathrm{nm}$ with $\epsilon_{in} = 80\epsilon_0\,\mathrm{F/m}$.

Figure 5.3b shows $|Q_{in}/Q_{out}|$ with respect to $2R_{out}/L$ for three different permittivities of the dielectric medium. Again, the curves with star markers align well with the circle markers, with the exception of an error of about 1%, observable at some points on the blue and red curves. Finally, in Fig. 5.3b, $|Q_{in}/Q_{out}|$ is depicted as a function of $2R_{out}/L$, now exploring three surface charge densities. In this case, the star marker curves align extremely well with the circle markers. The remarkable agreement with the previous work [89], marked by only minor deviations, underscores the validation of our modeling approach employed in COMSOL Multiphysics.

The underlying causes of the electroneutrality breakdown, as depicted in these figures, are already discussed in Section 3.4. Additionally, it is observed in Fig. 5.3 that the system tends towards electroneutrality as the channels are brought closer together in the array by decreasing $2R_{out}/L$. This trend is attributed to the interaction between the nanochannels in the array, referred to as the "coupling of nanochannels" in this work. Such coupling leads to an increase in the magnitude of the electric potential inside the channels, and consequently an increase in the concentration of counterions within the channels. Higher concentration of counterions leads to more screening of the surface charge on the channel, thereby driving the system towards electroneutrality. Drawing from the analysis of single nanochannels in Chapter 3, a detailed study is undertaken to study the electroneutrality breakdown across an infinite periodic array of nanochannels, considering a range of parameters listed in Table 3.2. In contrast, De Souza et al. [89] focused their findings on distinct parameter values such as c_0, ϵ_{out}, and σ_s.

5.3 Comparison between a periodic array of nanochannels and a single nanochannel

Phase diagrams are generated as a result of the parametric study for an infinite periodic array of nanochannels in a similar fashion as discussed in Sec. 3.4. A comparative analysis is performed between these newly obtained phase diagrams and the phase di-

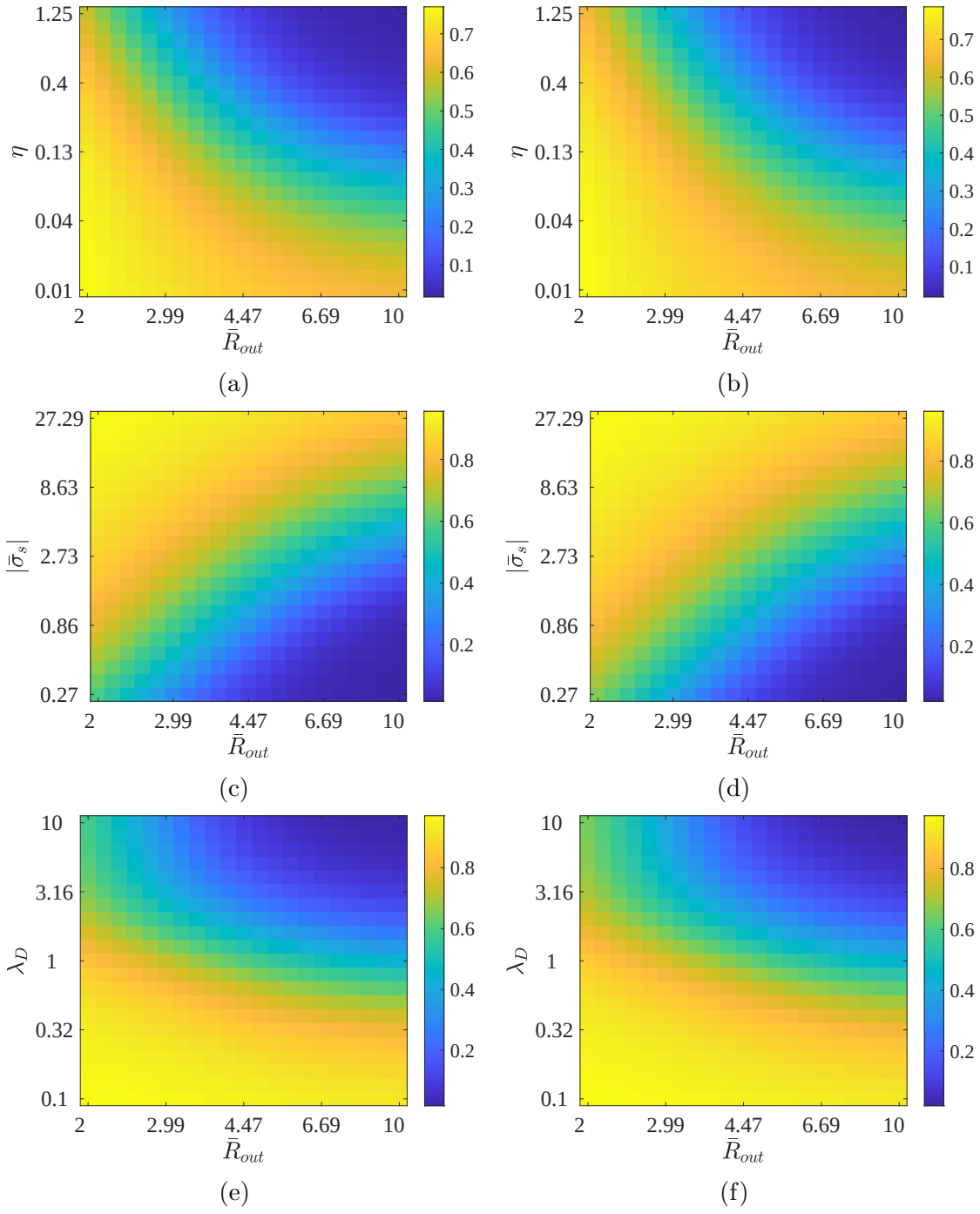

Figure 5.4: Log-log plots of $|Q_{in}/Q_{out}|$ for an infinite periodic array of nanochannels (left panel) and a single nanochannel (right panel) as a function of (a) & (b) η and $\bar{R}_{out}$, (c) & (d) $|\bar{\sigma}_s|$ and $\bar{R}_{out}$, and (e) & (f) $\bar{\lambda}_D$ and $\bar{R}_{out}$. The other fixed parameters for each phase diagram are listed in Table 3.1.

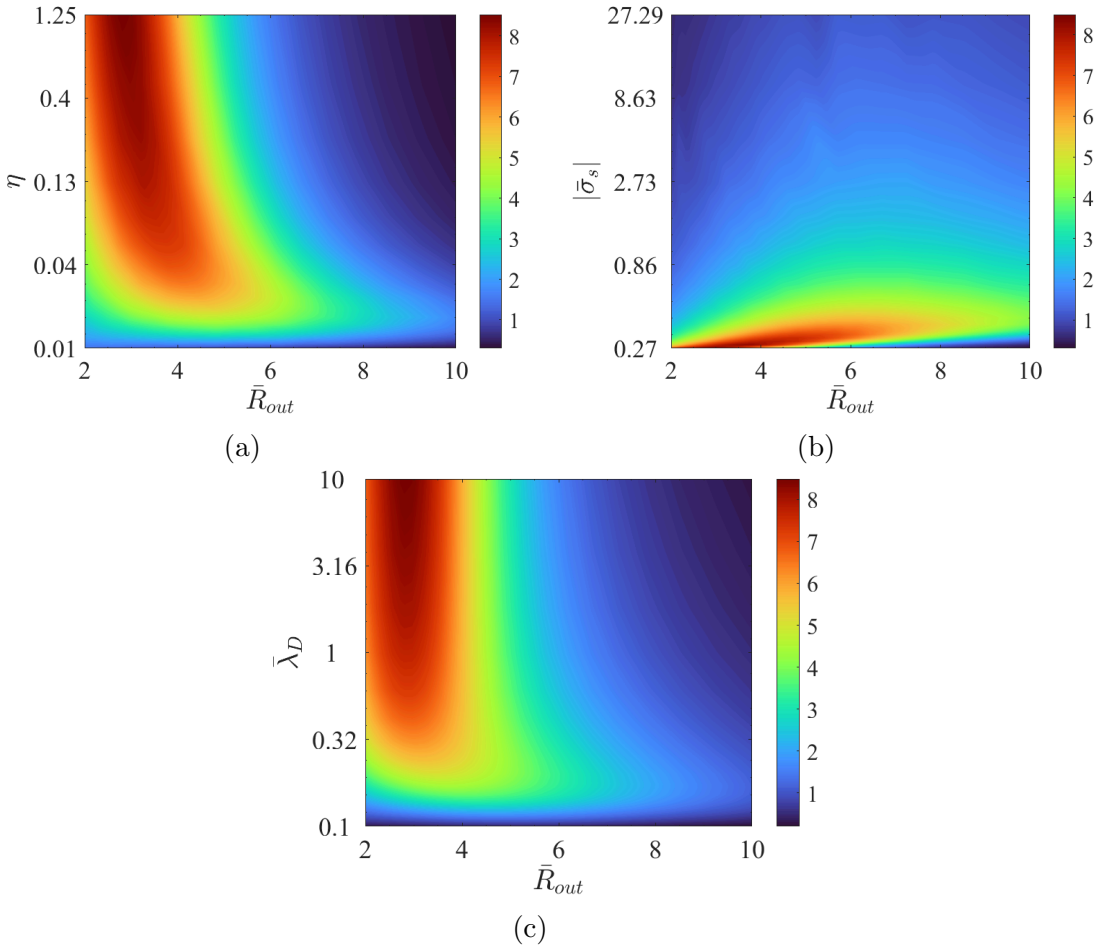

Figure 5.5: Log-log plots of difference (in %) in $|Q_{in}/Q_{out}|$ between an infinite periodic array of nanochannels and a single nanochannel as a function of (a) η and $\bar{R}_{out}$, (b) $|\bar{\sigma}_s|$ and $\bar{R}_{out}$, and (c) $\bar{\lambda}_D$ and $\bar{R}_{out}$. The other fixed parameters for each plot are listed in Table 3.1.

Table 5.1: Comparison of electric field leakages, q_{ex}^1 and q_{ex}^2, for both the nanochannel array and the single channel models. Values are provided for specific parameters: $\eta = 1.25$, $|\bar{\sigma}_s| = 0.27$, $\bar{\lambda}_D = 10$, and both $\bar{R}_{out} = 2$ and $\bar{R}_{out} = 10$.

Nanochannel array				Single channel			
$\bar{R}_{out} = 2$		$\bar{R}_{out} = 10$		$\bar{R}_{out} = 2$		$\bar{R}_{out} = 10$	
q_{ex}^1	q_{ex}^2	q_{ex}^1	q_{ex}^2	q_{ex}^1	q_{ex}^2	q_{ex}^1	q_{ex}^2
0.15	0.57	1.63	53.86	0.13	0.37	1.46	45.46

agrams of a single nanochannel in Fig. 5.4[1]. Upon close inspection, subtle differences are noted in the corresponding phase diagrams. To better understand these discrepancies, the difference in $|Q_{in}/Q_{out}|$ (absolute difference reported in % for more clarity) between the diagrams of the nanochannel array and the single channel is graphically represented in Fig. 5.5 using contour plots. Figure 5.5a captures the variation in electroneutrality breakdown with respect to η and $\bar{R}_{out}$. Similarly, Fig. 5.5b showcases the differences as a function of $|\bar{\sigma}_s|$ and $\bar{R}_{out}$, while Fig. 5.5c shows the differences influenced by $\bar{\lambda}_D$ and $\bar{R}_{out}$. Collectively, it becomes evident that the disparities can be as significant as 8% for $\bar{R}_{out} = 2$, while being as subtle as 1% for $\bar{R}_{out} = 10$. This calls for an exploration of the electroneutrality trends for $\bar{R}_{out}$ being 2 and 10 for both the nanochannel array and the single channel.

Figure 5.6a and Fig. 5.6b show $|Q_{in}/Q_{out}|$ vs. η for $\bar{R}_{out} = 2$ and $\bar{R}_{out} = 10$, respectively, for both nanochannel models. Similarly, Figs. 5.6c and 5.6d show the effect of $|\bar{\sigma}_s|$ on $|Q_{in}/Q_{out}|$ while Figs. 5.6e and 5.6f highlight the ramifications of varying $\bar{\lambda}_D$. Two primary observations emerged from this comparison. First, a more pronounced electroneutrality breakdown was observed for the nanochannel array compared to the single channel. Second, while the breakdown curves for both models closely aligned for $\bar{R}_{out} = 10$, a divergence was noted for $\bar{R}_{out} = 2$.

The models were further investigated for the parameter set exhibiting the most

[1]No-flux boundary conditions for the electric field are imposed on the lateral surfaces for both the unit cell of the array and the single nanochannel.

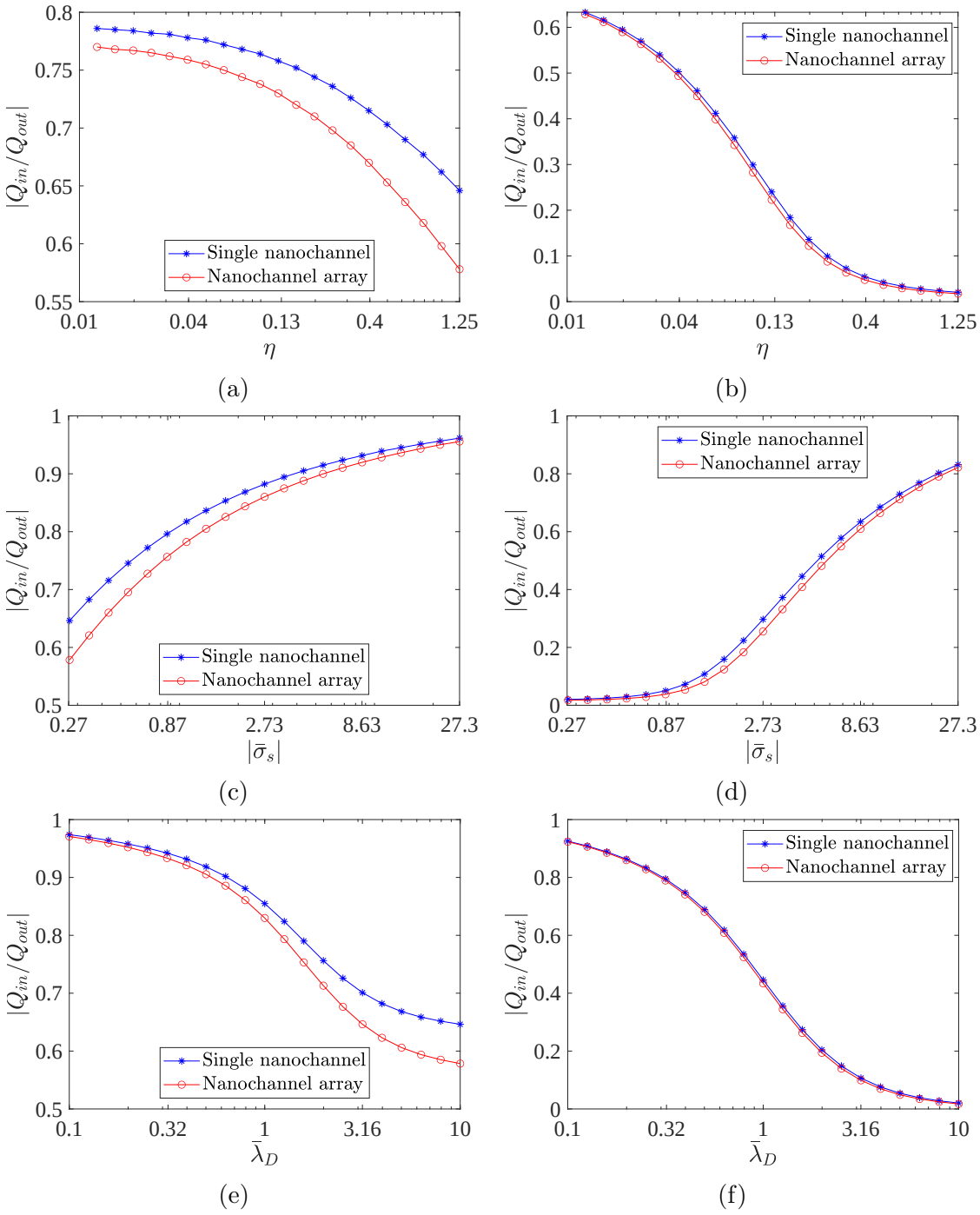

Figure 5.6: $|Q_{in}/Q_{out}|$ against (a) & (b) η, (c) & (d) $|\bar{\sigma}_s|$, and (e) & (f) $\bar{\lambda}_D$ for $\bar{R}_{out} = 2$ (left panel) and $\bar{R}_{out} = 10$ (right panel) for a single nanochannel and a nanochannel array. The other fixed parameters for each plot are listed in Table 3.1.

pronounced difference in $|Q_{in}/Q_{out}|$, specifically $\eta = 1.25$, $|\bar{\sigma}_s| = 0.27$, $\bar{\lambda}_D = 10$, and $\bar{R}_{out} = 2$. It is also compared with the models with $\bar{R}_{out} = 10$ keeping all the other parameters fixed. Leakages q^1_{ex} and q^2_{ex} associated with these parameters were recorded and subsequently compared in Table 5.1. Elevated levels of leakages were observed in the nanochannel array, thereby inducing a more prominent breakdown in electroneutrality compared to the single channel. The electric potential and ion concentration are studied along certain coordinates within the nanochannel to further investigate the breakdown of electroneutrality. In Fig. 5.7a, a quarter section of the nanochannel array is highlighted by dashed black lines on the $x-y$ plane with $\bar{z} = \bar{L}/2$. In this figure, coordinate x_1 is defined along the horizontal edge, and coordinate x_2 is defined along the diagonal, forming an angle of 45° with the horizontal. Re-examining Fig. 5.1, it is clear that both x_1 and x_2 serve as a line of symmetry. As a result, the electric field at any point on x_1 is entirely along x_1 and does not have a component perpendicular to x_1. The same applies to x_2. Such a feature is similar to the electric field at any points on the radial axis (r, depicted in Fig. 5.7b) in the single nanochannel model where, due to axisymmetry, the electric field is entirely along the r axis. This similarity in the behavior of the electric field along coordinates x_1, x_2, and r facilitates the comparison between the array and the single channel models. Figures depicting the electric potential $\bar{\phi}_{in}$ and ion concentration c were generated along these lines and presented in Figs. 5.8a and 5.8c for $\bar{R}_{out} = 2$, and Figs. 5.8b and 5.8d for $\bar{R}_{out} = 10$. Lower magnitudes of $\bar{\phi}_{in}$ were noted for the nanochannel array along x_1 and x_2 in comparison to the single channel along r, resulting in a reduced concentration of charges. This further reinforced the observation that the nanochannel array displayed a stronger inclination towards electroneutrality breakdown.

The electric field E is calculated along x_1 and x_2 in the array, and r in the single channel and normalized to $\bar{E}$ in Fig. 5.8e for $\bar{R}_{out} = 2$ and Fig. 5.8f for $\bar{R}_{out} = 10$.

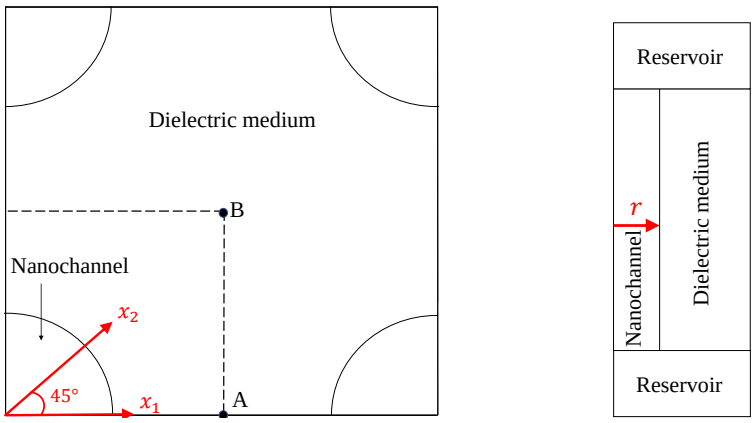

Figure 5.7: (a) Coordinates x_1 and x_2 originating from the center of the nanochannel extending along the edge and the diagonal, respectively, on the mid-cross section ($\bar{z} = \bar{L}/2$) of the quarter section of the array. (b) Coordinate r originating from the center and extending along the radius of the mid-cross section ($\bar{z} = \bar{L}/2$) of the single nanochannel.

The normalized electric field, $\bar{E}$, is defined by

$$\bar{E} = \frac{\tilde{z} e R_{in} (\mathbf{E} \cdot \mathbf{n})}{k_B T}. \tag{5.16}$$

where $\mathbf{n}$ is the direction of the coordinates x_1, x_2 and r. For both $\bar{R}_{out} = 2$ and $\bar{R}_{out} = 10$, $\bar{E}$ approaches zero along each specified direction (x_1, x_2 and r), though at different distances. For the array shown in Fig. 5.7a, the convergence of $\bar{E}$ to zero was noted at the intersections of x_1 and x_2 with the dashed black lines, at points A and B. For the single nanochannel shown in Fig. 5.7b, $\bar{E} = 0$ at the outer surface of the dielectric medium due to the BC (Eq. 3.37). Since non-zero electric field in the dielectric medium is a major contribution to leakage and hence electroneutrality breakdown, two hypothetical single channel models, labeled as 1 and 2, were proposed and depicted in Fig. 5.9. Models 1 and 2 share the same physical parameters as the array except the radii of their dielectric media. Specifically, the radius of the dielectric medium of model 1 is $\bar{R}_{out}$, while that of model 2 is $\sqrt{2}\bar{R}_{out}$. The BCs on the outer surface of their dielectric media, respectively, align with the electric field conditions at points A and B of the nanochannel array model. Given the three-

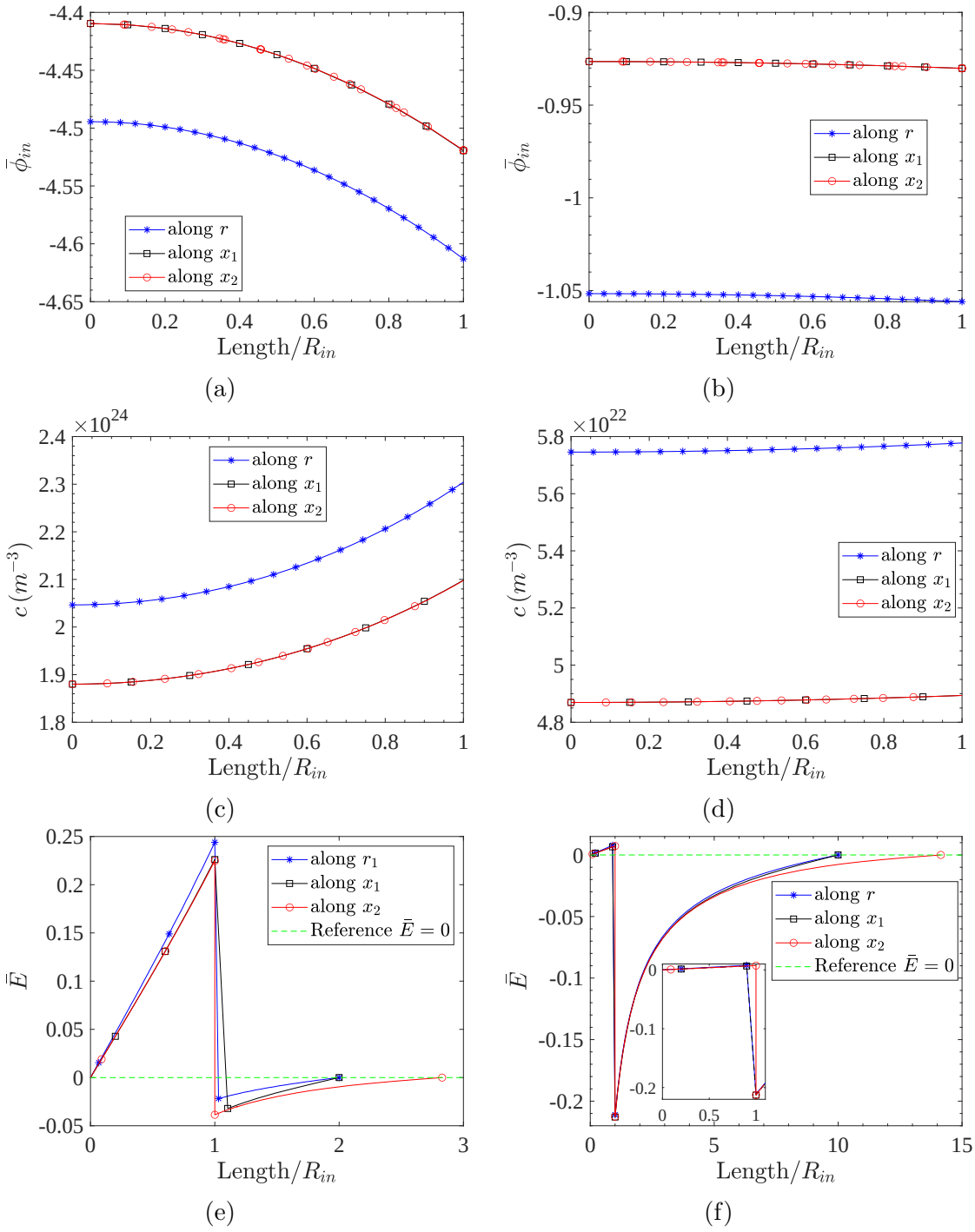

Figure 5.8: (a) & (b) $\bar{\phi}_{in}$, (c) & (d) c, and (e) & (f) $\bar{E}$ plotted along the coordinates, shown in Fig. 5.7a and Fig. 5.7b, of the nanochannel array and the single channel, respectively, normalized by R_{in}. The left panel corresponds to $\bar{R}_{out} = 2$ while the right panel is for $\bar{R}_{out} = 10$. The other parameters are $\eta = 1.25$, $|\bar{\sigma}_s| = 0.27$, $\bar{\lambda}_D = 10$. $\bar{E}$ is plotted in the direction of these coordinates for the entire quarter section highlighted by the dashed black lines in Fig. 5.7a whereas $\bar{\phi}_{in}$ and c are plotted within the nanochannel only.

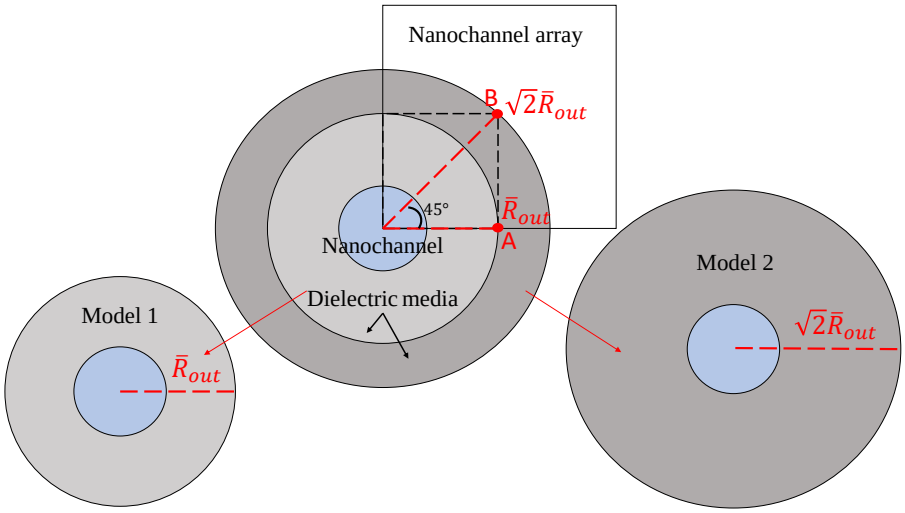

Figure 5.9: The hypothetical single nanochannel models, labeled 1 and 2, whose boundary conditions on the outer surface of the dielectric medium match the condition of the electric field at points A and B of the nanochannel array model, respectively. The radius of the dielectric media of model 1 is $\bar{R}_{out}$ and of model 2 is $\sqrt{2}\bar{R}_{out}$.

dimensional geometry of the array, the volume of the dielectric medium encompassing a nanochannel is situated between the volumes of the dielectric media in models 1 and 2. Consequently, this implies that the electric field leakage values of the nanochannel array should also be intermediate to those of the two models. This is confirmed when the leakages within the array in Table 5.1 are compared to the leakages within the single channels for $\bar{R}_{out}$ equal to 2, $2\sqrt{2}$, 10, and $10\sqrt{2}$, listed in Table 5.2. The array registers higher leakages than the single channel for $\bar{R}_{out}$ equal to 2 and 10 but lower for $\bar{R}_{out}$ equal to $2\sqrt{2}$, and $10\sqrt{2}$.

In Fig. 5.6, disparities in the Q_{in}/Q_{out} curves for $\bar{R}_{out} = 2$ are more pronounced than those for $\bar{R}_{out} = 10$. According to Table 5.1, for $\bar{R}_{out} = 2$, q_{ex}^2 in the array surpasses that of the single channel by a significant 54%. This pronounced difference is noted for only 36.4% increase in the volume of the dielectric medium in the array than the single channel. On the other hand, for $\bar{R}_{out} = 10$, despite a large 3114.2% increase in the volume of the array compared to the single channel, q_{ex}^2 surpasses the single channel by a relatively modest 18.5%. Note that these percentage differences were calculated with q_{ex}^2 of the single channel used as the reference. In Sec. 3.4, it was

Table 5.2: Electric field leakages, q_{ex}^1 and q_{ex}^2, for a single nanochannel with $\bar{R}_{out}$ equal to 2, $2\sqrt{2}$, 10, and $10\sqrt{2}$. The other parameters are $\eta = 1.25$, $|\bar{\sigma}_s| = 0.27$, $\bar{\lambda}_D = 10$, and $\bar{L} = 20$.

$\bar{R}_{out} = 2$		$\bar{R}_{out} = 2\sqrt{2}$		$\bar{R}_{out} = 10$		$\bar{R}_{out} = 10\sqrt{2}$	
q_{ex}^1	q_{ex}^2	q_{ex}^1	q_{ex}^2	q_{ex}^1	q_{ex}^2	q_{ex}^1	q_{ex}^2
0.13	0.37	0.17	0.98	1.46	45.46	1.96	70.37

discussed that the electric field leakage through the channel wall is confined by the dielectric medium. $\bar{R}_{out} = 2$ provides stronger confinement and as a result, a small increase in dielectric volume (from single channel to array) can cause a large relaxation of the confinement leading to significantly increased leakage. This emphasizes the critical role of the dielectric medium in governing the electroneutrality breakdown.

5.4 Effect of temperature

The interesting results found for single nanochannels at $T = 353\,\mathrm{K}$ in Sec. 3.6 have sparked an investigation into the behavior of nanochannel arrays of square packing, under similar conditions. De Souza et al. [89] concluded that the array with square packing is a good approximation for a variety of channel arrangements by comparing it with the nanochannel array with a hexagonal arrangement. Figure 5.10 shows one such arrangement of a nanochannel array with hexagonal packing where a unit cell representing the entire array is outlined in red. The nanochannel arrays with square and hexagonal arrangements are investigated to analyze the electroneutrality breakdown within interacting nanochannels with a fixed $\bar{R}_{out}$ of 2, while varying η, $|\bar{\sigma}_s|$, and $\bar{\lambda}_D$, at an elevated temperature of $T = 353\,\mathrm{K}$. These results are also compared to that of the single channel for a better understanding of the trends.

The impact of η on $|Q_{in}/Q_{out}|$ is illustrated in Figs. 5.11a and 5.11b at $T = 353\,K$ and $T = 300\,K$, respectively. Figures 5.11c and 5.11d depict the influence of $|\bar{\sigma}_s|$ on $|Q_{in}/Q_{out}|$ at $T = 353\,K$ and $T = 300\,K$, respectively. Figures 5.11e and 5.11f highlight the effect of $\bar{\lambda}_D$ on $|Q_{in}/Q_{out}|$ at $T = 353\,K$ and $T = 300\,K$, respectively.

Table 5.3: Electric field leakages, q_{ex}^1 and q_{ex}^2, for a single nanochannel with $\bar{R}_{in} = 1$ and $\bar{L} = 20$ at $T = 353\,\mathrm{K}$ and $T = 300\,\mathrm{K}$. The other parameters are $\eta = 0.13$, $|\bar{\sigma}_s| = 0.27$, $\bar{\lambda}_D = 10$, and $\bar{R}_{out} = 2$.

$T = 353\,\mathrm{K}$				$T = 300\,\mathrm{K}$			
Square packing		Hexagonal packing		Square packing		Hexagonal packing	
q_{ex}^1	q_{ex}^2	q_{ex}^1	q_{ex}^2	q_{ex}^1	q_{ex}^2	q_{ex}^1	q_{ex}^2
0.16	0.92	0.15	0.53	0.15	0.57	0.13	0.44

The leakages at both temperature settings are quantified for the parameter set of $\eta = 0.13$, $|\bar{\sigma}_s| = 0.27$, $\bar{\lambda}_D = 10$, and $\bar{R}_{out} = 2$. Note that, as established in Sec. 5.3, the electroneutrality breakdown trends of the nanochannel array with square packing align very well with that of the single channel for $\bar{R}_{out} = 10$, thus the effect of temperature is studied for $\bar{R}_{out} = 2$ only. The electric field leakages q_{ex}^1 and q_{ex}^2 are computed for these parameters for the nanochannel arrays with both square and hexagonal arrangements and compared in Table 5.3. Two observations can be made from the leakages as well as the figures in Fig. 5.11. Firstly, the nanochannel arrays exhibit higher leakages at the elevated temperature resulting in more pronounced electroneutrality breakdown. This supports the discussion in Sec. 3.6 where the single channel is shown to depict a similar trend of electroneutrality breakdown at the two temperatures. Secondly, the square-packed nanochannel array exhibits higher

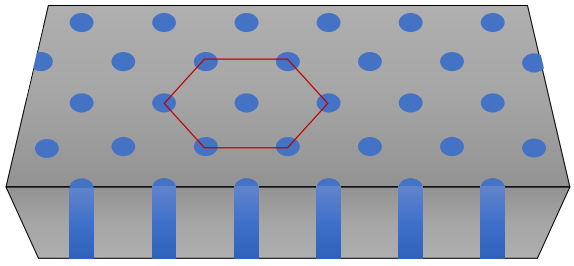

Figure 5.10: A periodic nanochannel array with hexagonal packing. A unit cell employed in the COMSOL simulation, representing the entire array, is indicated with a red outline. The reservoirs connected to the channel entrances included in the COMSOL model are not indicated in the figure.

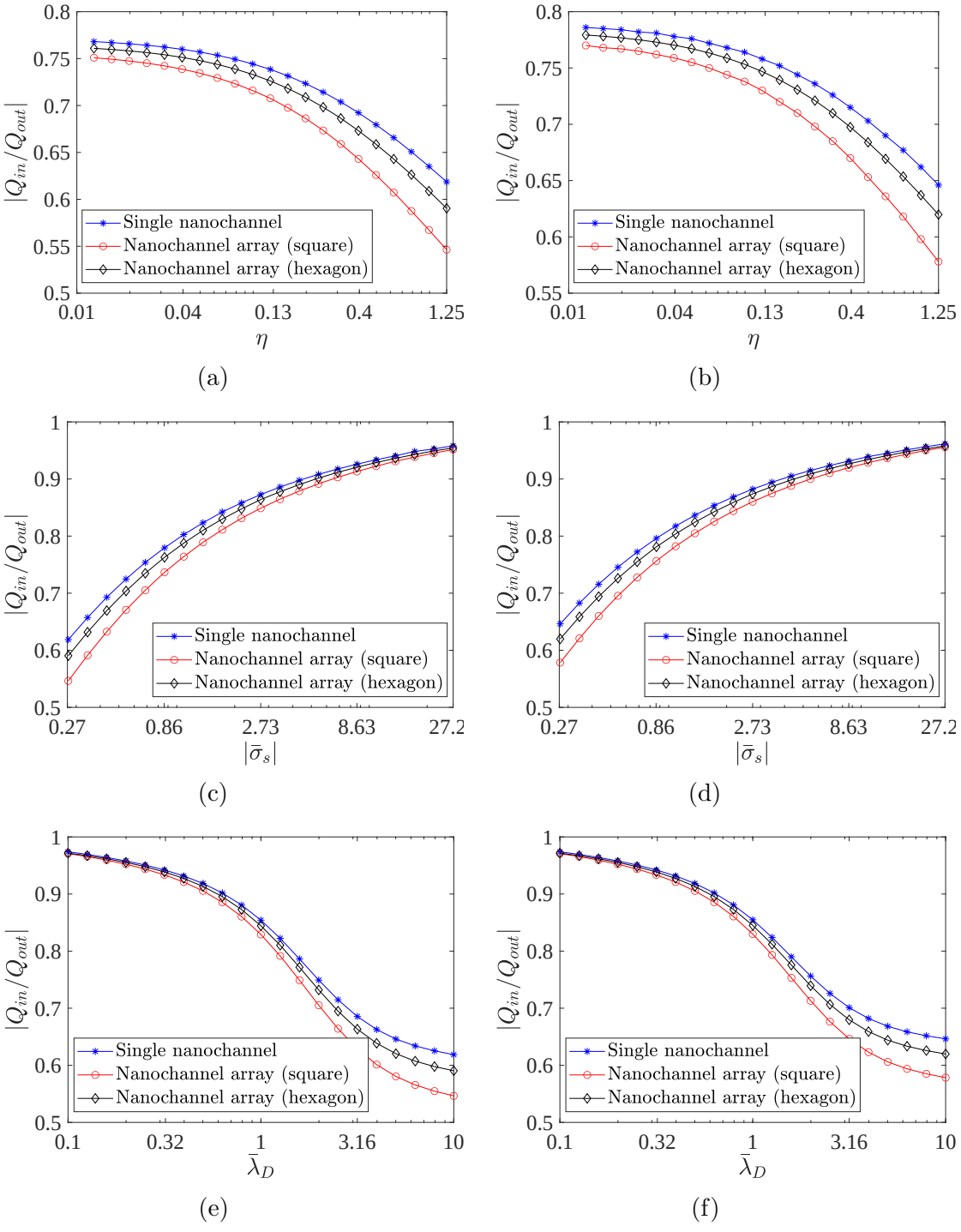

Figure 5.11: $|Q_{in}/Q_{out}|$ against (a) & (b) η, (c) & (d) $|\bar{\sigma}_s|$, and (e) & (f) $\bar{\lambda}_D$ for a single nanochannel and a nanochannel array with square and hexagonal packing at $T = 353\,\mathrm{K}$ (left panel) and $T = 300\,\mathrm{K}$ (right panel). The other parameters are listed in Table. 3.1.

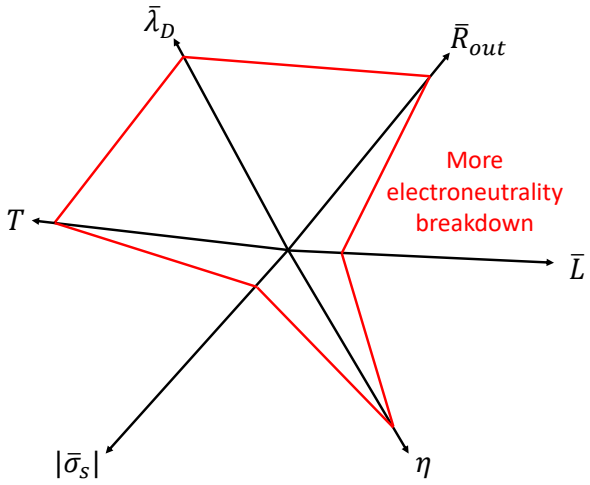

Figure 5.12: Diagram showing a multi-dimensional visualization of electroneutrality breakdown governed by six key parameters of our study. For each axis, the location of the intersection of the polygon with the axis indicates the direction (increasing or decreasing magnitude of the respective parameter) in which electroneutrality breakdown increases as all other parameters are held constant.

leakages when compared to the hexagonal-packed array for both temperature settings, listed in Table 5.3. This can be explained by the fact that an array with square packing has a coordination number (number of surrounding nanochannels) of 4 while it is 6 for a hexagonal arrangement. A higher coordination number implies more coupling among the channels, thereby directing the system toward electroneutrality, depicted in Fig. 5.11. Thus, the role of channel coupling is highlighted through this observation. However, further investigation at various temperatures is necessary before any definite conclusions can be drawn.

A visual summary of the trends for increase in electroneutrality breakdown caused by each physical parameter, namely $\bar{L}$, $\bar{R}_{out}$, η, $|\bar{\sigma}_s|$, $\bar{\lambda}_D$, and T, is illustrated by a multi-dimensional "surface" in Fig. 5.12. Note that all the parameters are normalized except T. The intersection of the red polygon with each axis indicates the contribution of the specific parameter towards an increase in electroneutrality breakdown keeping the other parameters fixed. For example, when T is increased while all the other parameters remain the same, electroneutrality breakdown is more pronounced in the

system. Similarly, increasing $\bar{\lambda}_D$ (or $\bar{R}_{out}$ or η), while keeping all other parameters fixed, increases electroneutrality breakdown. For $\bar{L}$ and $|\bar{\sigma}_s|$, the trend is the opposite, i.e. decreasing their magnitudes enhances electroneutrality breakdown.

Chapter 6

Conclusion and future work

In this final chapter, the main findings of the work are summarised and discussed, and suggestions are presented for future studies. Chapter 3 establishes a comprehensive investigation of electroneutrality breakdown within single-digit nanochannels (SDNs) utilizing COMSOL Multiphysics. This exploration is initiated with an analytical and numerical examination of an infinite, single nanochannel, which serves as a validation for the numerical model. The one-dimensional model is followed by the modeling of a finite, single nanochannel in an $r-z$ plane, a key step in understanding the intricacies of electroneutrality within the nanochannel. The electric field leakages through the channel wall and entrances are revealed as contributing factors to electroneutrality breakdown. An array of physical parameters is examined for their influence on electroneutrality breakdown, leading to the creation of a set of phase diagrams. These diagrams depict $|Q_{in}/Q_{out}|$ as a function of combinations of two physical parameters, such as $\bar{L}$ and $\bar{R}_{out}$, η and $\bar{R}_{out}$, and $|\bar{\sigma}_s|$ and $\bar{\lambda}_D$. It is demonstrated that a system comprising a short nanochannel, filled with a dilute electrolytic solution and separated by a weakly charged interface from a thick dielectric medium with high permittivity, tends towards electroneutrality breakdown. The influence of steric effects on electroneutrality breakdown is analyzed by considering finite-size ions. Results suggest that while steric effects may not significantly impact the deviation from electroneutrality, they might have an influence on breakdown scenarios that fall outside

the applicability of continuum models, such as in sub-nanometer nanochannels. Acknowledging the potential influence of temperature on electroneutrality breakdown, the model is analyzed under two distinct temperature conditions, viz., $T = 300K$ and $T = 353K$. It is observed that an increase in temperature, which translates to higher kinetic energy for the ions of the electrolytes, can promote the deviation from electroneutrality driven by entropy.

Chapter 4 emphasizes the vital role of incorporating the dielectric medium into the model. In their work, Levy et al. [1] proposed a Robin boundary condition at the surface of the nanochannel, which offers an opportunity to eliminate the need to compute the electric field in the surrounding medium. Through a detailed analysis, the fundamental issues associated with the approximations employed in the derivation of the proposed boundary condition are pointed out. These approximations can give relative errors as large as 100% in assessing the electric potential and the charge distribution within the single nanochannel. The implications of these findings are profound and considerable caution is required when deciding to utilize a boundary condition to represent the medium enveloping the nanochannel. Inaccurate representations can skew our understanding of ion transport within nanochannels, leading to potentially erroneous predictions and conclusions.

Chapter 5 represents a significant stride towards translating the theoretical framework to practical nanostructured systems, extrapolating from the insights gained in earlier chapters. The nanochannel array model employed in our study is validated by its alignment with the $|Q_{in}/Q_{out}|$ curves presented by De Souza et al. [89]. Findings suggest that the interaction between nanochannels becomes apparent when the inter-channel distance is on par with the radius of the channel. As the channels are progressively brought closer, a trend toward electroneutrality becomes evident. Our investigation branches into a comparative analysis between the electroneutrality breakdown trends observed for the nanochannel array and the single channel models. It is found that even though the interaction between the nanochannels leads the

array towards electroneutrality, the propensity for breakdown is still higher in the array when compared to a single channel. Analysis of the electric potential, the ion concentration, and the electric field leakages showed that the pronounced breakdown observed in the array can be ascribed to greater electric field leakages. This increased leakage is facilitated by the increased volume of the dielectric medium of the array when compared to a single channel. Notably, a slight volume augmentation highly affects the electric field leakages in case of lower $\bar{R}_{out}$ in an array due to restriction in leakage caused by a thin dielectric medium. However, with less restricted leakage for higher $\bar{R}_{out}$, an increase in volume does not significantly increase the leakage. This results in the disparity between $|Q_{in}/Q_{out}|$ of the nanochannel array and the single channel at $\bar{R}_{out} = 2$, while at $\bar{R}_{out} = 10$, the curves align very well. This suggests that a single channel can approximate a nanochannel array when the influence of channel coupling diminishes. At an elevated temperature of $T = 353K$, the nanochannel array displays a distinct inclination towards breakdown for both arrangements, namely hexagonal and square. The hexagonal arrangement exhibited a reduced tendency towards electroneutrality breakdown, attributed to its increased coupling from being surrounded by more nanochannels compared to the square arrangement. However, similar breakdown patterns were observed for both configurations at $T = 300\,K$ and $T = 353K$.

For future endeavors, several avenues of investigation emerge from this study. One such area involves the scrutiny of electroneutrality breakdown at elevated temperatures, which can provide a more comprehensive understanding of the behavior of both single nanochannels and nanochannel arrays under higher thermal conditions. Another interesting exploration could be to model the surrounding medium as a semiconductor. Semiconductors, with their unique and controllable electrical properties imparted through techniques such as doping or voltage application, offer a realm of possibility for diverse applications. Further inquiry may also extend to studying both single and array systems under conditions of flow through the channels, enabling the

analysis of electroneutrality breakdown's influence on conductivity and capacitance [89]. Lastly, implementing Molecular Dynamics simulations could provide a more nuanced and accurate representation of the model's physics. This approach could account for more complex factors, such as hydration shells and correlation effects, thereby enriching the understanding of the underlying dynamics.

Bibliography

[1] A. Levy, J. P. de Souza, and M. Z. Bazant, "Breakdown of electroneutrality in nanopores," *Journal of Colloid and Interface Science*, vol. 579, pp. 162–176, 2020.

[2] J. C. Eijkel and A. v. d. Berg, "Nanofluidics: What is it and what can we expect from it?" *Microfluidics and Nanofluidics*, vol. 1, pp. 249–267, 2005.

[3] B. Hille, "Ionic channels in excitable membranes. current problems and biophysical approaches," *Biophysical journal*, vol. 22, no. 2, pp. 283–294, 1978.

[4] D. A. Doyle *et al.*, "The structure of the potassium channel: Molecular basis of k+ conduction and selectivity," *science*, vol. 280, no. 5360, pp. 69–77, 1998.

[5] J. Yang, F. Lu, L. W. Kostiuk, and D. Y. Kwok, "Electrokinetic microchannel battery by means of electrokinetic and microfluidic phenomena," *Journal of Micromechanics and Microengineering*, vol. 13, no. 6, p. 963, 2003.

[6] S. J. Kim, S. H. Ko, K. H. Kang, and J. Han, "Direct seawater desalination by ion concentration polarization," *Nature nanotechnology*, vol. 5, no. 4, pp. 297–301, 2010.

[7] A. Mani and M. Z. Bazant, "Deionization shocks in microstructures," *Physical Review E*, vol. 84, no. 6, p. 061 504, 2011.

[8] D. Cohen-Tanugi and J. C. Grossman, "Water desalination across nanoporous graphene," *Nano letters*, vol. 12, no. 7, pp. 3602–3608, 2012.

[9] S. H. Roelofs, A. van den Berg, and M. Odijk, "Microfluidic desalination techniques and their potential applications," *Lab on a Chip*, vol. 15, no. 17, pp. 3428–3438, 2015.

[10] A. De La Escosura-Muñiz and A. Merkoçi, "Nanochannels preparation and application in biosensing," *ACS nano*, vol. 6, no. 9, pp. 7556–7583, 2012.

[11] W. Reisner, J. N. Pedersen, and R. H. Austin, "Dna confinement in nanochannels: Physics and biological applications," *Reports on progress in physics*, vol. 75, no. 10, p. 106 601, 2012.

[12] S. Berneche and B. Roux, "Energetics of ion conduction through the k+ channel," *Nature*, vol. 414, no. 6859, pp. 73–77, 2001.

[13] P. Hess and R. W. Tsien, "Mechanism of ion permeation through calcium channels," *Nature*, vol. 309, no. 5967, pp. 453–456, 1984.

[14] C. Werner, R. Zimmermann, and T. Kratzmüller, "Streaming potential and streaming current measurements at planar solid/liquid interfaces for simultaneous determination of zeta potential and surface conductivity," *Colloids and Surfaces A: Physicochemical and Engineering Aspects*, vol. 192, no. 1-3, pp. 205–213, 2001.

[15] J. J. Vilatela and R. Marcilla, "Tough electrodes: Carbon nanotube fibers as the ultimate current collectors/active material for energy management devices," *Chemistry of Materials*, vol. 27, no. 20, pp. 6901–6917, 2015.

[16] C. Y. Lee, W. Choi, J.-H. Han, and M. S. Strano, "Coherence resonance in a single-walled carbon nanotube ion channel," *Science*, vol. 329, no. 5997, pp. 1320–1324, 2010.

[17] K. V. Agrawal, S. Shimizu, L. W. Drahushuk, D. Kilcoyne, and M. S. Strano, "Observation of extreme phase transition temperatures of water confined inside isolated carbon nanotubes," *Nature nanotechnology*, vol. 12, no. 3, pp. 267–273, 2017.

[18] A. Siria *et al.*, "Giant osmotic energy conversion measured in a single transmembrane boron nitride nanotube," *Nature*, vol. 494, no. 7438, pp. 455–458, 2013.

[19] W. Guan and M. A. Reed, "Electric field modulation of the membrane potential in solid-state ion channels," *Nano letters*, vol. 12, no. 12, pp. 6441–6447, 2012.

[20] H. Daiguji, P. Yang, A. J. Szeri, and A. Majumdar, "Electrochemomechanical energy conversion in nanofluidic channels," *Nano letters*, vol. 4, no. 12, pp. 2315–2321, 2004.

[21] S. Faucher *et al.*, "Critical knowledge gaps in mass transport through single-digit nanopores: A review and perspective," *The Journal of Physical Chemistry C*, vol. 123, no. 35, pp. 21 309–21 326, 2019.

[22] D. Duong-Hong, J.-S. Wang, G. Liu, Y. Z. Chen, J. Han, and N. G. Hadjiconstantinou, "Dissipative particle dynamics simulations of electroosmotic flow in nano-fluidic devices," *Microfluidics and Nanofluidics*, vol. 4, no. 3, pp. 219–225, 2008.

[23] J.-F. Gwan and A. Baumgaertner, "Ion transport in a nanochannel," *Journal of Computational and Theoretical Nanoscience*, vol. 4, no. 1, pp. 50–56, 2007.

[24] R. Qiao and N. R. Aluru, "Ion concentrations and velocity profiles in nanochannel electroosmotic flows," *The Journal of chemical physics*, vol. 118, no. 10, pp. 4692–4701, 2003.

[25] D. Xu, D. Li, Y. Leng, and Y. Chen, "Molecular dynamics simulation of ion distribution in nanochannels," in *ASME International Mechanical Engineering Congress and Exposition*, vol. 47756, 2006, pp. 641–645.

[26] A. Raghunathan and N. Aluru, "Self-consistent molecular dynamics formulation for electric-field-mediated electrolyte transport through nanochannels," *Physical Review E*, vol. 76, no. 1, p. 011 202, 2007.

[27] M. Wang and Z. Li, "Nonideal gas flow and heat transfer in micro-and nanochannels using the direct simulation monte carlo method," *Physical Review E*, vol. 68, no. 4, p. 046 704, 2003.

[28] A. J. Frijns, S. V. Nedea, A. A. van Steenhoven, A. J. Markvoort, and P. A. Hilbers, "Molecular dynamics and monte carlo simulations for heat transfer in micro-and nanochannels," *International journal for Multiscale Computational engineering*, vol. 4, no. 3, 2006.

[29] Y. Wang, D. R. Tree, and K. D. Dorfman, "Simulation of dna extension in nanochannels," *Macromolecules*, vol. 44, no. 16, pp. 6594–6604, 2011.

[30] C. Micheletti and E. Orlandini, "Knotting and metric scaling properties of dna confined in nano-channels: A monte carlo study," *Soft Matter*, vol. 8, no. 42, pp. 10 959–10 968, 2012.

[31] R. Chang and K. Jo, "Dna conformation in nanochannels: Monte carlo simulation studies using a primitive dna model," *The Journal of chemical physics*, vol. 136, no. 9, 2012.

[32] S. Nedea, A. Frijns, A. Van Steenhoven, A. J. Markvoort, and P. Hilbers, "Hybrid method coupling molecular dynamics and monte carlo simulations to study the properties of gases in microchannels and nanochannels," *Physical Review E*, vol. 72, no. 1, p. 016 705, 2005.

[33] S. Nedea, A. J. Markvoort, A. van Steenhoven, and P. Hilbers, "Heat transfer predictions for micro-/nanochannels at the atomistic level using combined molecular dynamics and monte carlo techniques," 2009.

[34] S. Nedea, A. van Steenhoven, A. Markvoort, P. Spijker, and D. Giordano, "Gas-surface interactions using accommodation coefficients for a dilute and a dense gas in a micro-or nanochannel: Heat flux predictions using combined molecular dynamics and monte carlo techniques," *Physical Review E*, vol. 89, no. 5, p. 053 012, 2014.

[35] G. Karniadakis, A. Beskok, and N. Aluru, *Microflows and nanoflows: fundamentals and simulation*. Springer Science & Business Media, 2006, vol. 29.

[36] X. Li, J. Fan, H. Yu, Y. Zhu, and H. Wu, "Lattice boltzmann method simulations about shale gas flow in contracting nano-channels," *International Journal of Heat and Mass Transfer*, vol. 122, pp. 1210–1221, 2018.

[37] Y. Jin, X. Liu, Z. Liu, S. Lu, and Q. Xue, "Effect of interfacial layer on water flow in nanochannels: Lattice boltzmann simulations," *Physica B: Condensed Matter*, vol. 487, pp. 18–24, 2016.

[38] J. Ghazanfarian and A. Abbassi, "Heat transfer and fluid flow in microchannels and nanochannels at high knudsen number using thermal lattice-boltzmann method," *Physical review E*, vol. 82, no. 2, p. 026 307, 2010.

[39] F. Tian, B. Li, and D. Y. Kwok, "Lattice boltzmann simulation of electroosmotic flows in micro-and nanochannels," in *2004 International Conference on MEMS, NANO and Smart Systems (ICMENS'04)*, IEEE, 2004, pp. 294–299.

[40] A. Karimipour, "Provide a suitable range to include the thermal creeping effect on slip velocity and temperature jump of an air flow in a nanochannel by lattice boltzmann method," *Physica E: Low-dimensional Systems and Nanostructures*, vol. 85, pp. 143–151, 2017.

[41] Y. Shi, T. Zhao, and Z. Guo, "Lattice boltzmann simulation of thermal electroosmotic flows in micro/nanochannels," *Journal of Computational and Theoretical Nanoscience*, vol. 5, no. 2, pp. 236–246, 2008.

[42] P. Hoogerbrugge and J. Koelman, "Simulating microscopic hydrodynamic phenomena with dissipative particle dynamics," *Europhysics letters*, vol. 19, no. 3, p. 155, 1992.

[43] P. Espanol and P. Warren, "Statistical mechanics of dissipative particle dynamics," *Europhysics letters*, vol. 30, no. 4, p. 191, 1995.

[44] P. Nikunen, M. Karttunen, and I. Vattulainen, "How would you integrate the equations of motion in dissipative particle dynamics simulations?" *Computer physics communications*, vol. 153, no. 3, pp. 407–423, 2003.

[45] D. A. Fedosov, G. Em Karniadakis, and B. Caswell, "Dissipative particle dynamics simulation of depletion layer and polymer migration in micro-and nanochannels for dilute polymer solutions," *The Journal of chemical physics*, vol. 128, no. 14, 2008.

[46] D. Kasiteropoulou, T. E. Karakasidis, and A. Liakopoulos, "Dissipative particle dynamics investigation of parameters affecting planar nanochannel flows," *Materials Science and Engineering: B*, vol. 176, no. 19, pp. 1574–1579, 2011.

[47] J. Smiatek and F. Schmid, "Polyelectrolyte electrophoresis in nanochannels: A dissipative particle dynamics simulation," *The Journal of Physical Chemistry B*, vol. 114, no. 19, pp. 6266–6272, 2010.

[48] Y. Zheng, A. L. Garcia, and B. J. Alder, "Comparison of kinetic theory and hydrodynamics for poiseuille flow," *Journal of Statistical Physics*, vol. 109, pp. 495–505, 2002.

[49] D. Y. Chan and R. Horn, "The drainage of thin liquid films between solid surfaces," *The Journal of chemical physics*, vol. 83, no. 10, pp. 5311–5324, 1985.

[50] J. Georges, S. Millot, J. Loubet, and A. Tonck, "Drainage of thin liquid films between relatively smooth surfaces," *The Journal of chemical physics*, vol. 98, no. 9, pp. 7345–7360, 1993.

[51] U. Raviv and J. Klein, "Fluidity of bound hydration layers," *Science*, vol. 297, no. 5586, pp. 1540–1543, 2002.

[52] J. Gao, R. Szoszkiewicz, U. Landman, E. Riedo, *et al.*, "Structured and viscous water in subnanometer gaps," *Physical Review B*, vol. 75, no. 11, p. 115 415, 2007.

[53] A. Maali, T. Cohen-Bouhacina, G. Couturier, and J.-P. Aimé, "Oscillatory dissipation of a simple confined liquid," *Physical review letters*, vol. 96, no. 8, p. 086 105, 2006.

[54] T. Becker and F. Mugele, "Nanofluidics: Viscous dissipation in layered liquid films," *Physical Review Letters*, vol. 91, no. 16, p. 166 104, 2003.

[55] L. Bocquet and E. Charlaix, "Nanofluidics, from bulk to interfaces," *Chemical Society Reviews*, vol. 39, no. 3, pp. 1073–1095, 2010.

[56] W. Lo, K. Chan, and K. Mok, "Molecular dynamics simulation of ions in charged capillaries," *Journal of Physics: Condensed Matter*, vol. 6, no. 23A, A145, 1994.

[57] W. Lo, K. Chan, M. Lee, and K. Mok, "Molecular simulation of electrolytes in nanopores," *Journal of Electroanalytical Chemistry*, vol. 450, no. 2, pp. 265–272, 1998.

[58] A. P. Thompson, "Nonequilibrium molecular dynamics simulation of electro-osmotic flow in a charged nanopore," *The Journal of chemical physics*, vol. 119, no. 14, pp. 7503–7511, 2003.

[59] J. B. Freund, "Electro-osmosis in a nanometer-scale channel studied by atomistic simulation," *The Journal of Chemical Physics*, vol. 116, no. 5, pp. 2194–2200, 2002.

[60] R. Qiao and N. R. Aluru, "Scaling of electrokinetic transport in nanometer channels," *Langmuir*, vol. 21, no. 19, pp. 8972–8977, 2005.

[61] S. Cui and H. Cochran, "Electroosmotic flow in nanoscale parallel-plate channels: Molecular simulation study and comparison with classical poisson–boltzmann theory," *Molecular Simulation*, vol. 30, no. 5, pp. 259–266, 2004.

[62] J.-F. Dufrêche, V. Marry, N. Malikova, and P. Turq, "Molecular hydrodynamics for electro-osmosis in clays: From kubo to smoluchowski," *Journal of molecular liquids*, vol. 118, no. 1-3, pp. 145–153, 2005.

[63] W. Zhu, S. J. Singer, Z. Zheng, and A. Conlisk, "Electro-osmotic flow of a model electrolyte," *Physical review E*, vol. 71, no. 4, p. 041 501, 2005.

[64] M. Wang and S. Chen, "On applicability of poisson-boltzmann equation for micro-and nanoscale electroosmotic flows," *Commun Comput Phys*, vol. 3, no. 5, pp. 1087–1099, 2008.

[65] I. Borukhov, D. Andelman, and H. Orland, "Adsorption of large ions from an electrolyte solution: A modified poisson–boltzmann equation," *Electrochimica Acta*, vol. 46, no. 2-3, pp. 221–229, 2000.

[66] L. Lue, N. Zoeller, and D. Blankschtein, "Incorporation of nonelectrostatic interactions in the poisson- boltzmann equation," *Langmuir*, vol. 15, no. 11, pp. 3726–3730, 1999.

[67] S. Woelki and H.-H. Kohler, "A modified poisson–boltzmann equation: Ii. models and solutions," *Chemical Physics*, vol. 261, no. 3, pp. 421–438, 2000.

[68] Z. Adamczyk and P. Warszyński, "Role of electrostatic interactions in particle adsorption," *Advances in Colloid and Interface Science*, vol. 63, pp. 41–149, 1996.

[69] P. Peters, R. Van Roij, M. Z. Bazant, and P. Biesheuvel, "Analysis of electrolyte transport through charged nanopores," *Physical review E*, vol. 93, no. 5, p. 053 108, 2016.

[70] F. H. Van der Heyden, D. J. Bonthuis, D. Stein, C. Meyer, and C. Dekker, "Electrokinetic energy conversion efficiency in nanofluidic channels," *Nano letters*, vol. 6, no. 10, pp. 2232–2237, 2006.

[71] I. Vlassiouk, S. Smirnov, and Z. Siwy, "Ionic selectivity of single nanochannels," *Nano letters*, vol. 8, no. 7, pp. 1978–1985, 2008.

[72] D. Stein, M. Kruithof, and C. Dekker, "Surface-charge-governed ion transport in nanofluidic channels," *Physical Review Letters*, vol. 93, no. 3, p. 035 901, 2004.

[73] S. X. Li, W. Guan, B. Weiner, and M. A. Reed, "Direct observation of charge inversion in divalent nanofluidic devices," *Nano letters*, vol. 15, no. 8, pp. 5046–5051, 2015.

[74] P. Biesheuvel and M. Bazant, "Analysis of ionic conductance of carbon nanotubes," *Physical Review E*, vol. 94, no. 5, p. 050 601, 2016.

[75] R. J. Gross and J. Osterle, "Membrane transport characteristics of ultrafine capillaries," *The Journal of chemical physics*, vol. 49, no. 1, pp. 228–234, 1968.

[76] J. Fair and J. Osterle, "Reverse electrodialysis in charged capillary membranes," *The Journal of Chemical Physics*, vol. 54, no. 8, pp. 3307–3316, 1971.

[77] V. Sasidhar and E. Ruckenstein, "Electrolyte osmosis through capillaries," *Journal of colloid and interface science*, vol. 82, no. 2, pp. 439–457, 1981.

[78] E. Secchi, A. Niguès, L. Jubin, A. Siria, and L. Bocquet, "Scaling behavior for ionic transport and its fluctuations in individual carbon nanotubes," *Physical review letters*, vol. 116, no. 15, p. 154 501, 2016.

[79] Y.-C. Yao, A. Taqieddin, M. A. Alibakhshi, M. Wanunu, N. R. Aluru, and A. Noy, "Strong electroosmotic coupling dominates ion conductance of 1.5 nm diameter carbon nanotube porins," *ACS nano*, vol. 13, no. 11, pp. 12 851–12 859, 2019.

[80] Y. Ren and D. Stein, "Slip-enhanced electrokinetic energy conversion in nanofluidic channels," *Nanotechnology*, vol. 19, no. 19, p. 195 707, 2008.

[81] J. Cervera, B. Schiedt, and P. Ramirez, "A poisson/nernst-planck model for ionic transport through synthetic conical nanopores," *Europhysics letters*, vol. 71, no. 1, p. 35, 2005.

[82] M. Lozada-Cassou, W. Olivares, and B. Sulbarán, "Violation of the electroneutrality condition in confined charged fluids," *Physical Review E*, vol. 53, no. 1, p. 522, 1996.

[83] M. Lozada-Cassou, W. Olivares, B. Sulbarán, and Y. Jiang, "Violation of the electroneutrality condition in confined unsymmetrical electrolytes," *Physica A: Statistical Mechanics and its Applications*, vol. 231, no. 1-3, pp. 197–206, 1996.

[84] T. Colla, M. Girotto, A. P. Dos Santos, and Y. Levin, "Charge neutrality breakdown in confined aqueous electrolytes: Theory and simulation," *The Journal of chemical physics*, vol. 145, no. 9, 2016.

[85] M. Schmuck and M. Z. Bazant, "Homogenization of the poisson–nernst–planck equations for ion transport in charged porous media," *SIAM Journal on Applied Mathematics*, vol. 75, no. 3, pp. 1369–1401, 2015.

[86] Z.-X. Luo, Y.-Z. Xing, Y.-C. Ling, A. Kleinhammes, and Y. Wu, "Electroneutrality breakdown and specific ion effects in nanoconfined aqueous electrolytes observed by nmr," *Nature communications*, vol. 6, no. 1, p. 6358, 2015.

[87] Y. Noh and N. R. Aluru, "Ion transport in electrically imperfect nanopores," *ACS nano*, vol. 14, no. 8, pp. 10 518–10 526, 2020.

[88] A. Ji, B. Wang, G. Xia, J. Luo, and Z. Deng, "Effective modulation of ion mobility through solid-state single-digit nanopores," *Nanomaterials*, vol. 12, no. 22, p. 3946, 2022.

[89] J. P. de Souza, A. Levy, and M. Z. Bazant, "Electroneutrality breakdown in nanopore arrays," *Physical Review E*, vol. 104, no. 4, p. 044 803, 2021.

[90] J. Perram, R. Hunter, and H. Wright, "Charge and potential at the oxide/solution interface," *Chemical Physics Letters*, vol. 23, no. 2, pp. 265–269, 1973.

[91] S. H. Behrens and D. G. Grier, "The charge of glass and silica surfaces," *The Journal of Chemical Physics*, vol. 115, no. 14, pp. 6716–6721, 2001.

[92] R. Hunter and H. Wright, "The dependence of electrokinetic potential on concentration of electrolyte," *Journal of Colloid and Interface Science*, vol. 37, no. 3, pp. 564–580, 1971.

[93] J. A. Davis, R. O. James, and J. O. Leckie, "Surface ionization and complexation at the oxide/water interface: I. computation of electrical double layer properties in simple electrolytes," *Journal of colloid and interface science*, vol. 63, no. 3, pp. 480–499, 1978.

[94] J. Sonnefeld, A. Göbel, and W. Vogelsberger, "Surface charge density on spherical silica particles in aqueous alkali chloride solutions: Part 1. experimental results," *Colloid and Polymer Science*, vol. 273, pp. 926–931, 1995.

[95] R. B. Schoch, J. Han, and P. Renaud, "Transport phenomena in nanofluidics," *Reviews of modern physics*, vol. 80, no. 3, p. 839, 2008.

[96] M. Gouy, "Sur la constitution de la charge électrique à la surface d'un électrolyte," *J. Phys. Theor. Appl.*, vol. 9, no. 1, pp. 457–468, 1910.

[97] O. Stern, "Zur theorie der elektrolytischen doppelschicht," *Zeitschrift für Elektrochemie und angewandte physikalische Chemie*, vol. 30, no. 21-22, pp. 508–516, 1924.

[98] T.-L. Horng, "Review and modification of entropy modeling for steric effects in the poisson-boltzmann equation," *Entropy*, vol. 22, no. 6, p. 632, 2020.

[99] P. D. Beale, *Statistical Mechanics*. Butterworth-Heinemann, 1996.

[100] F. Fogolari and J. M. Briggs, "On the variational approach to poisson–boltzmann free energies," *Chemical Physics Letters*, vol. 281, no. 1-3, pp. 135–139, 1997.

[101] W. Kleijn and L. Bruner, "Derivation of the poisson—boltzmann equation by minimization of the helmholtz free energy using a variational principle," *Journal of colloid and interface science*, vol. 96, no. 1, pp. 20–27, 1983.

[102] J. D. Jackson, *Classical electrodynamics*, 1999.

[103] Z. Yuan, A. L. Garcia, G. P. Lopez, and D. N. Petsev, "Electrokinetic transport and separations in fluidic nanochannels," *Electrophoresis*, vol. 28, no. 4, pp. 595–610, 2007.

[104] W.-L. Hsu, D. J. Harvie, M. R. Davidson, D. E. Dunstan, J. Hwang, and H. Daiguji, "Viscoelectric effects in nanochannel electrokinetics," *The Journal of Physical Chemistry C*, vol. 121, no. 37, pp. 20 517–20 523, 2017.

[105] M. S. Kilic, M. Z. Bazant, and A. Ajdari, "Steric effects in the dynamics of electrolytes at large applied voltages. i. double-layer charging," *Physical review E*, vol. 75, no. 2, p. 021 502, 2007.

[106] M. S. Kilic, M. Z. Bazant, and A. Ajdari, "Steric effects in the dynamics of electrolytes at large applied voltages. ii. modified poisson-nernst-planck equations," *Physical review E*, vol. 75, no. 2, p. 021 503, 2007.

[107] I. Borukhov, D. Andelman, and H. Orland, "Steric effects in electrolytes: A modified poisson-boltzmann equation," *Physical review letters*, vol. 79, no. 3, p. 435, 1997.

[108] W. Jia, B. Tang, and P. Wu, "Novel slightly reduced graphene oxide based proton exchange membrane with constructed long-range ionic nanochannels via self-assembling of nafion," *ACS applied materials & interfaces*, vol. 9, no. 27, pp. 22 620–22 627, 2017.

[109] H. Daiguji, "Ion transport in nanofluidic channels," *Chemical Society Reviews*, vol. 39, no. 3, pp. 901–911, 2010.

[110] W. Jia, B. Tang, and P. Wu, "Novel composite pem with long-range ionic nanochannels induced by carbon nanotube/graphene oxide nanoribbon composites," *ACS applied materials & interfaces*, vol. 8, no. 42, pp. 28 955–28 963, 2016.

[111] S. Homaeigohar and M. Elbahri, "Graphene membranes for water desalination," *NPG Asia Materials*, vol. 9, no. 8, e427–e427, 2017.

[112] J. R. Werber, C. O. Osuji, and M. Elimelech, "Materials for next-generation desalination and water purification membranes," *Nature Reviews Materials*, vol. 1, no. 5, pp. 1–15, 2016.

[113] D.-K. Kim, C. Duan, Y.-F. Chen, and A. Majumdar, "Power generation from concentration gradient by reverse electrodialysis in ion-selective nanochannels," *Microfluidics and Nanofluidics*, vol. 9, pp. 1215–1224, 2010.

[114] Y.-C. Yao, Z. Li, A. J. Gillen, S. Yosinski, M. A. Reed, and A. Noy, "Electrostatic gating of ion transport in carbon nanotube porins: A modeling study," *The Journal of Chemical Physics*, vol. 154, no. 20, p. 204 704, 2021.

[115] A. Esfandiar *et al.*, "Size effect in ion transport through angstrom-scale slits," *Science*, vol. 358, no. 6362, pp. 511–513, 2017.

[116] R. Sai, K. Ueno, K. Fujii, Y. Nakano, and H. Tsutsumi, "Steric effect on li+ coordination and transport properties in polyoxetane-based polymer electrolytes bearing nitrile groups," *RSC advances*, vol. 7, no. 60, pp. 37 975–37 982, 2017.

[117] M. Mahmud and B. Kim, "Atomic boundary position and steric effects on ion transport and separation through nanoporous graphene membrane," *Journal of Mechanical Science and Technology*, vol. 37, no. 2, pp. 875–886, 2023.

[118] D. Pandey and S. Bhattacharyya, "Impact of surface hydrophobicity and ion steric effects on the electroosmotic flow and ion selectivity of a conical nanopore," *Applied Mathematical Modelling*, vol. 94, pp. 721–736, 2021.

[119] A. Iglič, E. Gongadze, and K. Bohinc, "Excluded volume effect and orientational ordering near charged surface in solution of ions and langevin dipoles," *Bioelectrochemistry*, vol. 79, no. 2, pp. 223–227, 2010.

[120] P. Berg and B. Benjaminsen, "Effects of finite-size ions and relative permittivity in a nanopore model of a polymer electrolyte membrane," *Electrochimica Acta*, vol. 120, pp. 429–438, 2014.

[121] F. Barbir, "Pem fuel cells-theory and practice'elsevier academic press," *Burlil/ on*, 2005.

[122] H. Liu, C. Song, L. Zhang, J. Zhang, H. Wang, and D. P. Wilkinson, "A review of anode catalysis in the direct methanol fuel cell," *Journal of Power Sources*, vol. 155, no. 2, pp. 95–110, 2006.

[123] C. Li, L. Wen, X. Sui, Y. Cheng, L. Gao, and L. Jiang, "Large-scale, robust mushroom-shaped nanochannel array membrane for ultrahigh osmotic energy conversion," *Science Advances*, vol. 7, no. 21, eabg2183, 2021.

[124] A. Hibara *et al.*, "Nanochannels on a fused-silica microchip and liquid properties investigation by time-resolved fluorescence measurements," *Analytical Chemistry*, vol. 74, no. 24, pp. 6170–6176, 2002.

[125] A. L. Garcia *et al.*, "Electrokinetic molecular separation in nanoscale fluidic channels," *Lab on a Chip*, vol. 5, no. 11, pp. 1271–1276, 2005.

[126] R. Karnik, K. Castelino, and A. Majumdar, "Field-effect control of protein transport in a nanofluidic transistor circuit," *Applied Physics Letters*, vol. 88, no. 12, p. 123 114, 2006.

Appendix A: Limiting trends for electroneutrality breakdown

Limiting trends refer to the convergence of electroneutrality breakdown curves as a specific parameter increases or decreases while all other parameters are held constant. The study of limiting trends is crucial for a parametric study in order to understand the behavior of the system. The limiting trends for electroneutrality breakdown are observed for the parametric analysis of $|\bar{\sigma}_s|$, η, and $\bar{R}_{out}$. Figure A.1a shows $|Q_{in}/Q_{out}|$ as a function of $1/\bar{\lambda}_D$ and $|\bar{\sigma}_s|$ across four orders of magnitude. Merging of the curves for lower $|\bar{\sigma}_s| = 0.273, 0.0273, 0.00273$ constitute the limiting curves for this case. In other words, $|Q_{in}/Q_{out}|$ is independent of $|\bar{\sigma}_s|$ for $|\bar{\sigma}_s|$ smaller than 0.273, corresponding to $\sigma_s = -1.0 \times 10^{-3}\, C/m^2$. The effect of η is exhibited in Fig. A.1b. The curves corresponding to $\eta = 1.25, 1.875$, and 2.5 are in close alignment, though not fully converged. Similarly, Fig. A.1c illustrates the trend of electroneutrality breakdown for different $\bar{R}_{out}$. The limiting behavior of the system is depicted by the curves corresponding to $\bar{R}_{out} = 10, 15$, and 20 for this case.

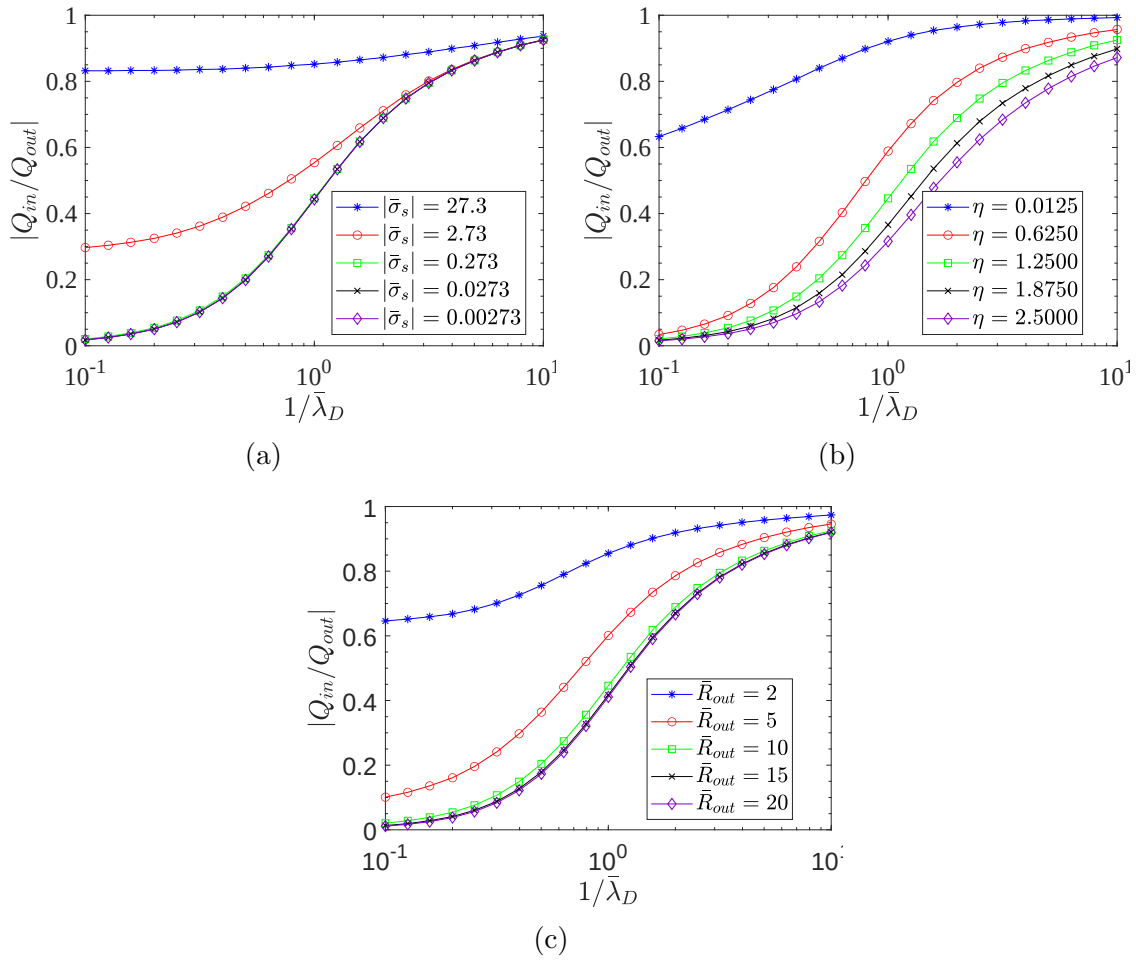

Figure A.1: Limiting trends emerge in the log-linear plots of $|Q_{in}/Q_{out}|$ as a function of $1/\bar{\lambda}_D$ for different (a) $\bar{\sigma}_s$, (b) η (c) $\bar{R}_{out}$.

Appendix B: Numerical modeling

The systems depicted in Figs. 3.3 and 5.1 are modeled using the electrostatics interface under the AC/DC module in COMSOL Multiphysics. Leveraging the symmetry of each system, only the upper half above the mid-cross section is modeled, as shown in Fig. B.1a for the single nanochannel and Fig. B.1b for the nanochannel array. Triangular and tetrahedral meshes with quadratic Lagrange elements are utilized for the discretization of the single nanochannel and the nanochannel array, respectively. The nanochannel (domain Ω_1) being the area of interest, has the smallest element size, followed by the dielectric medium (domain Ω_2) and the reservoirs (domain Ω_3). The time-independent nonlinear BVPs are solved using the Newton-Raphson method maintaining a residual of 1.0×10^{-4}. An average CPU time of 1 second is consumed for each simulation of the single channel whereas the nanochannel array consumes 2 minutes and 30 seconds.

To ascertain the reliability of the models, mesh convergence analyses are undertaken using reference parameters, listed in Table 3.1. The analyses, as depicted in Figs. B.2a and B.2b, illustrate the convergence of the ratio $|Q_{in}/Q_{out}|$ against the total number of elements in the system. Notably, $|Q_{in}/Q_{out}|$ converges for approximately 2.0×10^4 elements in the single nanochannel while it converges for approximately 2.0×10^5 elements in the nanochannel array

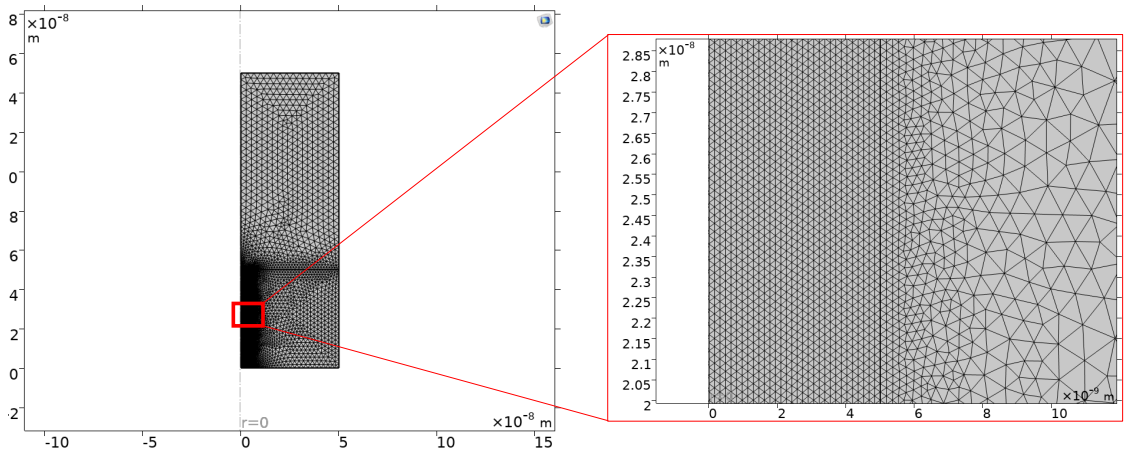

(a)

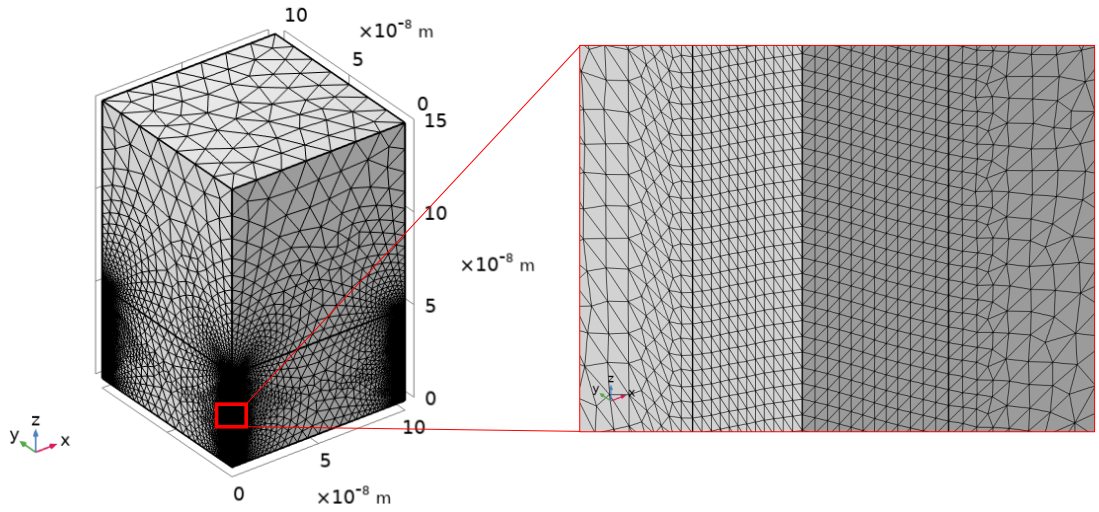

(b)

Figure B.1: Discretization of the (a) single nanochannel and (b) nanochannel array models employed in COMSOL Mutliphysics for the system depicted in Figs. B.1a and 5.1, respectively.

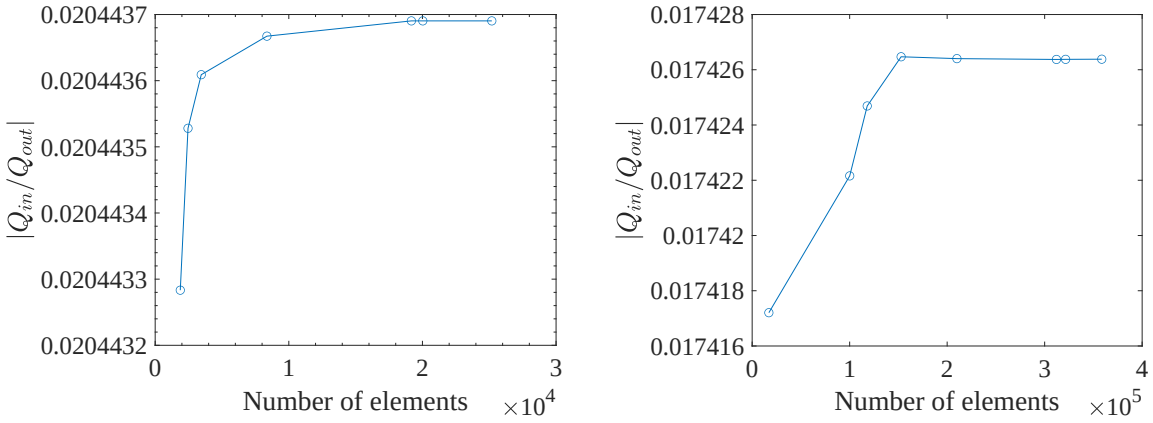

Figure B.2: Mesh convergence analysis for $|Q_{in}/Q_{out}|$ against the total number of elements in the (a) single nanochannel and (b) nanochannel array models.